nature portfolio

Peer Review File

High-density asymmetric iron dual-atom sites for efficient and stable electrochemical water oxidation

REVIEWER COMMENTS

Reviewer #1 (Remarks to the Author):

In this work, the authors reported the synthesis of a series of DACs as OER catalysts. The results showed that the asymmetric FeS1N2-FeN3 moieties exhibit the best OER performance and high stability. Due to my primary focus on theoretical computational research, I only pose the following questions from the perspective of theoretical computation.

1) In general, the substitution of N atom by S atom with a larger radius may lead to the structural distortion. For example, the introduced S dopant will be outward from the plane. However, in Supplementary Fig. 54, it seems that the two configurations exhibit different atom numbers. In particular, there are different configurations for DACs, please see applied Catalysis B: Environmental 2023, 339, 123156. why did the author adopt such the only configuration?

2) In the experimental parts, the authors only explored the OER catalytic performance. Why did the author also consider the ORR performance in the theoretical study?

3) For metal-based catalysts, the unpaired d-electrons are complex, which should be treated using DFT+U methods. At least, some test should be performed. In addition, rPBE method is suggested to confirm the accuracy of PBE.

4) The authors claimed that the surfaces of DASs were all covered by 1.5 O coverages. Did the experiments validate such a configuration?

5) Was this Gibbs free energy diagram obtained under applied voltage? If so, what method was used to calculate this issue? CHE or constant-potential method?

6) More discussion was suggested to be provided for the difference in OER catalytic performance before and after introducing S dopant.

Reviewer #2 (Remarks to the Author):

The manuscript "High-density asymmetric iron dual-atom sites for efficient and ultra-stable electrochemical water oxidation" reports a joint experimental-theoretical study on the performance of a dual-atom catalyst where two Fe atoms are stabilized in a Sulphur and Nitrogen doped carbon nanostructure leading to a particularly active system for the oxygen evolution reaction (OER). According to the results presented, the new catalyst outperforms the commercially used RuO_2 catalyst. The authors report the synthesis of the new catalyst where an impressive loading of 6.7% wt in Fe is achieved. The catalyst appears also to be particularly stable.

The results presented are interesting and sufficiently novel, and the characterization of the new material is accurate. However, since our expertise is theoretical, we will comment on this part of the work. In this respect, the theoretical part of the paper is not up to the level of the experimental sections. There are mainly three reasons for this.

The first aspect is methodological. The calculations are performed at the PBE level, thus neglecting the self-interaction problem inherent to DFT. For this, hybrid functionals (e.g. HSE06 or PBE0) or the DFT+U approach are recommended. Recent studies have shown that this can have considerable effects in

particular for systems with localized d electrons (Patel et al (2018). Theoretical approaches to describing the oxygen reduction reaction activity of single-atom catalysts. The Journal of Physical Chemistry C, 122(51), 29307-29318). One aspect where the theory part that needs to be improved is also in the description of the electronic structure of the system. Are the Fe atoms spin polarized? What is their magnetization? The problem of using a PBE approach could be smaller if the system is non-spin-polarized.
The second limitation is that in the study of the OER only a small number of classical intermediates has been considered, O*, OH*, and OOH*. These are the intermediates that form on metal electrodes, but recent studies have shown that other intermediates can form on single atom catalysts (Barlocco et al (2023). Does the Oxygen Evolution Reaction follow the classical OH*, O*, OOH* path on single atom catalysts?. Journal of Catalysis, 417, 351-359.). It is likely that this can occur also on dual atom catalysts. The possible formation of the unconventional intermediates should be checked, and at least the authors should mention that the neglection of the formation of these intermediates can affect the overall reaction profile.
A third, possibly less severe, limitation with respect to the previous ones, is the use of an implicit solvent model (polarized continuum model) to represent the solvent. Things can be substantially different with more refined models of the water solvent are adopted (Gono et al (2019). Effect of the solvent on the oxygen evolution reaction at the TiO2–water interface. The Journal of Physical Chemistry C, 123(30), 18467-18474). Even in this case, at least a warning should be given to the reader.
In conclusion, the approximations done in the theoretical part are rather severe, and they will certainly impact the final results. The authors should perform some additional calculations to check that the method adopted is sufficient to grasp the complexity of the catalyst studied. This can provide a more robust and credible support to the experimental results reported in the paper.

Reviewer #3 (Remarks to the Author):

I co-reviewed this manuscript with one of the reviewers who provided the listed reports. This is part of the Nature Communications initiative to facilitate training in peer review and to provide appropriate recognition for Early Career Researchers who co-review manuscripts.

Reviewer #4 (Remarks to the Author):

Please find attached.

Reviewer #5 (Remarks to the Author):

Atomic catalysts with diversified well-defined coordination configurations have attracted increasing attention due to their maximized atomic utilization and high catalytic activity. This manuscript submitted by Chen et al. constructed asymmetric nitrogen, sulfur-coordinated diatomic iron centers on highly defective nitrogen-doped carbon nanosheets, which possessed the atomic configuration of N2S1Fe-FeN3

moiety. Benefited from the spontaneous electric polarization occurred on the iron dual-atom sites of the A-Fe2S1N5/SNC catalyst, it displays ultra-high OER activity and stability in alkaline electrolyte. Moreover, alkaline AEMWE device catalyzed by A-Fe2S1N5/SNC displays good performance, indicating its broad practical application potential. This work provides a new guidance for simultaneously balancing activity and stability of double-atom catalysts toward electrocatalysis applications. Therefore, I recommend publishing this manuscript after minor revisions. Below is a list of specific comments and questions the authors should address before publication.

1. When fitting the average oxidation state of Fe in A-Fe2S1N5/SNC from the XANES spectra, the author mentioned that the first maximum of the first derivative is used as refer in Fig S14. So, why not choose the peak near 7120 ev for fitting?
2. Please check whether the lsv after ECSA normalization is suitable carefully and give the corresponding calculation details. It should be noted that ECSA = Cdl/Cs.
3. According to the catalyst's XPS data of S after the stability test, the signal of S almost disappeared. Is it accompanied by the metal leaching? Please provide the Fe content change before and after the test via ICP. In addition, how do the authors consider the balance between S corrosion during the OER process and its regulation of the original catalyst structure? Will this regulatory effect persist?
4. It is recommended that authors supply the catalytic performance under the industrial electrolytic water system, such as 80 °C, 30% KOH.
5. There are some vague description and typo errors in this article. Thus, for a better readability, please check throughout the whole article text and correct all the errors.

Title: High-density asymmetric iron dual-atom sites for efficient and ultra-stable electrochemical water oxidation

The present manuscript demonstrates the synthesis of asymmetric A-Fe2S1N5/SNC dual atom catalysts via two-step thermal annealing approaches. Initially, the authors fabricated SNC support using 2-benzimidazolethiol and melamine, while in the second Fe salt, melamine, and trimesic acid were used for implanting Fe sites in the S, N-doped graphenic structures. The developed materials were characterized using AC-HAADF, STEM, XPS, and XAS measurements. XANES and EXAFS data fitting probe the proposed structure. The presence of high-density Fe dual sites (6.72 wt%) and S coordination was attributed to the increased OER performance compared to symmetric Fe2-NC and Fe1-NC structures. In OER a reduced potential of 193 mV at 10 mA cm-2 was obtained while catalyst stability was maintained for 2000h. The mechanism was thoroughly studied using DFT and in-situ XAS measurement. The scope of synthesis was explored for other 3d transition metals and ORR and Zn-Air battery application was also investigated. The manuscript provides appreciable analysis and enhanced performance however few questions related to the origin of exact coordination should be addressed before consideration of manuscript for the publication.

1. The graphical abstract of the study is missing. A nice sketched graphical abstract portraying the main finding of the manuscript should be added.
2. The authors claimed that ~81% of sites were present as dual S-coordinated sites. The S content of materials should be determined using CHNS analysis and compared with the given number.
3. A significant portion of S2p spectra demonstrated the presence of Sox species. However, these are not considered in the DFT calculation. What was the origin of SOx sites if the catalyst was prepared in an N2 environment? Do these species influence the OER activity?
4. The introduction needs slight improvement. The authors stated, "…due to their symmetric electron distribution." How the symmetric distribution of M2 sites on M2-N-C catalysts reduces the performance in OER should be explained. The authors should give some examples of cooperative catalysis by dual atom sites.
5. The BET surface area of catalysts should be provided and compared with the ECSA.
6. Considering the C/N and metal content. Can the authors predict the distance of Fe sites in a graphenic network? Since it is a high concentration, I think the calculated distance might be just for the uniformly distributed Fe single-atom sites. How about the possibility of the presence of a mixture of Fe-N4-C and Fe-N3S-C sites?
7. Indeed, the explanation of how Fe sites are arranged in dual atom sites is missing. Since Fe atoms are free to move (no preorganized

metal-organic complex was used) they can form dual atom sites, and triple atom sites as well. What factor promotes a precise organization of Fe sites on SNC sites?

8. In Figure 1a bottom part after annealing S sites are within the graphene network and not available for coordination. While in the final structure, these sites are coordinated to metal centers. Any explanation?
9. Figure 2, please enlarge the small area of Figure d to show Fe sites. I can see numerous sites that are randomly distributed. Fe K-edge in EELS spectra should be presented as inset. Do the authors observe any peak splitting? Similarly, XANES should have an inset showing an enlarged view of the high-energy region.
10. The peak assigned to Fe-S scattering in EXAFS spectra of A-Fe2S1N5/SNC might be from the Fe-C scattering path. Such scattering has been observed in high-density Fe-N-C catalysts (*Nat. Catal.* **2022**, *5*, 311– 323)
11. Though the OER performance of A-Fe2S1N5/SNC was compared with Fe1-N4 and Fe2N6-N catalysts. This does not verify that Fe1-N3S-C sites will be less active toward OER. A fair comparison with such catalysts is required both experimentally and in DFT.
12. What is the role of trimesic acid in the synthesis? It seems a source of carbon. The equation for the calculation of TOF should be added in SI.
13. Bader charge analysis of Fe atom bonded to N and S clearly shows a difference. I understand it is challenging but can the authors provide a charge on each Fe site from XANES or EXAFS?
14. What about the stability of the catalyst in ORR? After recycling the S2p peak was significantly diminished. Please explain.
15. Please add how XANES data was fitted. In Figure S26.there are two pyridinic N. Please Correct it.
16. The evolved oxygen should be measured either from GC or water replacement approach and demonstrate actual Faradain efficiency.
17. How authors have chosen a certain metal content for the synthesis. Is it possible to add more metal during synthesis? After the synthesis, did the authors use any acid leaching to remove any nanoparticles?
18. There are many grammatical/sentence errors. Remove hyperbolic phrases such as ultrahigh, unprecedented, etc. Double atom catalysts should be written as dual atom catalysts. Rephrase “which suffered confined pyrolysis…” Please add enough details in the experimental part such as the operating voltage of TEM. How samples were prepared for XPS. Do the authors perform any carbon correction of XPS spectra? What was the voltage for AC-HAADF?

Responses to the Referees' Comments

We express our sincere gratitude to the reviewers for their valuable and constructive comments on our manuscript. We have addressed each comment in detail and have revised the manuscript thoroughly, considering all the feedback and suggestions. The reviewers' comments are laid out below in Italic font and specific concerns have been numbered. Our responses and corresponding revisions are given in normal font with blue color.

Response to Reviewer 1:

In this work, the authors reported the synthesis of a series of DACs as OER catalysts. The results showed that the asymmetric FeS_1N_2-FeN_3 moieties exhibit the best OER performance and high stability. Due to my primary focus on theoretical computational research, I only pose the following questions from the perspective of theoretical computation.

Response: We thank the reviewer for carefully reviewing the manuscript with detailed constructive comments. All the insightful comments have been thoroughly considered, and we have performed a series of additional theoretical calculations to address all the concerns raised by the reviewer. The corresponding revisions have been made (please see the below).

Comment 1: *In general, the substitution of N atom by S atom with a larger radius may lead to the structural distortion. For example, the introduced S dopant will be outward from the plane. However, in Supplementary Fig. 54, it seems that the two configurations*

exhibit different atom numbers. In particular, there are different configurations for DACs, please see Applied Catalysis B: Environmental 2023, 339, 123156. why did the author adopt such the only configuration?

Response: We thank the reviewer for the constructive suggestions. According to the reviewer's advice, we have systematically rendered the possible configurations of DACs in **Fig. R1**, referring to the previous report.[1] Based on the second comment and Reviewer 2's suggestion, the PBE functional with and without DFT+U correction for the 3d orbitals of Fe atoms was adopted to evaluate their stabilities using formation energy calculations. Given the strong spin-polarized characteristic of Fe element, their ferromagnetic (FM) and anti-ferromagnetic (AFM) states of diatomic Fe sites for DACs were also considered initially. However, some AFM states may be changed to ferrimagnetic states after relaxation. Four kinds of possible Fe_2NC DACs were displayed in **Fig. R1**, named as Fe_2/N_3-6_1, Fe_2/N_3-6_2, Fe_2/N_4-6, and Fe_2/N_4-8. Their relative energies between FM and AFM state and formation energies were summarized in **Fig. R2**. Based on the results using PBE functional with and without DFT+U correction, their ground states are AFM states, except for the Fe_2/N_3-6_2 model with FM ground state just based on the pure PBE functional. All of the models exhibit negative formation energy. Among them, the Fe_2/N_3-6_2 model possesses the lowest formation energy, with values of -7.85 and -11.79 eV using PBE with and without DFT+U correction, respectively. The bond lengths of Fe-Fe and Fe-N are about 2.79 and 2.02 Å with the DFT+U method, respectively, which is close to the EXAFS fitting results. Therefore, the Fe_2/N_3-6_2 configuration serves as a symmetric Fe_2N_6/NC model used to

investigate the cascade OER or ORR process and is also regarded as the comparison of the asymmetric *A*-$Fe_2S_1N_5$/SNC model.

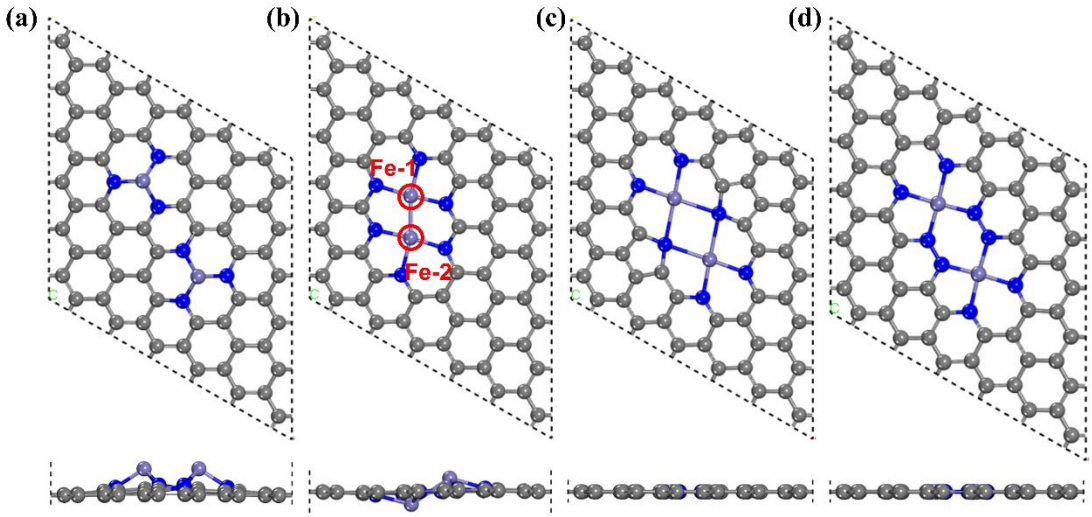

Fig. R1. Four kinds of optimized diatomic Fe embedding into N-doped graphene using PBE functional with DFT+U correction (effective U = 4 eV). (a) Fe_2/N_3-6_1, (b) Fe_2/N_3-6_2, (c) Fe_2/N_4-6, and (d) Fe_2/N_4-8. The brown, blue, and gray ball marks Fe, N, and C atoms, respectively. The red circles indicate Fe-1 and Fe-2 sites.

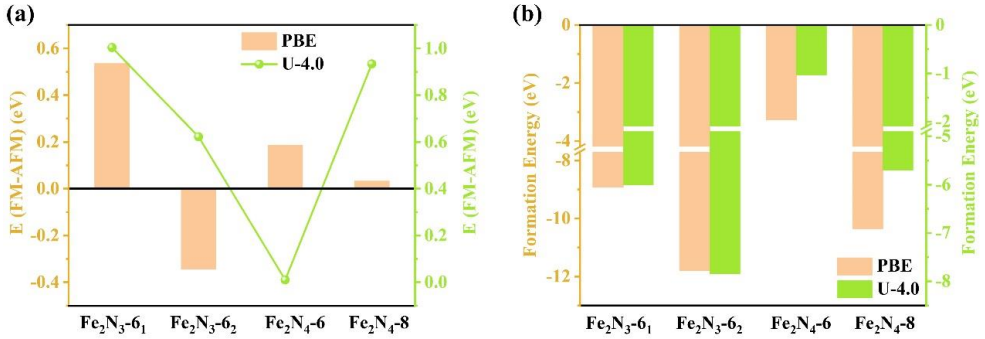

Fig. R2. (a) The energy difference between FM (ferromagnetic) and AFM (antiferromagnetic) states in possible diatomic Fe embedding into N-doped graphene configurations using PBE functional with and without DFT+U (U = 4.0 for Fe atom) correction. Note that FM and AFM states are based on the initial magnetic state setting, after optimizing, the AFM state may be altered to be a ferrimagnetic state. (b) Their

formation energies are based on the stable magnetic state.

Fig. R3 shows the possible asymmetric configurations of the *A*-$Fe_2S_1N_5$/SNC electrocatalyst, named "1-8". Based on the Fe_2/N_3-6_2 configuration, the "1-3" models just replace one nitrogen site using one sulfur atom with different nitrogen sites. One sulfur atom substitutes one carbon and one nitrogen site with different carbon-nitrogen sites to generate "4-6" models. The "7-8" models were similar to "4-6" configurations just with fewer nitrogen atoms. Their relative energies and formation energies were marked in **Fig. R4**. Interestingly, their ground states are all AFM states using PBE functional with DFT+U correction, but pure PBE functional obtain FM ground states except for the "8" model with AFM ground state by negligible energy disparity of 0.02 eV. They all have negative formation energy, among them the "1" model owned the lowest formation energy with -6.01 and -10.17 eV using PBE functional with and without DFT+U correction, respectively. The bond lengths of the Fe-Fe, Fe-S, and Fe-N pair are 2.40, 2.37, and 1.96 Å with the DFT+U method, respectively, which match well with the EXAFS fitting results. Therefore, the "1" model served as a stable *A*-$Fe_2S_1N_5$/NSC structure to research the following OER or ORR process.

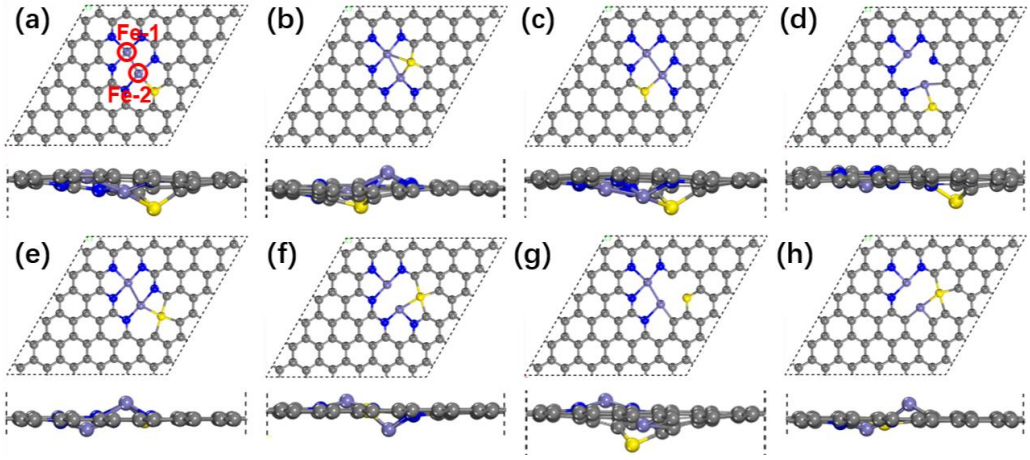

Fig. R3. The optimized configurations of *A*-Fe_2NS/NSC in the 6×6 supercell of

graphene using PBE functional with DFT+U correction (effective U = 4 eV). Based on the Fe_2N_6/NC model, (a-c) one nitrogen site was replaced by one sulfur atom with different nitrogen sites, named "1, 2, 3", (d-f) One sulfur atom substitutes one carbon and one nitrogen site with different carbon-nitrogen sites, named "4, 5, 6". (g, h) similar to "4-6" model, Fe atoms coordinating with fewer nitrogen atoms, named "7, 8". The brown, blue, yellow, and gray balls indicate Fe, N, S, and C atoms, respectively. The red circles indicate Fe-1 (with three nitrogen atoms) and Fe-2 (with two nitrogen atoms and one sulfur atom).

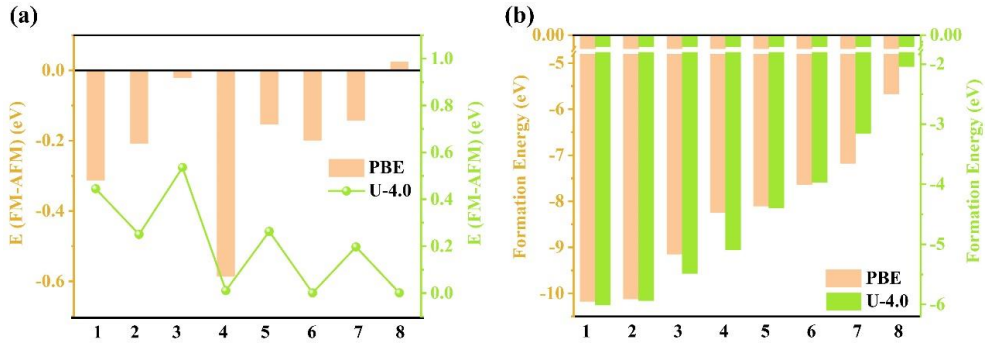

Fig. R4. (a) The energy difference between FM (ferromagnetic) and AFM (antiferromagnetic) states in possible *A*-Fe_2NS/NSC configurations (named "1-8") using PBE functional with and without DFT+U (U = 4.0 for Fe atom) correction. Note that FM and AFM states are based on the initial magnetic state setting, after optimizing, the AFM state may be altered to be a ferrimagnetic state. (b) Their formation energies are based on the stable magnetic state.

Reference:

[1] Zhao, T. et al. Homonuclear dual-atom catalysts embedded on N-doped graphene for highly effcient nitrate reduction to ammonia: From theoretical prediction to experimental validation. *Appl. Catal. B: Environ.* **339**, 123156 (2023).

Our revision: We have revised our manuscript according to the reviewer's suggestion (**Line 472-501** in the revised manuscript and **Supplementary Figs. 62-65**).

Comment 2: *In the experimental parts, the authors only explored the OER catalytic performance. Why did the author also consider the ORR performance in the theoretical study?*

Response: We sincerely appreciate the valuable suggestions. We only included target sample preparation and important experimental sections in the manuscript. Since the focus of this article is on the OER, only the catalytic performance of the OER was included in the manuscript. In addition, the prepared *A*-$Fe_2S_1N_5$/SNC catalyst also exhibits satisfactory ORR performance. The electrochemical test method and catalytic performance for ORR are presented in the **Methods** section of the **Supporting Information**. As shown in **Fig. R5**, *A*-$Fe_2S_1N_5$/SNC displayed superior ORR activity as evidenced by a high onset potential (E_{onset}) of 1.05 V, close to that of Pt/C (0.99 V). However, $Fe_1S_1N_3$/NC, Fe_2N_6/NC, Fe_1N_4/NC, and SNC exhibited lower electrocatalytic performance with E_{onset} values of 0.98, 0.97, 0.95, and 0.83 V, respectively. Linear sweep voltammetry (LSV) curves of these catalysts indicated the best activity of *A*-$Fe_2S_1N_5$/SNC with aspect to its highest halfwave potential ($E_{1/2}$). Specifically, $E_{1/2}$ of *A*-$Fe_2S_1N_5$/SNC, $Fe_1S_1N_3$/NC, Fe_2N_6/NC, Fe_1N_4/NC, SNC, and Pt/C was 0.91, 0.85, 0.82, 0.79, 0.70, and 0.85 V *vs.* RHE, respectively. The lowest Tafel slope of *A*-$Fe_2S_1N_5$/SNC (87 mV dec^{-1}) among those of $Fe_1S_1N_3$/NC (89 mV dec^{-1}), Fe_2N_6/NC (91 mV dec^{-1}), Fe_1N_4/NC (109 mV dec^{-1}), SNC (110 mV dec^{-1}), and Pt/C

(101 mV dec^{-1}) also supported the superior ORR kinetics of *A*-$Fe_2S_1N_5$/SNC (**Fig. R5b**). Moreover, *A*-$Fe_2S_1N_5$/SNC exhibited a remarkable kinetic current density (J_k) of 12.6 mA cm^{-2} at 0.85 V *vs.* RHE, about 4 times and 7 times higher than those of Fe_2N_6/NC (3.5 mA cm^{-2}) and Fe_1N_4/NC (1.8 mA cm^{-2}), respectively (**Fig. R5c**). Therefore, to gain a deeper understanding of the mechanism of *A*-$Fe_2S_1N_5$/SNC, we also considered the ORR performance in the theoretical study.

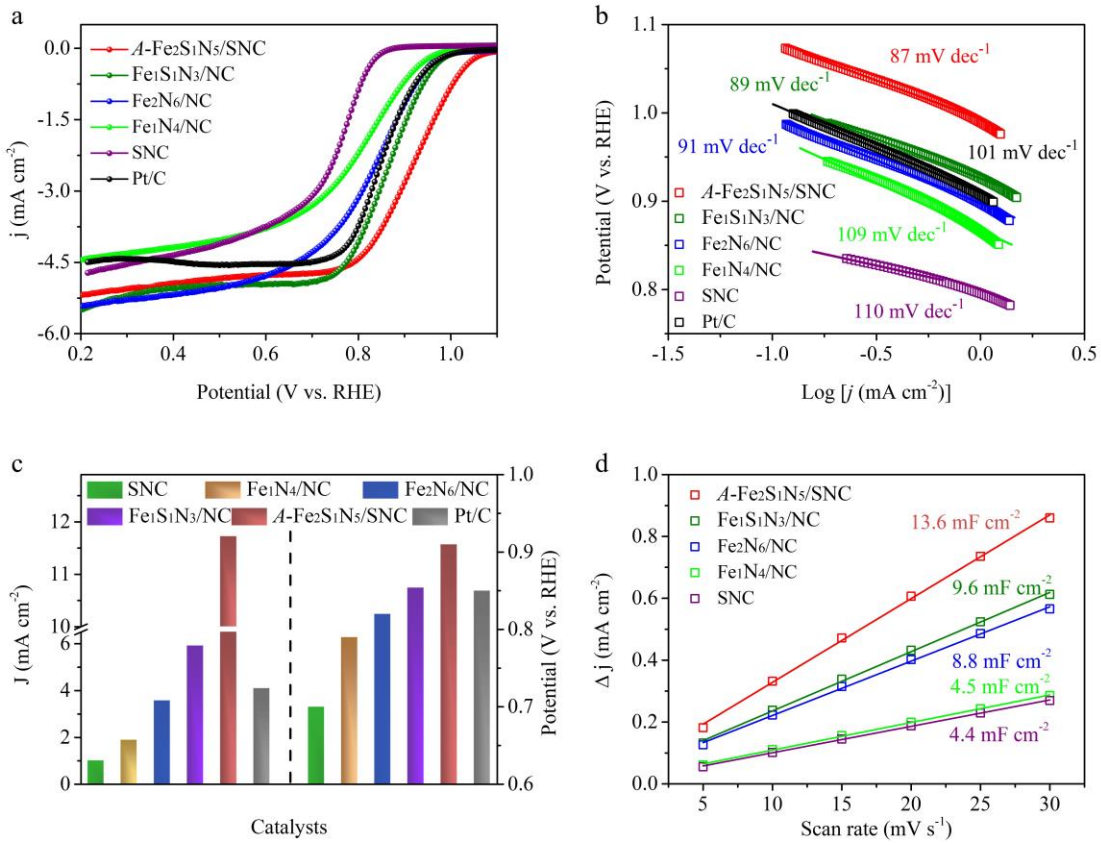

Fig. R5. ORR electrochemical activity in 0.1 M KOH. (a) LSV curves, (b) Tafel slopes, (c) kinetic current density (J_k) at 0.85 V versus reversible hydrogen electrode (versus RHE) and half-wave potentials, and (d) calculated C_{dl} values of *A*-$Fe_2S_1N_5$/SNC, $Fe_1S_1N_3$/NC, Fe_2N_6/NC, Fe_1N_4/NC, and SNC catalysts.

Our revision: We have revised our manuscript according to the reviewer's suggestion (**Supplementary Fig. 86**).

Comment 3: *For metal-based catalysts, the unpaired d-electrons are complex, which should be treated using DFT+U methods. At least, some test should be performed. In addition, rPBE method is suggested to confirm the accuracy of PBE.*

Response: We thank the reviewer for the constructive comments. Based on the reviewer's suggestions and reviewer 2's comments, the OER and ORR performances on the Fe_2N_6/NC and *A*-$Fe_2S_1N_5$/SNC systems were entirely evaluated by the DFT+U methods, referring to the previously similar report about diatomic Fe catalyst supporting on the nitrogen-doped graphene.[1] We have updated the results of the theoretical simulation in the revised manuscripts.

Based on the reviewer's comment, we systematically investigate the OER property of the *A*-$Fe_2S_1N_5$/SNC catalyst as an example to confirm their disparities using PBE and rPBE functional. Initially, the adsorption energies of oxygenated species (O, OH, H-OH, et al.) on the *A*-$Fe_2S_1N_5$/SNC catalyst were evaluated using PBE and rPBE functional, corresponding adsorption energies were shown in **Table R1**. The energy difference between PBE and rPBE methods was small, most of them are within the range of ±0.1 eV. Their free energy profiles are also very similar in **Fig. R6**. Under the electrochemical OER condition, such as 1.50 V vs RHE, the 3O species occupied the two Fe sites using the above methods, termed as 3O-$Fe_2S_1N_5$/SNC catalyst, indicating the uniformity of general functional using PBE and rPBE. Then the OER mechanism

using the above functionals was further evaluated on the 3O-$Fe_2S_1N_5$/SNC catalyst, the corresponding adsorption energy of intermediates including classical and unconventional complexes were shown in **Table R2**, and the adsorbed configurations resembled the results of DFT+U method. Their adsorption energy discrepancies are small, most of them are within the range of 0.2 eV. **Fig. R7** displayed the free energy changes of primary steps for OER in the potential of 1.23 V, they all featured the same reaction mechanism: H_2O (l)→*OH→*O→*O+*OH→2*O→O_2 (g). The elementary step 2*O→*+O_2 (g) was the maximal endothermic process. Above all, the electrochemical OER performance from rPBE can acquire coincident results, compared with PBE functional.

Table R1. The adsorption free energy of various species (H, OH, and O) on the *A*-$Fe_2S_1N_5$/SNC catalysts with the rPBE and PBE functional. MM represents the total magnetic moment. $\Delta G=\Delta G_{corr}+\Delta E$.

species	rPBE				PBE				ΔG_{PBE}-ΔG_{rPBE}
	MM (μB)	ΔE (eV)	ΔG_{corr} (eV)	ΔG (eV)	MM (μB)	ΔE (eV)	ΔG_{corr} (eV)	ΔG (eV)	(eV)
O	5.00	-0.14	0.01	-0.13	5.00	-0.17	0.01	-0.16	-0.03
OH	5.98	-0.73	0.31	-0.42	5.85	-0.71	0.31	-0.40	0.02
2OH	5.22	-0.69	0.63	-0.06	7.66	-0.65	0.63	-0.02	0.04
3OH	6.67	-0.76	0.94	0.18	6.67	-0.53	0.94	0.41	0.23
2O	7.00	1.06	0.02	1.08	7.00	1.20	0.02	1.22	0.14
3O	7.00	2.46	0.03	2.49	7.00	2.80	0.03	2.83	0.34

H-OH	5.00	0.59	0.66	1.25	5.00	0.46	0.66	1.11	-0.14

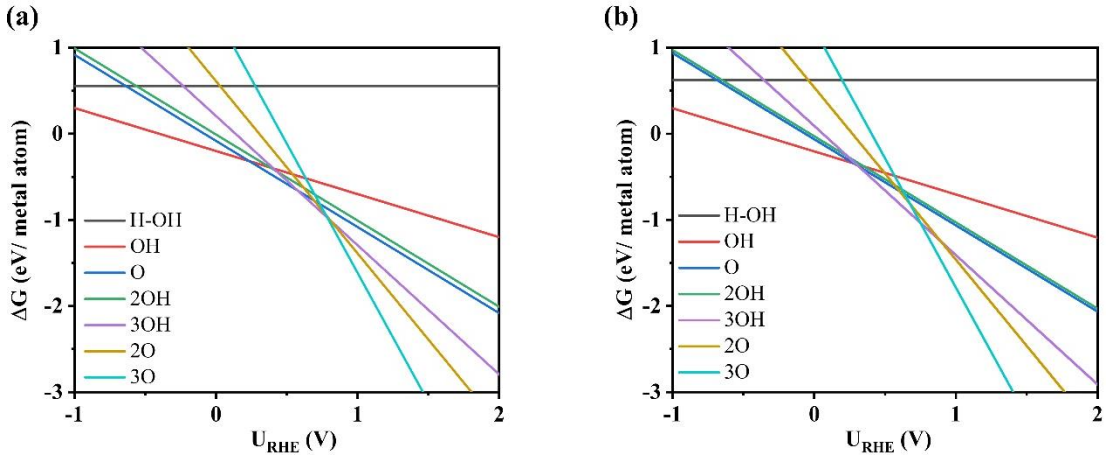

Fig. R6. Free energy profile of diverse O, OH, and H species coverage under reversed hydrogen electrode (RHE) on the *A*-$Fe_2S_1N_5$/SNC catalysts with the (a) PBE and (b) rPBE functional.

Table R2. The adsorption free energy of various OER intermediates on the 3O-*A*-$Fe_2S_1N_5$/SNC catalysts with the rPBE and PBE functional. MM represents the total magnetic moment. $\Delta G=\Delta G_{corr}+\Delta E$.

	rPBE				PBE				ΔG_{PBE}-
species	MM (μB)	ΔE (eV)	ΔG_{corr} (eV)	ΔG (eV)	MM (μB)	ΔE (eV)	ΔG_{corr} (eV)	ΔG (eV)	ΔG_{rPBE} (eV)
OH	6.00	0.44	0.31	0.75	6.00	0.58	0.31	0.89	0.14
O	7.00	1.25	0.01	1.26	7.00	1.50	0.01	1.51	0.25
2OH	6.78	1.20	0.63	1.83	6.78	1.36	0.63	1.99	0.16
OOH	8.00	3.31	0.31	3.62	8.00	3.46	0.31	3.77	0.15

O-OH	7.31	2.22	0.32	2.55	7.08	2.57	0.32	2.90	0.35
2O	6.08	3.65	0.02	3.67	5.91	4.08	0.02	4.10	0.43
O_2	7.00	4.33	-0.05	4.28	7.00	4.57	-0.05	4.52	0.24

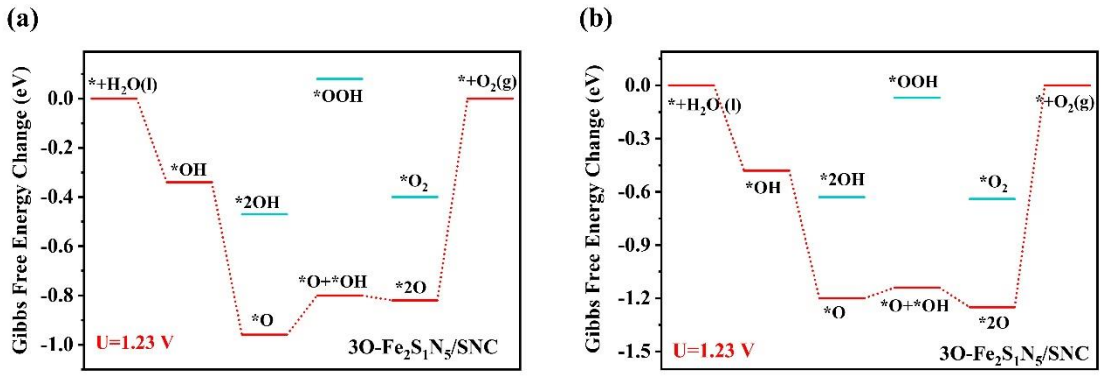

Fig. R7. Free energy profile of OER mechanism on the *A*-$Fe_2S_1N_5$/SNC catalysts with the (a) PBE and (b) rPBE functional.

Reference:

[1] Zhao, Y-X. et al. General synthesis of a diatomic catalyst library via a macrocyclic precursor-mediated approach. *J. Am. Chem. Soc*. **145**, 4819-4827 (2023).

Our revision: We have revised our manuscript according to the reviewer's suggestion (**Line 309-393** in the revised manuscript and **Supplementary Figs. 62-84**).

Comment 4: *The authors claimed that the surfaces of DASs were all covered by 1.5 O coverages. Did the experiments validate such a configuration?*

Response: We thank the referee for this comment and invaluable suggestion. To further elucidate the structural evolution during OER, the in-situ XAFS analysis was conducted. A homemade cell was applied to perform the in-situ XAFS tests, through the commonly used Lytle detector (in a fluorescence model) to collect all the spectra. The FT-EXAFS

spectra were recorded at Fe K-edges to further probe the evolution of the coordination configuration for Fe atoms in *A*-$Fe_2S_1N_5$/SNC. The Fe-N, Fe-S, and Fe-Fe shells displayed an obvious dynamic change during OER. The coordination peaks shift to the low-R region, which might be derived from the bridging adsorption of the oxygen-containing intermediates on dual Fe sites. By considering Fe-N, Fe-S, Fe-Fe, and Fe-O scattering paths, the first coordinated shell of EXAFS curve-fitting analysis for *A*-$Fe_2S_1N_5$/SNC was displayed in **Table R3**. Accordingly, the coordination number of Fe-O reached 1.4 at 1.42 V, which indicates that the surfaces of the Fe site were on average covered by 1.5 O coverages. The experimental results are consistent with the calculation.

Table R3. Structural parameters extracted from the Fe K-edge EXAFS fitting. (S_0^2=0.87)

sample	Scattering pair	CN	R(Å)	σ^2(10^{-3}Å^2)	ΔE_0(eV)	R factor
A-$Fe_2S_1N_5$/SNC-in situ-1.42V	Fe-N	2.3	1.85	6.5	2.0	0.009
	Fe-O	1.4	2.01	5.8		
	Fe-S	0.4	2.27	5.9		
	Fe-Fe	1.1	2.49	7.0		

Comment 5: *Was this Gibbs free energy diagram obtained under applied voltage? If so, what method was used to calculate this issue? CHE or constant-potential method?*

Response: We thank the reviewer for the constructive suggestions. In our electrochemical reaction simulation, we initially confirm the stable surface states of the catalyst using the Pourbaix phase under the electrochemical OER/ORR conditions and then calculate the Gibbs free energy diagram using the CHE model. This method was widely used in electrocatalytic simulations,[1-4] offers an effective solution to tackle the experimental phenomenon. We have included the computational method and discussion in the revised manuscript for your kind review.

References:

[1] Li, H. et al. Analysis of the limitations in the oxygen reduction activity of transition metal oxide surfaces. *Nat. Catal*. **4**, 463–468 (2021).

[2] Pan, S. et al. Efficient and stable noble-metal-free catalyst for acidic water oxidation. *Nat. Commun*. **13**, 2294 (2022).

[3] Yang, W. et al. Why is C–C coupling in CO_2 reduction still difficult on dual-atom electrocatalysts. *ACS Catal*. **13**, 9695−9705 (2023).

[4] Liu, H. et al. Origin of the superior oxygen reduction activity of zirconium nitride in alkaline media. *Chem. Sci.* **14**, 9000 (2023).

Our revision: We have revised our manuscript according to the reviewer's suggestion (**Line 319-334** and **Line 505-518** in the revised manuscript).

Comment 6: *More discussion was suggested to be provided for the difference in OER catalytic performance before and after introducing S dopant.*

Response: Thank you for your insightful comment. The mesoporous sulfur/nitrogen-

codoped carbon was employed as support to facilitate the formation of high-loading and atomically dispersed metal catalysts. The numerous defects and doped S/N endow the supports with a high density of anchor sites for the fixation of Fe atoms via the strong chemical metal-sulfur interactions. Furthermore, the microenvironment of typical M-N_4 active sites (where M represents Fe, Cu, Co, Ni, Mn, Pt, etc.) can be adjusted by S doping, which can effectively modify the electronic structure of SACs and optimize the adsorption strength of reaction intermediates.[1-4] Therefore, the sulfur-doped sample demonstrated enhanced alkaline OER performance compared to the non-doped sample.

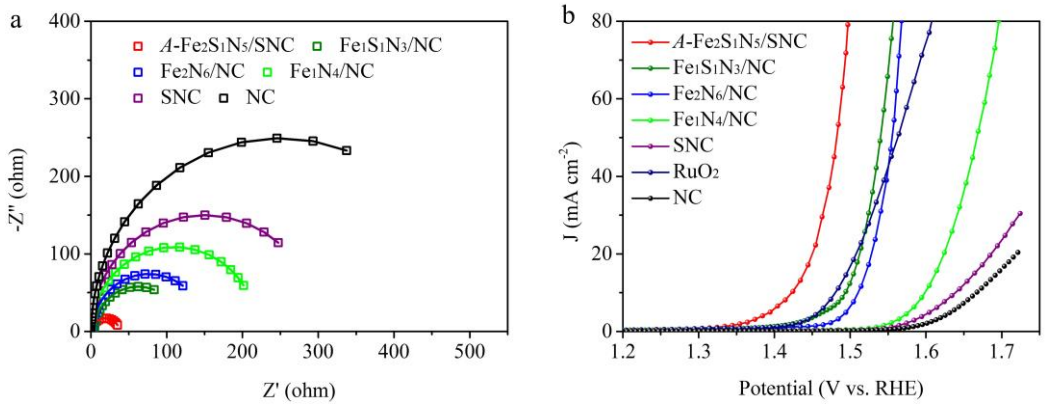

Fig. R8. OER electrochemical activity in 1.0 M KOH. (a) EIS curves and (b) LSV curves of *A*-$Fe_2S_1N_5$/SNC, $Fe_1S_1N_3$/NC, Fe_2N_6/NC, Fe_1N_4/NC, SNC, and NC catalysts.

As illustrated in **Fig. R8a**, the *A*-$Fe_2S_1N_5$/SNC catalyst exhibits a reduced charge transfer resistance compared to the Fe_2N_6/NC catalyst. This suggests an accelerated charge-transfer mechanism following sulfur after S doping during OER. Furthermore, the SNC support demonstrates a diminished charge transfer resistance relative to the NC support, indicating an enhanced electron transfer rate within the SNC framework. As a result, the incorporation of S dopant has been shown to increase the efficiency of

charge transfer during the alkaline OER. This improvement is linked to the formation of a highly polarized S-C bond, which arises from the contrasting electronegativities of sulfur and carbon. The presence of this bond facilitates electron transfer, leading to enhanced conductivity within the system. It's noted that the presence of positively charged carbon atoms is facilitated by the electron-withdrawing C-S-C species, which act as the active sites for OER.[5] This occurrence is attributed to the advantageous adsorption characteristics of positively charged carbon atoms towards hydroxyl species. Consequently, the SNC exhibits superior OER activity compared to the NC, which is consistent with the experimental results in **Fig. R8b**. To further understand the effect of S doping on OER performance, we prepared a comparative $Fe_1S_1N_3$/NC catalyst. The data presented in **Fig. R8a** illustrates that the $Fe_1S_1N_3$/NC catalyst exhibits enhanced conductivity compared to the sulfur-free Fe_1N_4/NC catalyst, as evidenced by its lower EIS value. Furthermore, the OER performance of the $Fe_1S_1N_3$/NC catalyst has also been improved, as depicted in the LSV curves for OER in **Fig. R8b**, demonstrating improved activity attributed to sulfur doping.

From a theoretical view, we also rendered comprehensive electronic structure simulations about the effect of introduced S sources on the OER performance. The results show that the excellent OER performance for 3O-$Fe_2S_1N_5$/SNC was mainly attributed to the enhanced oxygen capture ability induced by the involvement of unsymmetric S source and dual-atom Fe sites. From the Crystal Orbital Hamilton Population (COHP) results of the adsorbed O species between O and active Fe site on the diatomic catalyst in **Fig. R9**, 3O-$Fe_2S_1N_5$/SNC surface possessed stronger bond

strength with a more negative integrated COHP (ICOHP) value of –2.17 for spin up states and –3.44 for spin down states, principally dedicated by the Fe $3d_{yz}$ and O $2p_z$, Fe $3d_{xy}$ and O $2p_x$ than that of 3O-Fe_2N_6/NC with –2.13 and –3.35, respectively.

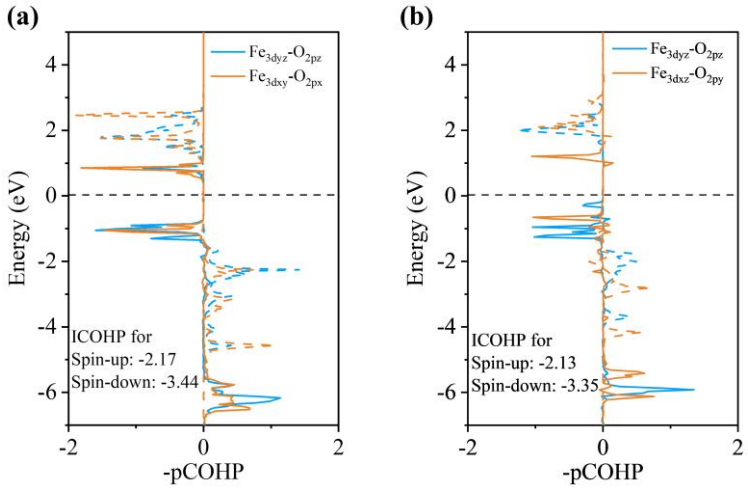

Fig. R9. The pCOHP results with O-Fe bond of OER intermediate on the 3O-$Fe_2S_1N_5$/SNC and 3O-Fe_2N_6/NC systems. Solid and dashed line marks the spin-up and spin-down, respectively.

The charge and spin magnetic moment distribution of active sites also played a critical role in the OER property,[52,53] simulated by Bader charge, differential and spin charge density in **Figs. R10** and **R11**. For the 3O-$Fe_2S_1N_5$/SNC, Fe-1 site reduced much more electrons (+1.52 e^-) to surrounding coordinate atoms than the Fe-2 site (+1.48 e^-) to generate localized spontaneous electric polarization, yet Fe-2 site possessed larger magnetic moment (MM: 3.82 μB) than Fe-1 site (3.60 μB), contrast with symmetrical 3O-Fe_2N_6/NC model for Fe-1 and Fe-2 site featuring same charge (+1.53 e^-) and magnetic moment (3.72 μB) distribution. Even though the obtained charge (+1.40 e^-) and MM (2.85 μB) of Fe site on the 2OH-$Fe_1S_1N_3$/NC catalyst was less than that of symmetrical 3O-Fe_2N_6/NC, the derived electric polarization induced by the

introduction of S source into FeN_4 moiety significantly boosted the OER performance. Above all, the endowed spontaneous electric polarization intensity by heteroatom S doping and dual-atom sites can synergistically optimize the adsorption capability of OER intermediates, thus promoting the electrochemical oxygen evolution property.

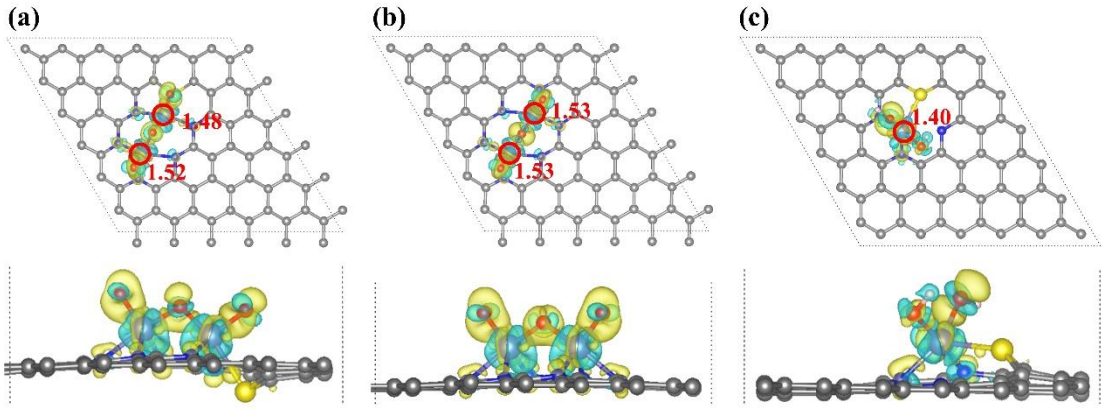

Fig. R10. Differential charge density diagram of (a) *A*-$Fe_2S_1N_5$/SNC, (b) Fe_2N_6/NC, and (c) $Fe_1S_1N_3$/NC between Fe and SNC/NC substrates. The yellow and cyan contour with the isosurface value of 0.01 e/bohr^3 marks augmented and reduced charge density, respectively. The number indicates the localized charge of the Fe atom by the scheme of the Bader formula. The brown, gray, blue, yellow, red, and white balls indicate Fe, C, N, S, O, and H atoms, respectively.

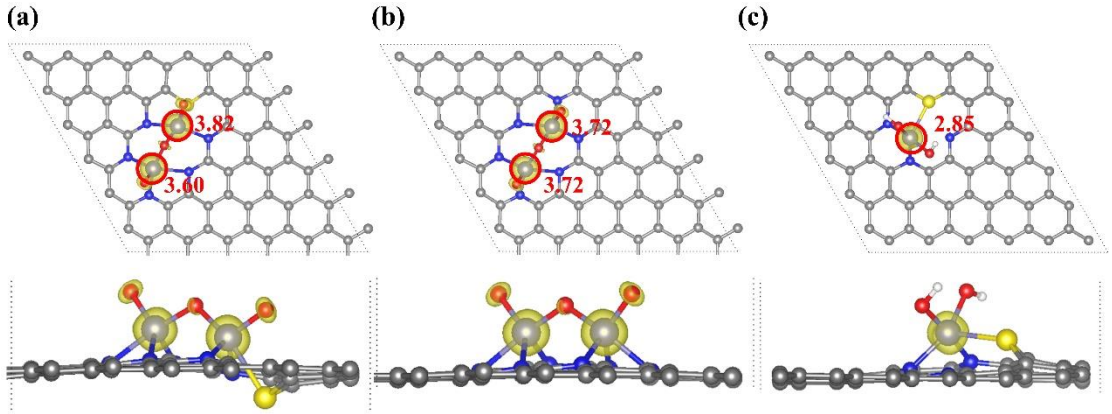

Fig. R11. Spin charge density diagram of (a) *A*-$Fe_2S_1N_5$/SNC, (b) Fe_2N_6/NC, and (c) $Fe_1S_1N_3$/NC between Fe and SNC/NC substrates. The yellow contour with the

isosurface value of 0.05 e/bohr^3 marks spin charge density, the number indicates the size of the magnetic moment. The brown, gray, blue, yellow, red, and white balls indicate Fe, C, N, S, O, and H atoms, respectively.

References:

[1] Yuan, S. et al. Decarboxylation-induced defects in MOF-derived single cobalt atom@carbon electrocatalysts for efficient oxygen reduction. *Angew. Chem. Int. Ed*. **60**, 21685-21690 (2021).

[2] Fan, M. et al. Improving the catalytic activity of carbon-supported single atom catalysts by polynary metal or heteroatom doping. *Small* **16**, 1906782 (2020).

[3] Zhang, Z. et al. Atomically dispersed cobalt trifunctional electrocatalysts with tailored coordination environment for flexible rechargeable Zn–air battery and self-driven water splitting. *Adv. Energy Mater*. **10**, 2002896 (2020).

[4] Zhang, J. et al. Tuning the coordination environment in single-atom catalysts to achieve highly efficient oxygen reduction reactions. *J. Am. Chem. Soc*. **141**, 20118-20126 (2019).

[5] Huang Y. et al. Atomic modulation and structure design of carbons for bifunctional electrocatalysis in metal-air batteries, *Adv. Mater.* 1803800 (2018).

Our revision: We have revised our manuscript according to the reviewer's suggestion (**Line 235-241**, **Line 361-380**, and **Fig 3a** in the revised manuscript, **Supplementary Fig. 37b** and **Supplementary Figs. 78-80**).

Response to Reviewer 2：

The manuscript "High-density asymmetric iron dual-atom sites for efficient and ultra-stable electrochemical water oxidation" reports a joint experimental-theoretical study on the performance of a dual-atom catalyst where two Fe atoms are stabilized in a Sulphur and Nitrogen doped carbon nanostructure leading to a particularly active system for the oxygen evolution reaction (OER). According to the results presented, the new catalyst outperforms the commercially used RuO_2 catalyst. The authors report the synthesis of the new catalyst where an impressive loading of 6.7% wt in Fe is achieved. The catalyst appears also to be particularly stable.

The results presented are interesting and sufficiently novel, and the characterization of the new material is accurate. However, since our expertise is theoretical, we will comment on this part of the work. In this respect, the theoretical part of the paper is not up to the level of the experimental sections. There are mainly three reasons for this.

Response: We thank the reviewer for the constructive suggestions about the improvement of our theoretical simulations when compared to previous work. And for their affirmation that this work should be published after addressing their concerns, which we believe we have done. We address them point-by-point:

Comment 1: *The first aspect is methodological. The calculations are performed at the PBE level, thus neglecting the self-interaction problem inherent to DFT. For this, hybrid functionals (e.g. HSE06 or PBE0) or the DFT+U approach are recommended. Recent studies have shown that this can have considerable effects in particular for*

systems with localized d electrons (Patel et al (2018). Theoretical approaches to describing the oxygen reduction reaction activity of single-atom catalysts. The Journal of Physical Chemistry C, 122(51), 29307-29318). One aspect where the theory part that needs to be improved is also in the description of the electronic structure of the system. Are the Fe atoms spin polarized? What is their magnetization? The problem of using a PBE approach could be smaller if the system is non-spin-polarized.

Response: We thank the reviewer for the constructive comments. We also agree with the reviewer's opinion about the effect of localized d electrons on the electrochemical OER and ORR performance and have systematically investigated the ORR and OER mechanism on the Fe_2N_6/NC and *A*-$Fe_2S_1N_5$/SNC surface using PBE functional with DFT+U correction (effective U = 4.0 eV for 3d orbitals of Fe element).[1]

(1) Considering the DFT+U correction, the bond length of Fe-Fe, Fe-N, and Fe-S pairs for the Fe_2N_6/NC and *A*-$Fe_2S_1N_5$/SNC models match well with the EXAFS fitting results in **Table R4**, compared with the pure PBE functional.

Table R4. The key bond lengths of Fe_2N_6/NC and *A*-$Fe_2S_1N_5$/SNC using the PBE and DFT+U method, compared to the EXAFS fitting results.

Sample	Bond	DFT+U/Å	PBE/Å	EXAFS fitting/Å
Fe_2N_6/NC	Fe-Fe	2.79	2.22	2.52
	Fe-N	2.02	2.02	1.92
A-$Fe_2S_1N_5$/SNC	Fe-Fe	2.40	2.17	2.56
	Fe-N	1.96	1.99	1.90
	Fe-S	2.37	2.33	2.30

(2) The electrochemical OER/ORR results were summarized in the theoretical simulation parts using the DFT+U method. We copied these contents below for your kind check in **Line 309-393** of the revised manuscript.

Line 309-393:

"**Theoretical study of *A*-$Fe_2S_1N_5$/SNC on OER.** To deeply unearth the activity origin of oxygen electrochemical reaction on the asymmetrical *A*-$Fe_2S_1N_5$/SNC catalyst in comparison with the Fe_2N_6/NC and $Fe_1S_1N_3$/NC catalyst, the first-principles method was adopted to study their proton-coupling electron-transfer (PCET) processes.[47] **Supplementary Figs. 62-65** show the possible configurations of Fe_2N_6/NC and *A*-$Fe_2S_1N_5$/SNC catalysts. Given the spin-polarized Fe element, their relative energies between ferromagnetic (FM) and anti-ferromagnetic (AFM) state for each model and formation energies were systematically evaluated to confirm their ground states of stable models. The Fe_2N_6/NC and *A*-$Fe_2S_1N_5$/SNC models were all AFM ground state, two Fe atoms were named Fe-1 and Fe-2 site for ease of distinction, which Fe-2 site connects with one S atom and two N atoms, and the Fe-1 site coordinates with only N atoms in unsymmetrical *A*-$Fe_2S_1N_5$/SNC model. The $Fe_1S_1N_3$/NC model was depicted in **Supplementary Fig. 66.** Initially, the adsorption of intermediates in OER/ORR was evaluated on the said models, corresponding adsorbed configurations and adsorption-free energies were shown in **Supplementary Figs. 67-69**, and **Supplementary Tables 9-11**, respectively. The O and OH species possess strong binding energy with –0.64 and –1.49 eV on the bare *A*-$Fe_2S_1N_5$/SNC surface, –0.44 and –1.25 eV on the bare Fe_2N_6/NC surface, 1.62 and 0.49 eV on the bare $Fe_1S_1N_3$/NC catalyst, respectively, all

deviating from the ideal adsorption energy of optimal OER/ORR catalyst with 2.46 and 1.23 eV. It meant that the O or OH intermediates were prone to occupy the Fe sites in the electrochemical surroundings.[48] As known, the Pourbaix diagram can clearly show the stable states of the catalyst surface under the electrochemical conditions, which are relative to the pH and electrode potential.[49] **Fig. 4a** and **Supplementary Fig. 70** depict the free energies of a series of coverage surfaces following electrode potential U vs. RHE sampled for *A*-$Fe_2S_1N_5$/SNC, Fe_2N_6/NC, and $Fe_1S_1N_3$/NC models. At the real electrochemical OER conditions, such as 1.50 V vs RHE, their surfaces were all covered by 3O with two Fe sites for diatomic catalysts and 2OH for $Fe_1S_1N_3$/NC catalyst, termed as 3O-$Fe_2S_1N_5$/SNC, 3O-Fe_2N_6/NC, and 2OH-$Fe_1S_1N_3$/NC in the OER surroundings, respectively. According to the OER mechanism of the single-atom catalysts reported by Pacchioni et al.,[50] at least one unconventional chemical intermediate, such as, 2*OH, *O + *OH, 2*O, and *O_2 ("*" marks surface site), was found to be more stable than the classical one including *O and *OOH species in all cases. Therefore, we systematically evaluated the adsorption of these OER intermediates composed of classical and unconventional ones on the above-mentioned surfaces, corresponding optimized adsorption configurations and adsorption energies were displayed in **Supplementary Figs. 71-73** and **Tables 12-14**. Their Gibbs free energy change of elementary steps for OER were depicted in **Figs. 4b-c** and **Supplementary Figs. 74-77**, the unconventional complex (*O + *OH) was more stable than classical *OOH intermediate on the Fe-2 site of 3O-$Fe_2S_1N_5$/SNC and 3O-Fe_2N_6/NC surface, and similar adsorption energy of *2OH and *O. Hence, their cascade

OER processes on the diatomic catalyst could get through unconventional intermediates: H_2O (l)→*OH→*2OH→*O+*OH→*O_2→O_2 (g). Considering the instability of the 2OH-$Fe_1S_1N_3$/NC catalyst induced by the unusual intermediates *2OH and *O + *OH, the classical steps were just considered for the OER process. The asymmetric diatomic catalyst 3O-$Fe_2S_1N_5$/SNC owned the lowest overpotential (0.32 V) under the involvement of an S source, compared to the symmetric 3O-Fe_2N_6/NC catalyst (0.41 V), and also excelled to single-atom catalyst 2OH-$Fe_1S_1N_3$/NC (0.35 V), consistent with the experimental measurements. Their potential-determined steps (PDSs) were the second dehydrogenation process [*OH → *2OH (O)]. **Fig. 4d** depicted the OER mechanism on the 3O-$Fe_2S_1N_5$/SNC catalyst in the light of unusual intermediates. Supposing based on the classical intermediates for OER [H_2O (l)→*OH→*O→*OOH→O_2 (g)], their overpotentials were 0.32, 0.44, and 0.35 V with the same PDSs of *OH→*O for 3O-$Fe_2S_1N_5$/SNC, 3O-Fe_2N_6/NC, and 2OH-$Fe_1S_1N_3$/NC, respectively. Regardless of classical and unconventional intermediates, *A*-$Fe_2S_1N_5$/SNC all possessed optimal electrochemical OER performance. Noting that the above OER results were based on implicit solvent model (VASPsol), which can generally capture the electrostatic interaction with diverse intermediates, neglect the influence of hydrogen bond on their stabilization and consequent OER mechanism using explicit solvent model.[51]

The excellent OER performance for 3O-$Fe_2S_1N_5$/SNC was mainly attributed to the enhanced oxygen capture ability induced by the involvement of unsymmetric S source and dual-atom Fe sites. From the Crystal Orbital Hamilton Population (COHP) results

of the adsorbed O species between O and active Fe site on the diatomic catalyst in **Supplementary Fig. S78,** 3O-$Fe_2S_1N_5$/SNC surface possessed stronger bond strength with a more negative integrated COHP (ICOHP) value of –2.17 for spin up states and –3.44 for spin down states, principally dedicated by the Fe $3d_{yz}$ and O $2p_z$, Fe $3d_{xy}$ and O $2p_x$ than that of 3O-Fe_2N_6/NC with –2.13 and –3.35, respectively. The charge and spin magnetic moment distribution of active sites also played a critical role in the OER property,[52,53] simulated by Bader charge, differential and spin charge density in **Supplementary Figs. 79-80.** For the 3O-$Fe_2S_1N_5$/SNC, Fe-1 site reduced much more electrons (+1.52 e^-) to surrounding coordinate atoms than the Fe-2 site (+1.48 e^-) to generate localized spontaneous electric polarization, yet Fe-2 site possessed larger magnetic moment (MM: 3.82 μB) than Fe-1 site (3.60 μB), contrast with symmetrical 3O-Fe_2N_6/NC model for Fe-1 and Fe-2 site featuring same charge (+1.53 e^-) and magnetic moment (3.72 μB) distribution. Even though the obtained charge (+1.40 e^-) and MM (2.85 μB) of Fe site on the 2OH-$Fe_1S_1N_3$/NC catalyst was less than that of symmetrical 3O-Fe_2N_6/NC, the derived electric polarization induced by the introduction of S source into FeN_4 moiety significantly boosted the OER performance. Above all, the endowed spontaneous electric polarization intensity by heteroatom S doping and dual-atom sites can synergistically optimize the adsorption capability of OER intermediates, thus promoting the electrochemical oxygen evolution property.

Similarly, at the electrochemical ORR realm, such as 0.90 V vs RHE, their surfaces were covered by 2OH species, named 2OH-$Fe_1S_1N_3$/NC, 2OH-Fe_2N_6/NC, and 2OH-$Fe_2S_1N_5$/SNC. **Supplementary Figs. 73, 81,** and **82** displayed the optimized ORR

intermediates, and corresponding adsorbed energies were shown in **Supplementary Tables 14-16. Supplementary Fig. 83** depicted the free energy changes of the ORR mechanism on the said surfaces, the asymmetric diatomic 2OH-$Fe_2S_1N_5$/SNC catalyst owned the largest onset potential (0.79 V) among that of 2OH-Fe_2N_6/NC (0.54 V) and 2OH-$Fe_1S_1N_3$/NC (0.65 V),[54] matching well with experimental results. Their PDSs were the first hydrogenation step for the generation of *OOH species. The enhanced capture of OOH species was distinctly ascribed to the large charge and spin magnetic moment population of active Fe site, specifically for asymmetric 2OH-$Fe_2S_1N_5$/SNC catalyst, evinced by **Supplementary Fig. 84.** Above all, the unsymmetrically geometric construction for *A*-$Fe_2S_1N_5$/SNC catalyst realized the spontaneous electric polarization by the coupling of dual site and heteroatom S doping to acquire a disparate OER/ORR performance."

(3) In the OER process, we systematically unearthed the activity origin of OER on the *A*-$Fe_2S_1N_5$/SNC surface using COHP bond analysis, charge and spin magnetic moment population analysis. We copied these discussions below for your kind check in **Line 361-377** of the revised manuscript.

Line 361-377:

"From the Crystal Orbital Hamilton Population (COHP) results of the adsorbed O species between O and active Fe site on the diatomic catalyst in **Supplementary Fig. S78,** 3O-$Fe_2S_1N_5$/SNC surface possessed stronger bond strength with a more negative integrated COHP (ICOHP) value of –2.17 for spin up states and –3.44 for spin down states, principally dedicated by the Fe $3d_{yz}$ and O $2p_z$, Fe $3d_{xy}$ and O $2p_x$ than that of

3O-Fe_2N_6/NC with –2.13 and –3.35, respectively. The charge and spin magnetic moment distribution of active sites also played a critical role in the OER property,[52,53] simulated by Bader charge, differential and spin charge density in **Supplementary Figs. 79-80.** For the 3O-$Fe_2S_1N_5$/SNC, Fe-1 site reduced much more electrons (+1.52 e^-) to surrounding coordinate atoms than the Fe-2 site (+1.48 e^-) to generate localized spontaneous electric polarization, yet Fe-2 site possessed larger magnetic moment (MM: 3.82 μB) than Fe-1 site (3.60 μB), contrast with symmetrical 3O-Fe_2N_6/NC model for Fe-1 and Fe-2 site featuring same charge (+1.53 e^-) and magnetic moment (3.72 μB) distribution. Even though the obtained charge (+1.40 e^-) and MM (2.85 μB) of Fe site on the 2OH-$Fe_1S_1N_3$/NC catalyst was less than that of symmetrical 3O-Fe_2N_6/NC, the derived electric polarization induced by the introduction of S source into FeN_4 moiety significantly boosted the OER performance. Above all, the endowed spontaneous electric polarization intensity by heteroatom S doping and dual-atom sites can synergistically optimize the adsorption capability of OER intermediates, thus promoting the electrochemical oxygen evolution property."

Reference:

[1] Zhao, Y-X. et al. General synthesis of a diatomic catalyst library via a macrocyclic precursor-mediated approach. *J. Am. Chem. Soc*. **145**, 4819-4827 (2023).

Our revision: We have revised our manuscript according to the reviewer's suggestion (**Line 309-393**, **Line 361-377,** and **Line 460-463** in the revised manuscript, **Supplementary Figs. 62-84**).

Comment 2: *The second limitation is that in the study of the OER only a small number of classical intermediates has been considered, O*, OH*, and OOH*. These are the intermediates that form on metal electrodes, but recent studies have shown that other intermediates can form on single atom catalysts (Barlocco et al (2023). Does the Oxygen Evolution Reaction follow the classical OH*, O*, OOH* path on single atom catalysts? Journal of Catalysis, 417, 351-359.). It is likely that this can occur also on dual atom catalysts. The possible formation of the unconventional intermediates should be checked, and at least the authors should mention that the neglection of the formation of these intermediates can affect the overall reaction profile.*

Response: We thank the reviewer for the constructive suggestions, and also agree with your opinion. We have updated the OER process considering the unconventional intermediates[1] in our revised manuscript in **Line 516-529** and **Line 334-353**.

Reference:

[1] Barlocco, I. et al. Does the oxygen evolution reaction follow the classical OH*, O*, OOH* path on single atom catalysts? *J. Catal.* **417**, 351–359 (2023).

In **Line 516-529：**

"The electrochemical oxygen evolution reaction (OER) and oxygen reduction reaction (ORR) mechanism were comprehensively researched via all the possible intermediates in the proton-coupling electron-transfer (PCET) processes referring to our previous work.[65,66]

For the electrochemical OER process, the possible elementary steps are below:

$H_2O+*\rightarrow *OH+H^+ +e^-$ (1)

$*OH \rightarrow *O + H^+ + e^-$ (2a)

$*OH + H_2O + * \rightarrow 2*OH + H^+ + e^-$ (2b)

$*O + H_2O + * \rightarrow *OOH + H^+ + e^-$ (3a)

$2*OH \rightarrow *O + *OH + H^+ + e^-$ (3b)

$*O + H_2O + * \rightarrow *O + *OH + H^+ + e^-$ (3c)

$*OOH \rightarrow *O_2 + H^+ + e^-$ (4a)

$*O + *OH \rightarrow 2*O + H^+ + e^-$ (4b)

$*O_2 \rightarrow * + O_2$ (g) (5a)

$2*O \rightarrow * + O_2$ (g) (5b)"

In **Line 334-353**:

"According to the OER mechanism of the single-atom catalysts reported by Pacchioni et al.,[50] at least one unconventional chemical intermediate, such as, 2*OH, *O + *OH, 2*O, and $*O_2$ ("*" marks surface site), was found to be more stable than the classical one including *O and *OOH species in all cases. Therefore, we systematically evaluated the adsorption of these OER intermediates composed of classical and unconventional ones on the above-mentioned surfaces, corresponding optimized adsorption configurations and adsorption energies were displayed in **Supplementary Figs. 71-73** and **Tables 12-14**. Their Gibbs free energy change of elementary steps for OER were depicted in **Figs. 4b-c** and **Supplementary Figs. 74-77**, the unconventional complex (*O + *OH) was more stable than classical *OOH intermediate on the Fe-2 site of $3O\text{-}Fe_2S_1N_5$/SNC and $3O\text{-}Fe_2N_6$/NC surface, and similar adsorption energy of *2OH and *O. Hence, their cascade OER processes on the diatomic catalyst could get

through unconventional intermediates: H_2O (l)→*OH→*2OH→*O+*OH→*O_2→O_2 (g). Considering the instability of the 2OH-$Fe_1S_1N_3$/NC catalyst induced by the unusual intermediates *2OH and *O + *OH, the classical steps were just considered for the OER process. The asymmetric diatomic catalyst 3O-$Fe_2S_1N_5$/SNC owned the lowest overpotential (0.32 V) under the involvement of an S source, compared to the symmetric 3O-Fe_2N_6/NC catalyst (0.41 V), and also excelled to single-atom catalyst 2OH-$Fe_1S_1N_3$/NC (0.35 V), consistent with the experimental measurements. Their potential-determined steps (PDSs) were the second dehydrogenation process [*OH → *2OH (O)]. **Fig. 4d** depicted the OER mechanism on the 3O-$Fe_2S_1N_5$/SNC catalyst in the light of unusual intermediates."

Our revision: We have revised our manuscript according to the reviewer's suggestion (**Line 516-529** and **Line 334-353** in the revised manuscript, **Supplementary Figs. 71-77, Supplementary Tables 12-14**).

Comment 3: *A third, possibly less severe, limitation with respect to the previous ones, is the use of an implicit solvent model (polarized continuum model) to represent the solvent. Things can be substantially different with more refined models of the water solvent are adopted (Gono et al (2019). Effect of the solvent on the oxygen evolution reaction at the TiO_2-water interface. The Journal of Physical Chemistry C, 123(30), 18467-18474). Even in this case, at least a warning should be given to the reader.*

Response: We thank the reviewer for the kind comments, and also agree with the effect of explicit solvent on the absolute value of reaction energies at specific electrochemical

systems (such as TiO_2-water[1]). The explicit solvent model can capture the hydrogen bond interacting with OER intermediates, evidently affecting the adsorption capability of oxygen intermediates. Given its huge computational cost, researchers often adopted implicit solvent models (such as VASPsol) as an alternative to simulate the electrochemical solvent surroundings, which can also capture the electrostatic interactions with oxygenous species, specifically for the comparisons of electrochemical performance on a series of similar systems.[2-4] In our works, we merely unravel the effect of asymmetric iron on the OER mechanism adopting the VASPsol model for three analogous systems (*A*-$Fe_2S_1N_5$/SNC, Fe_2N_6/NC, and $Fe_1S_1N_3$/NC), not focusing on the absolute value of reaction energy for the specific system. In the **Line 357-360** of the revised manuscript, we have discussed the effect of the explicit solvent model on the electrochemical OER intermediates, and then copied them for your kind check.

References:

[1] Gono, P. et al. Effect of the solvent on the oxygen evolution reaction at the TiO_2-water interface. *J. Phys. Chem. C* **123**, 18467-18474 (2019).

[2] Chu, C. et al. Neighboring Pd single atoms surpass isolated single atoms for selective hydrodehalogenation catalysis. *Nat. Commun.* **12**, 5179 (2021).

[3] Yang, G. et al. Regulating Fe-spin state by atomically dispersed Mn-N in Fe-N-C catalysts with high oxygen reduction activity. *Nat. Commun.* **12**, 1734 (2021).

[4] Liu, J. et al. Electrochemical potential-driven shift of frontier orbitals in M–N–C single-atom catalysts leading to inverted adsorption energies. *J. Am. Chem. Soc.* **145**,

46, 25264-25273 (2023).

In **Line 357-360**:

"Noting that the above OER results were based on implicit solvent model (VASPsol), which can generally capture the electrostatic interaction with diverse intermediates, neglect the influence of hydrogen bond on their stabilization and consequent OER mechanism using explicit solvent model.[51]"

Our revision: We have revised our manuscript according to the reviewer's suggestion (**Line 357-360**).

Comment 4: *In conclusion, the approximations done in the theoretical part are rather severe, and they will certainly impact the final results. The authors should perform some additional calculations to check that the method adopted is sufficient to grasp the complexity of the catalyst studied. This can provide a more robust and credible support to the experimental results reported in the paper.*

Response: We thank the reviewer for the constructive suggestions. We have answered these questions by point-to-point response. Based on the first question about the self-interaction of transition metal 3d Fe element, the DFT+U method (effective U = 4 eV for Fe element) was applied to evaluate the OER performance for the *A*-$Fe_2S_1N_5$/SNC, Fe_2N_6/NC, and $Fe_1S_1N_3$/NC catalyst. Combined with the second question about the unconventional OER intermediates on the single-atom catalyst, we systematically calculated all the intermediates composed of classical and unusual ones to assess the OER mechanism. The third question is about the effect of explicit solvent on the

stabilization of different intermediates. Given its huge computational cost, we declared a notice about the impact of explicit solvent on the OER intermediates in the revised manuscript. Above all the questions. We all presented elaborate simulation results and discussion in our revised manuscript.

Our revision: We have revised our manuscript according to the reviewer's suggestion (**Fig. 4, Line 309-393,** and **Line 456-539** in the revised manuscript, **Supplementary Figs. 62-84, Supplementary Tables 9-16**).

Response to Reviewer 3：

I co-reviewed this manuscript with one of the reviewers who provided the listed reports. This is part of the Nature Communications initiative to facilitate training in peer review and to provide appropriate recognition for Early Career Researchers who co-review manuscripts.

Response: Thanks for your valuable advice and professional comment to help us improve the manuscript. Your suggestions and comments have been carefully considered and addressed, and all the responses are listed in the following section, point by point.

Response to Reviewer 4：

Title: High-density asymmetric iron dual-atom sites for efficient and ultra-stable electrochemical water oxidation. The present manuscript demonstrates the synthesis of asymmetric A-$Fe_2S_1N_5$/SNC dual atom catalysts via two-step thermal annealing approaches. Initially, the authors fabricated SNC support using 2-benzimidazolethiol and melamine, while in the second Fe salt, melamine, and trimesic acid were used for implanting Fe sites in the S, N-doped graphenic structures. The developed materials were characterized using AC-HAADF, STEM, XPS, and XAS measurements. XANES and EXAFS data fitting probe the proposed structure. The presence of high-density Fe dual sites (6.72 wt%) and S coordination was attributed to the increased OER performance compared to symmetric Fe_2-NC and Fe_1-NC structures. In OER a reduced potential of 193 mV at 10 mA cm^{-2} was obtained while catalyst stability was maintained

for 2000 h. The mechanism was thoroughly studied using DFT and in-situ XAS measurement. The scope of synthesis was explored for other 3d transition metals and ORR and Zn-Air battery application was also investigated. The manuscript provides appreciable analysis and enhanced performance however few questions related to the origin of exact coordination should be addressed before consideration of manuscript for the publication.

Response: We truly thank the reviewers for their careful reading and constructive comments. All the insightful comments have been thoroughly considered, and we have performed a series of additional experiments to address all the concerns raised by the reviewer. The corresponding revisions have been made (please see the below).

1. The graphical abstract of the study is missing. A nice sketched graphical abstract portraying the main finding of the manuscript should be added.

Response: We appreciate the valuable comments from the reviewer. The graphical abstract can express the central idea of the manuscript clearly. Following your suggestion, we have added the graphical abstract to help illustrate the main finding of the manuscript (**Fig. R12**).

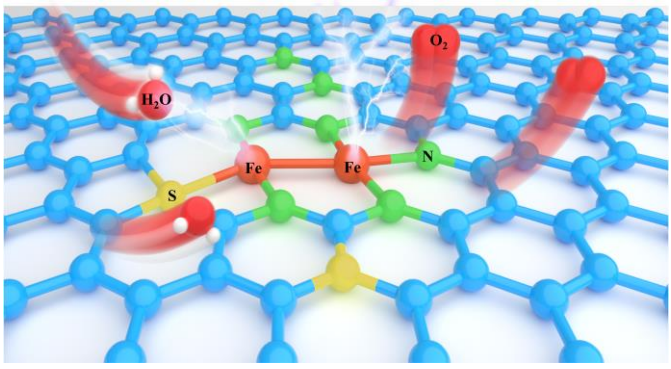

Fig. R12. The graphical abstract of the *A*-$Fe_2S_1N_5$/SNC.

Our revision: We have revised our manuscript according to the reviewer's suggestion (**Line 712-713** in the revised manuscript).

2. The authors claimed that ~81% of sites were present as dual S coordinated sites. The S content of materials should be determined using CHNS analysis and compared with the given number.

Response: Thank you for your rigorous comment. According to your recommendation, we carried out the CHNS analysis to ascertain the precise S content of the materials. Results demonstrate that the S content of *A*-$Fe_2S_1N_5$/SNC was quantified at 1.775 wt% through the CHNS technique (**Table R5**). The content of the S element tested by CHNS is consistent with the results of EDS elemental analysis (0.71 at%) and XPS test (0.65 at%) presented in **Fig. R13**.

Table R5. Light elements contents in the *A*-$Fe_2S_1N_5$/SNC using CHNS analysis.

Samples	C wt%	N wt%	S wt%	H wt%
A-$Fe_2S_1N_5$/SNC	80.05	11.55	1.775	0.098

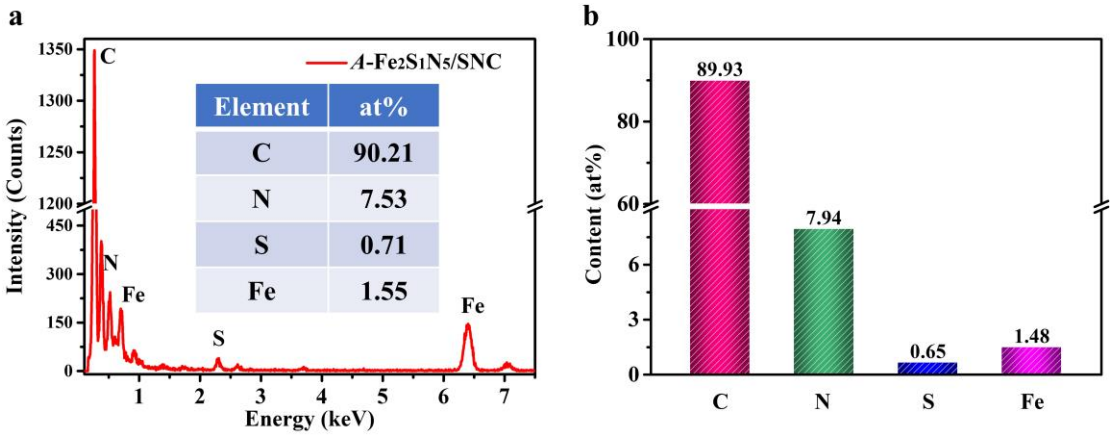

Fig. R13. (a) EDS spectrum of *A*-$Fe_2S_1N_5$/SNC. The element content in *A*-$Fe_2S_1N_5$/SNC was also labeled in the quantitative EDS spectrum. (b) The atomic content percentages of C, N, S, and Fe in *A*-$Fe_2S_1N_5$/SNC were measured by XPS analysis.

Our revision: We have revised our manuscript according to the reviewer's suggestion (**Line 158-159** in the revised manuscript, **Supplementary Fig. 6b, Fig. 24b,** and **Supplementary Table 2**).

3. A significant portion of S 2p spectra demonstrated the presence of SO_x species. However, these are not considered in the DFT calculation. What was the origin of SO_x sites if the catalyst was prepared in an N_2 environment? Do these species influence the OER activity?

Response: We appreciate the valuable comments from the reviewer. A significant portion of S 2p spectra demonstrated the presence of SO_x species. However, these are not considered in the DFT calculation. Because the catalyst was prepared in an N_2 environment, to investigate the origin of SO_x sites, the Fourier transform infrared spectroscopy (FTIR) and solid-state nuclear magnetic resonance (NMR) spectroscopy were conducted. **Fig. R14** displays the FTIR spectrum of the *A*-$Fe_2S_1N_5$/SNC catalyst. The spectrum in **Fig. R14a** reveals the presence of numerous sulfur-containing and nitrogen-containing terminal groups on the surfaces of *A*-$Fe_2S_1N_5$/SNC. The characteristic absorptions at 1350-1300 and 1160-1120 cm^{-1} are attributed to the stretching vibrations of S=O.[1-4] For *A*-$Fe_2S_1N_5$/SNC, no distinctive absorptions

belonging to S=O groups was found in **Fig. R14b**, which indicate the inexistence of SO_x in *A*-$Fe_2S_1N_5$/SNC. Additionally, the solid-state ^{13}C MAS NMR spectrum of *A*-$Fe_2S_1N_5$/SNC is performed. As illustrated in **Fig. R15**, the *A*-$Fe_2S_1N_5$/SNC exhibits a wide peak at 123 ppm accompanied by a secondary peak at 127.9 ppm, corresponding to sp^2 carbons and C=S, respectively. The absence of peaks at 140.8 ppm confirmed the absence of the C-SO_x moiety in *A*-$Fe_2S_1N_5$/SNC.[5-7] During XPS analysis, the incidence of high-energy X-rays on the sample surface can lead to oxidation. This is attributed to the sufficient energy of the X-rays to disrupt surface chemical bonds, resulting in heightened reactivity of the atoms and facilitating their interaction with oxygen. The occurrence of sample oxidation induced by X-rays necessitates careful consideration during experimentation, as it has the potential to impact the reliability of XPS test outcomes and compromise the precise evaluation of sample composition and chemical state. Consequently, only the S2p XPS analysis indicates the existence of SO_x species, which may be derived from the partial surface oxidation in *A*-$Fe_2S_1N_5$/SNC during the XPS test.

Recent studies have demonstrated that the addition of sulfur can create defects and electron-rich sites in carbon-based catalysts, leading to enhanced electrocatalytic activity. Additionally, the incorporation of sulfur into a metal-N-C single atom catalyst through metal sulfidation can improve the OER activity. Hence, an in-depth examination was conducted to explore the enhancement of catalytic activity in metal-N-C single atom catalysts by incorporating sulfur doping. The phenomenon that the S 2p XPS analysis demonstrated the presence of SO_x species in the metal-N-C single

atom catalyst is common in the reported literature. For example, Zhang et al. prepared a meso-FeNSC catalyst by a sequential synthesis route with the precise FeN_2S_2 site. The S 2p XPS spectra of meso-FeNSC show a broad peak at ~167.0 eV, which corresponds to the SO_x species.[8] Zhang et al. fabricated a novel catalyst consisting of single In atoms by rational coordination engineering and it was precisely modulated by first coordination with nitrogen and sulfur, and second coordination with boron in the hollow carbon rods (In SAs/NSBC). For the S 2p XPS spectrum of In SAs/NSBC, the peak at 168.6 eV is ascribed to the existence of oxidized S species (C-SO_x-C).[9] Chen et al. prepared a Co/Fe dual-metal-site catalyst (Co/Fe-SNC800) using the reverse-micelle assembly-pyrolysis strategy. The configuration of the dual-metal site in Co/Fe-SNC800 is dominated by FeN_3-CoN_2S coordination. The high-resolution S 2p XPS spectra of Co/Fe-SNC800 also show an oxidized S peak at the binding energy ~ 168.0 eV.[10] Pei et al. synthesized a series of Co-S_xN_{4-x} (x = 0, 1, 2, 3) single-atom catalysts by thermally replacing coordinated N with S at elevated temperatures. The high-resolution S 2p XPS spectrum shows a peak at 168.4 eV, which can be assigned to the C-SO_x-C.[11] Xiang et al. engineered metal-free carbon fibers with a fluorine and sulfur dual-doping strategy. From the high-resolution S 2p spectra, the peak centered at 168.7 eV corresponded to oxidized sulfur groups C-SO_x-C (x =1, 2, 3).[12]

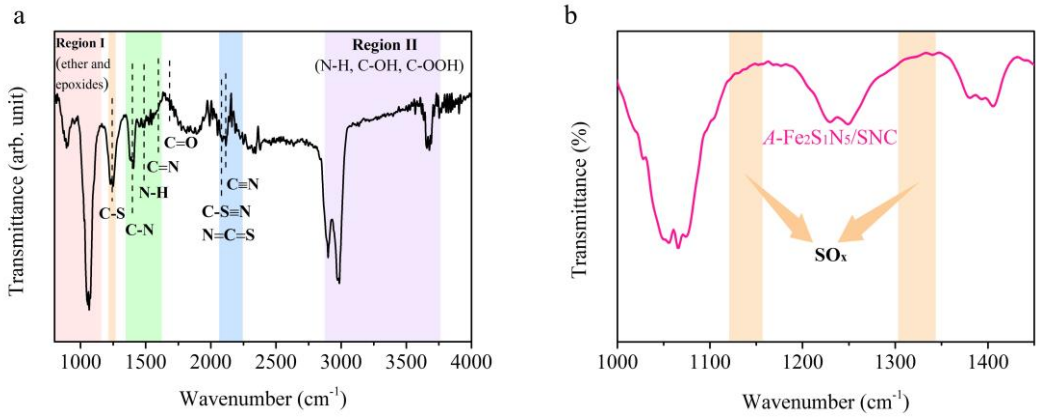

Fig. R14. FTIR spectrum of the *A*-$Fe_2S_1N_5$/SNC catalyst.

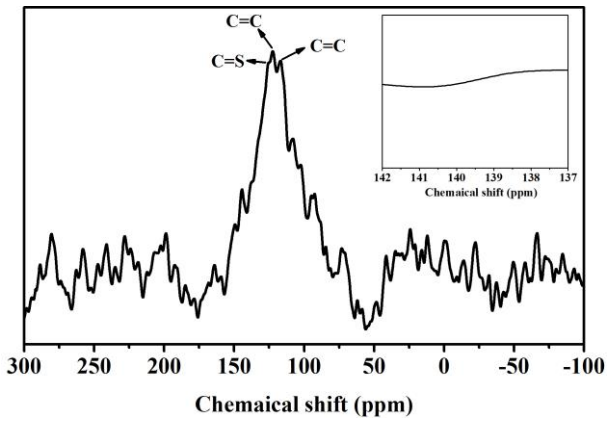

Fig. R15. ^{13}C MAS solid-state NMR of the *A*-$Fe_2S_1N_5$/SNC catalyst.

References:

[1] Das Manisha. et al. Electronic interplay: synergism of binary transition metals and role of M-N-S site towards oxygen electrocatalysis, *Chem. Commun.* **58**, 1934-1937 (2022).

[2] Liu, C. et al. One-dimensional van der waals heterostructures as efficient metal-free oxygen electrocatalysts, *ACS Nano* **15**, 3309-3319 (2021).

[3] Huo, L. et al. Amorphous MnO_2 lamellae encapsulated covalent triazine polymer-derived multi-heteroatoms-doped carbon for ORR/OER bifunctional electrocatalysis, *Adv. Mater.* 2312868 (2024).

[4] Zhou, X. et al. Hierarchical polyphosphazene@molybdenum disulfide hybrid structure for enhancing the flame retardancy and mechanical property of epoxy resins, *ACS Appl. Mater. Interfaces* **9**, 29147-29156 (2017).

[5] Nicolas Oger. et al. Practical and scalable synthesis of sulfonated graphene, *Carbon* **96**, 342e350 (2016).

[6] Li, Z. et al. N/S dual-doped graphene with high defect density for enhanced supercapacitor properties. *International Journal of Hydrogen Energy* **45**, 112-122 (2019).

[7] Zhang, Q. et al. S edge/center-selectively doped graphene oxide for bisphenol A electro-degradation: Preparation, efficiency and mechanism, *Chemical Engineering Journal* **420**, 127669 (2021).

[8] Zhang, W. et al. Two-electron redox chemistry via single-atom catalyst for reversible zinc-air batteries, *Nature Sustainability* **7**, 463-473 (2024).

[9] Su, H. et al. Flexibility tuning of dual-metal S-Fe-Co-N_5 catalysts with O-axial ligand structure for electrocatalytic water splitting, *Adv. Energy Mater*. **13**, 2301547 (2023).

[10] Chen, C. et al. Adjacent Fe site boosts electrocatalytic oxygen evolution at Co site in single-atom-catalyst through a dual-metal-site design, *Energy Environ. Sci.* **16**, 1685-1696 (2023).

[11] Pei, J. et al. A replacement strategy for regulating local environment of single-atom Co-S_xN_{4-x} catalysts to facilitate CO_2 electroreduction. *Nat. Commun*. **15**, 416 (2022).

[12] Xiang, F et al. Enhanced selectivity in the electroproduction of H_2O_2 via F/S dual-

doping in metal-free nanofibers, *Adv. Mater*. **35**, 2208533 (2023).

Our revision: We have revised our manuscript according to the reviewer's suggestion (**Line 206-210** in the revised manuscript, **Supplementary Figs. 30-31**).

4. The introduction needs slight improvement. The authors stated, "…due to their symmetric electron distribution." How the symmetric distribution of M2 sites on M2-N-C catalysts reduces the performance in OER should be explained. The authors should give some examples of cooperative catalysis by dual atom sites.

Response: We greatly appreciate your constructive comments. In recent decades, single-atom catalysts (SACs) have aroused significant interest owing to their maximal atomic utilization and well-defined coordination structure.[1] This presents an excellent opportunity to explore the potential correlations between structure and activity by integrating experimental and theoretical findings effectively.[2] As an extension of single metal site catalysts, dual-atom catalysts (DACs) have recently emerged as ideal candidates for fabricating OER electrocatalysts with encouraging activity, which not only inherits the advantages of M-N-C SACs but also permits qualitative (new binding sites) and quantitative (new binding modes) changes to occur within catalytic centers to break down the intrinsic activity limitations.[3]

The rational design of DACs has become a promising approach to elevating the intrinsic activity of catalysts. First, DACs provide a microenvironment optimization strategy to adjust contributing metal centers by short/medium-range interaction with another metal site.[4] Second, DACs own synergetic effects: two metal centers separately

catalyze different core steps to improve the catalytic performance together.[5] Third, reaction intermediates are allowed to simultaneously adsorb on dual-metal sites, thus breaking the strong scaling relationship limit based on conventional SACs.[6]

The heterogeneous nature of the coordination configuration may give rise to the formation of distinct catalytic active sites and reaction pathways, which in turn can influence the overall catalytic performance. Moreover, the atomic spatial configuration, the surrounding chelating atoms, and the coordination number are of paramount importance in optimizing the coordination environment of DACs. Accordingly, the dual-metal sites can be classified into three categories based on their coordination environment: binuclear homologous dual-metal sites, binuclear heterologous dual-metal sites, and isolated dual-metal sites. Among these, the symmetric distribution of M_2 sites on M_2-N-C DACs belongs to the binuclear homologous dual-metal site pairs. They will owe higher metal loading than the isolated metal site catalysts, due to the preferred diatomic pairs at high metal loading. As we know, the OER involves multiple proton-coupled electron transfer processes and the symmetric distribution M_2-N-C DACs possess unitary active sites, which make it difficult to achieve the optimal adsorption state of multiple reaction intermediates. Consequently, asymmetrical charge distribution on homonuclear dual-metal sites can maximize the potential of DACs for multistep reactions, which makes the optimization of activity and selectivity feasible. There are three common strategies to break the shackles of symmetry.

(i) Construct heteronuclear diatomic catalysts. The heteronuclear diatomic catalysts with two linked heterometal sites have asymmetric electronic structures. To

date, a series of heterometal diatomic sites, such as FeN4-CoN4, NiN4-FeN4, MnN4-FeN4, etc., have been constructed for promoting the OER activity.[7,8] Compared to the symmetric diatomic sites, the asymmetric diatomic sites with optimized coordinated configurations have more potential for OER, due to their ability to accelerate the electron transport and optimize the adsorption of intermediates.[9] Hence, the accurate construction of asymmetric diatomic sites and studying their electronic regulation effect are of tremendous fundamental and practical significance for OER. For example, Zeng et al. synthesized DACs consisting of nickel-iron hetero-diatomic pairs anchored on nitrogen-doped graphene. The orbital coupling between the catalytic iron center and the adjacent nickel atom leads to alteration in orbital energy level, asymmetric electronic states, higher oxidation state of iron, and weakened binding strength to the reaction intermediates, thus boosting OER performance.[10] Xiao et al. modulate the Co d-orbital electron configuration by constructing the Ir-Co atomic pair toward boosted bifunctional oxygen activities. Symmetry-breaking charge transfer happens on asymmetric dual-atom $IrCoN_5$ sites, resulting in charge polarization and electron redistribution.[11] Duan et al. reported a Fe-Ni dual-site catalyst (Fe-Ni-N-P-C), whose local doping of P and asymmetric Fe-Ni dual site comprehensively improve the OER catalytic performance.[12]

(ii) Introducing nonmetal to modify the specific coordination conditions around M for the M-N materials. Nonmetal (B, O, P, or S) coordination can effectively regulate the adsorption strength of and reduce the reaction energy barrier of intermediates.[13-16] Tuning both the type and chemical environment of the coordinated atoms can break the

electron/geometric symmetry of the M_2-N_6 catalyst.[17] This approach can elongate the M-N bond or slightly pull metal atoms out of the pristine plane, which polarizes the charge distribution and tunes the d-band center of metal centers, thus reducing the binding energies for OER intermediates.[18,19] For instance, Su et al. reported a dual-metal S-Fe-Co-N_5 catalyst is constructed by embedding Fe and S into the structure of Co-N_4 motifs. Theoretical analysis and in situ characterizations illustrate that the active sites will in situ combine an O-axial ligand to form the S-Fe-Co-N_5-O structure during the OER, which can reduce the reaction energy of O*→OOH*.[20]

(iii) The adjusting effect for breaking symmetry can also be achieved by introducing a nonmetallic heteroatom into the graphene skeleton. The indirect bonding environment from the substrates, such as O, S, or P doped on the substrate, can affect the catalytic activity and/or selectivity of the active center structures. Adjustment of the microenvironment of typical M-N4 active sites by S doping can effectively tune the electronic structure of SACs and optimize the adsorption strength of reaction intermediates for higher catalytic activity.[21] The additional S atoms induced uneven charge distribution on the N, S codoped carbon framework, resulting in positively charged C atoms, which was favorable for the adsorption of oxygen species. For example, Fe-N_x species on N, S codoped carbon (C-S-C) was prepared, in which the S salt could significantly improve the surface area of the resultant catalyst, leading to more active sites for the catalytic reaction.[22] The additional S atoms induced uneven charge distribution on the N, S codoped carbon framework, resulting in positively charged C atoms, which was favorable for the adsorption of oxygen species. As a result,

the combination of N and S co-decoration and the atomically dispersed Fe-N_x species led to superior activity in the Zn-air battery.[23]

References:

[1] Meng, H. et al. Optimizing electronic synergy of atomically dispersed dual-metal Ni-N_4 and Fe-N_4 sites with adjacent Fe nanoclusters for high efficiency oxygen electrocatalysis, *Energy Environ. Sci.* **17**, 704-716 (2024).

[2] Li, Z. et al. Engineering the electronic structure of single-atom iron sites with boosted oxygen bifunctional activity for zinc-air batteries, *Adv. Mater*. **35**, 2209644 (2023).

[3] Zhong, D. et al. Dinuclear metal synergistic catalysis for energy conversion, *Chem. Soc. Rev.* **52**, 3170-3214 (2023).

[4]. Lei, L. et al. From synthesis to mechanisms: in-depth exploration of the dual-atom catalytic mechanisms toward oxygen electrocatalysis. *Adv. Mater.* 2311434 (2024).

[5]. Yang, G. et al. Regulating Fe-spin state by atomically dispersed Mn-N in Fe-N-C catalysts with high oxygen reduction activity. *Nat. Commun.* ***12***, 1734 (2021).

[6]. Li, L. et al. Breaking the scaling relationship limit: from single-atom to dual-atom catalysts. *Acc. Mater. Res.* ***3***, 584-596 (2022).

[7] Zhou, X. et al. Theoretically revealed and experimentally demonstrated synergistic electronic interaction of CoFe dual-metal sites on N-doped carbon for boosting both oxygen reduction and evolution reactions, *Nano Lett*. **22**, 3392-3399 (2022).

[8] Cui, T. et al. Engineering dual single-atom sites on 2D ultrathin N-doped carbon nanosheets attaining ultra-low-temperature zinc-air battery, *Angew. Chem. Int. Ed*. **61**,

e202115219 (2022).

[9] Zang, W. et al. Heterogeneous single atom electrocatalysis, where “singles” are “married”, *Adv. Energy Mater*. **10**, 1903181 (2020).

[10] Zeng, Z. et al. Orbital coupling of hetero-diatomic nickel-iron site for bifunctional electrocatalysis of CO_2 reduction and oxygen evolution, *Nat. Commun*. **12**, 4088 (2021).

[11] Xiao, M. et al. 3d-orbital occupancy regulated Ir-Co atomic pair toward superior bifunctional oxygen electrocatalysis, *ACS Catal*. **11**, 8837-8846 (2021).

[12] Pan, F. et al. Theory-guided design of atomic Fe-Ni dual sites in N, P-co-doped C for boosting oxygen evolution reaction, *Chem Catalysis* **1**, 734-745 (2021).

[13] Zhou, Y. et al. Boosting oxygen electrocatalytic activity of Fe-N-C catalysts by phosphorus incorporation, *J. Am. Chem. Soc*. **145**, 3647-3655 (2023).

[14] Wang, X. et al. Atomically dispersed pentacoordinated-zirconium catalyst with axial oxygen ligand for oxygen reduction reaction. *Angew. Chem. Int. Ed*. **61**, e202209746 (2022).

[15] Cui, H. et al. Dynamics of non-metal-regulated FeCo bimetal microenvironment on oxygen reduction reaction activity and intrinsic mechanism, *Nano Res.* **16**, 2199 (2023).

[16] Li, Y. et al. High-valence nickel single-atom catalysts coordinated to oxygen sites for extraordinarily activating oxygen evolution reaction, *Adv. Sci*. **7**, 1903089 (2020).

[17] Hu, Y. et al. Recent progress of diatomic catalysts: general design fundamentals and diversified catalytic applications, *Small* **18**, 2203589 (2022).

[18] Li, R. et al. Superiority of dual-atom catalysts in electrocatalysis: one step further

than single-atom catalysts, *Adv. Energy Mater*. **12**, 2103564 (2022).

[19] Shang, H. et al. Atomic design of carbon-based dual-metal site catalysts for energy applications, *Nano Res*. **16**, 6477-6506 (2023).

[20] Su, H. et al. Flexibility tuning of dual-metal S-Fe-Co-N_5 catalysts with O-axial ligand structure for electrocatalytic water splitting, *Adv. Energy Mater*. **13**, 2301547 (2023).

[21] Chen, Z. et al. Mass production of sulfur-tuned single-atom catalysts for Zn-air batteries, *Adv. Mater*. **35**, 2209948 (2023).

[22] Shen, H. et al. Synergistic effects between atomically dispersed Fe@N@C and C@S@C for the oxygen reduction reaction in acidic media, *Angew. Chem. Int. Ed*. **56**, 13800-13804 (2017).

[23] Han, Y. et al. Electronic structure engineering to boost oxygen reduction activity by controlling the coordination of the central metal, *Energy Environ. Sci.*, **11**, 2348-2352 (2018).

Our revision: We have revised our manuscript according to the reviewer's suggestion (**Line 56-71** in the revised manuscript).

5. The BET surface area of catalysts should be provided and compared with the ECSA.

Response: We appreciate your thorough examination, as it contributes to enhancing the overall quality of this work. N_2 adsorption and desorption isotherms (**Fig. R16a**) revealed that the *A*-$Fe_2S_1N_5$/SNC, $Fe_1S_1N_3$/NC, Fe_2N_6/NC, Fe_1N_4/NC, and SNC catalysts had a comparable Brunauer-Emmett-Teller (BET) specific surface area. The

pore size distribution analysis using the Barrett-Joyner-Halenda (BJH) model (**Fig. R16b**) displayed a narrow peak around 2.3 nm. The relevant data can be found in **Table R6**.

The ECSA was determined by: $ECSA = C_{dl}/C_s$, where C_{dl} is double-layer capacitance and C_s is the specific capacitance of the sample. In this study, a general specific capacitance of $C_s = 0.035\ mF\ cm^{-2}$ was used based on the typical reported value.[1,2] C_{dl} was determined by the equation $C_{dl} = i_c/\nu$, where i_c is the charging current and ν is the scan rate. A series of CV tests in the non-faradaic potential region under different scan rates (20, 40, 60, 80, 100, and 120 $mV\ s^{-1}$) were performed (**Fig. R17**). By plotting measured i_c versus ν, C_{dl} was obtained from the slopes of the linear fitting (**Fig. R18**). The ECSAs for different catalysts are shown in **Table R7**. Results indicate that the *A*-$Fe_2S_1N_5$/SNC achieves the highest specific surface area and electrochemical active area. Additionally, *A*-$Fe_2S_1N_5$/SNC displays the largest ECSA and the highest ECSA normalized LSV curves (**Fig. R19**) as well, demonstrating its high intrinsic OER activity.

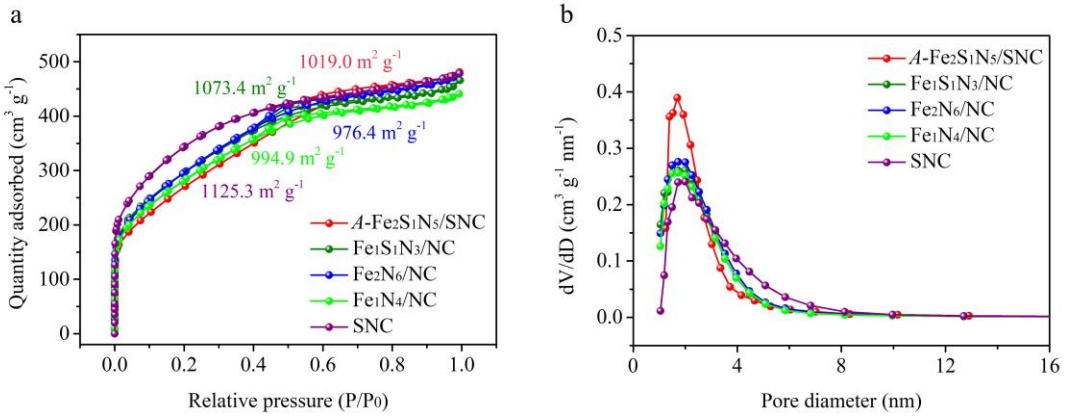

Fig. R16. BET analyses of *A*-$Fe_2S_1N_5$/SNC, $Fe_1S_1N_3$/NC, Fe_2N_6/NC, Fe_1N_4/NC, and SNC catalysts. (a) N_2 adsorption and desorption isotherms. (b) The corresponding pore-

size distributions.

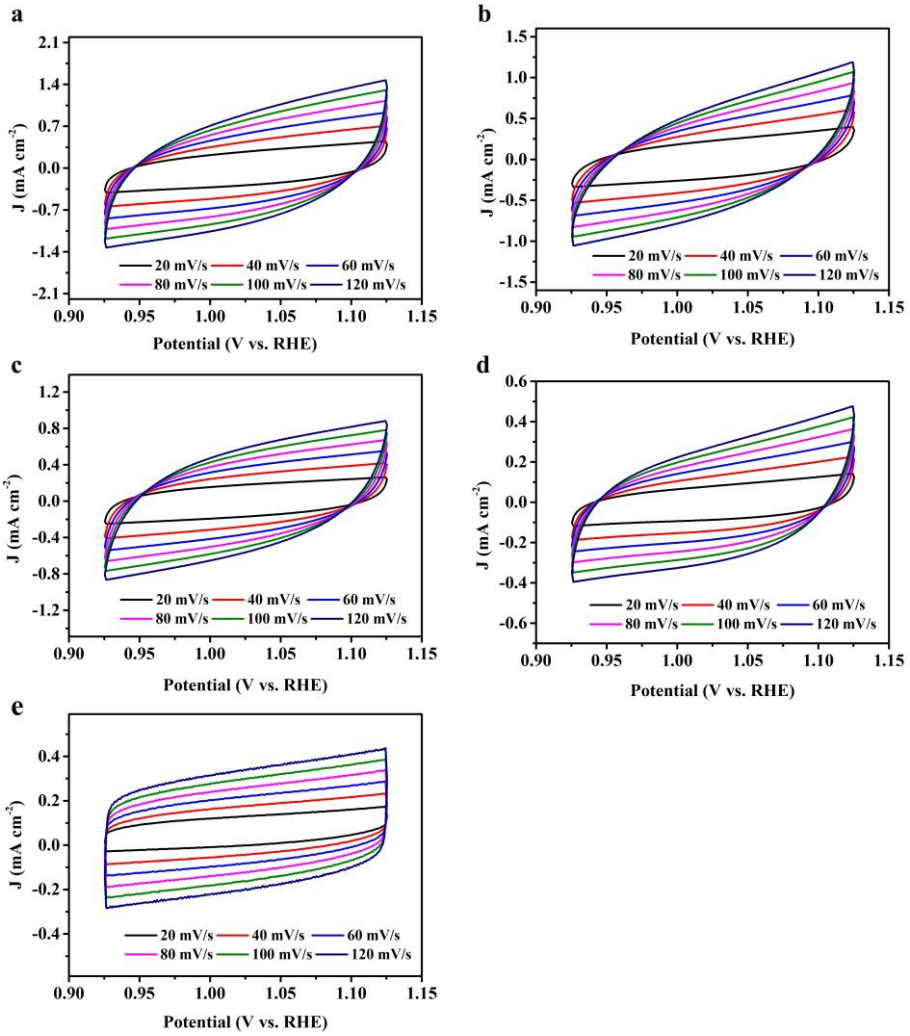

Fig. R17. CV plots at various sweep rates of (a) *A*-$Fe_2S_1N_5$/SNC, (b) $Fe_1S_1N_3$/NC, (c) Fe_2N_6/NC, (d) Fe_1N_4/NC, and (e) SNC for OER.

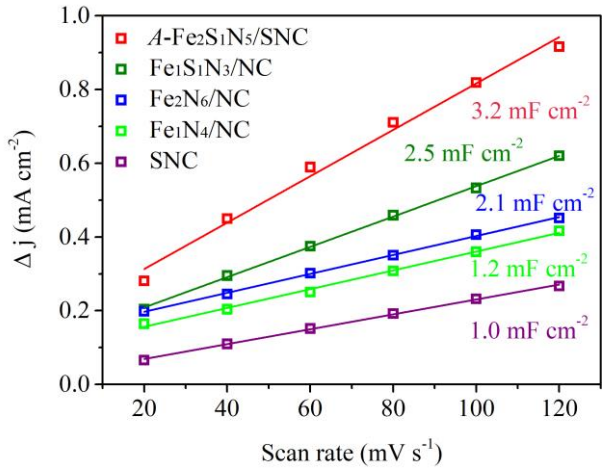

Fig. R18. Calculated C_{dl} values of *A*-$Fe_2S_1N_5$/SNC, $Fe_1S_1N_3$/NC, Fe_2N_6/NC, and

Fe_1N_4/NC, and SNC.

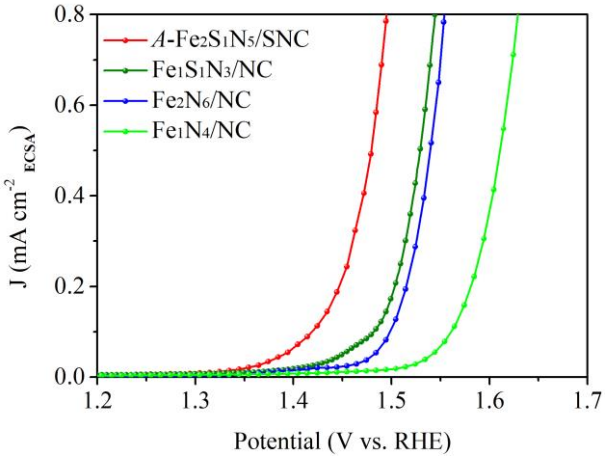

Fig. R19. ECSA-normalized LSV curves of *A*-$Fe_2S_1N_5$/SNC, $Fe_1S_1N_3$/NC, Fe_2N_6/NC, and Fe_1N_4/NC.

Table R6. The porosity of as-prepared catalysts.

Samples	**S_{BET}** ($m^2\ g^{-1}$)	**Total pore volume** ($cm^3\ g^{-1}$)	**Average pore diameter** (nm)
A-$Fe_2S_1N_5$/SNC	1019.0	0.7294	2.42
$Fe_1S_1N_3$/NC	1073.4	0.7109	2.31
Fe_2N_6/NC	976.4	0.7391	2.35
Fe_1N_4/NC	994.9	0.7109	2.31
SNC	1125.3	0.7511	2.75

Table R7. Calculated C_{dl} and ECSA values for different catalysts.

Catalyst	**C_{dl} (mF)**	**ECSA (cm^2)[a]**
A-$Fe_2S_1N_5$/SNC	3.2	91.4
$Fe_1S_1N_3$/NC	2.5	71.4
Fe_2N_6/NC	2.1	60.0

Fe_1N_4/NC	1.2	28.6

[a] ECSAs are determined by the equation of ECSA = $C_{dl}/C_s \times S$ and S is the electrode area (1.0 cm^2).

References:

[1] Wu, Z.-Y. et al. Non-iridium-based electrocatalyst for durable acidic oxygen evolution reaction in proton exchange membrane water electrolysis. *Nat. Mater*. **22**, 100-108 (2022).

[2] Qin, Y. et al. RuO_2 electronic structure and lattice strain dual engineering for enhanced acidic oxygen evolution reaction performance, *Nat. Commun*. **13**, 3784 (2022).

Our revision: We have revised our manuscript according to the reviewer's suggestion (**Line 153-157** and **Line 225-231** in the revised manuscript, **Supplementary Fig. 14, Supplementary Figs. 35-37,** and **Supplementary Table 1** and **Table 4**).

6. *Considering the C/N and metal content. Can the authors predict the distance of Fe sites in a graphenic network? Since it is a high concentration, I think the calculated distance might be just for the uniformly distributed Fe single-atom sites. How about the possibility of the presence of a mixture of Fe-N_4-C and Fe-N_3S-C sites?*

Response: Thank you for your comment. Considering the C/N and metal content, we predict the distance of Fe sites in a graphenic network. Since it is a high concentration, we calculated the distance of Fe sites if they were uniformly distributed as Fe single-atom sites. X-ray photoelectron spectroscopy (XPS) is employed to determine the

number of atoms in *A*-$Fe_2S_1N_5$/SNC, which is then used to calculate the mass of the atoms. According to the Brunauer-Emmett-Teller (BET) surface area, the distance of Fe sites was calculated to be approximately 12.16 Å. The comprehensive calculation process is illustrated in **Table R8**. The calculated distance of Fe sites is approximately 12.16 Å, if they were uniformly distributed as Fe single-atom sites, which is considerably larger than the bond length of Fe-Fe bonds (2.56 Å) obtained from EXAFS analysis. Therefore, in the *A*-$Fe_2S_1N_5$/SNC, the iron exists in the form of atomic pairs rather than as single sites.

Table R8. The calculation of average Fe-Fe distance based on XPS elemental content and BET surface area analysis.[1]

Number of atoms in *A*-$Fe_2S_1N_5$/SNC (at% XPS)			
C	N	S	Fe
89.93	7.94	0.65	1.48
100 atoms in total			
Mass of atoms (g)			
C	N	S	Fe
1.79×10^{-21}	1.85×10^{-22}	3.46×10^{-23}	1.37×10^{-22}
Total mass of atoms in *A*-$Fe_2S_1N_5$/SNC: 21.47×10^{-22} g			
Surface area calculations			
1 g of *A*-$Fe_2S_1N_5$/SNC	occupies	1019 m^2 (the experimental value)	
21.47×10^{-22} g of *A*-$Fe_2S_1N_5$/SNC	occupies	218.78×10^{-20} m^2 or 218.78 $Å^2$	
1.48 Fe atoms	occupy	218.8 $Å^2$ or 1 Fe atom occupies ~147.8 $Å^2$	

Fe-Fe distance = $\sqrt{147.8} = 12.16$ Å.

Furthermore, the statistical analysis of the site distributions was conducted by counting the pair distance for more than 140 sites (specifically 140 groups of metal sites) on the AC-STEM image of *A*-$Fe_2S_1N_5$/SNC. Among the identified sites, the Fe-Fe dual

sites were highlighted by a yellow ellipse (**Fig. R20**). The majority of the dots were counted as dot pairs above 80.8%, which represent the bimetallic dual sites. The Fe-Fe diatomic distance is primarily situated between 2.4 and 2.6 Å, accounting for more than 80%, which is consistent with the reported distance of bonded diatoms.[2-5] Recently, Zhang et al. reported the development of a planar-like Fe_2N_6 structure that exhibits a notable catalytic mechanism for oxygen reduction.[6] The interatomic spacing at the Fe-Fe sites was measured to be 2.47 ± 0.03 Å, which aligns with the primary distribution observed in our statistical analysis. As a result, our manuscript shows that the atomic spacing of the double Fe atom sites aligns closely with the distances documented in existing literature. This observation supports the assertion that the majority of metals exhibit the formation of Fe-Fe double sites in *A*-$Fe_2S_1N_5$/SNC.

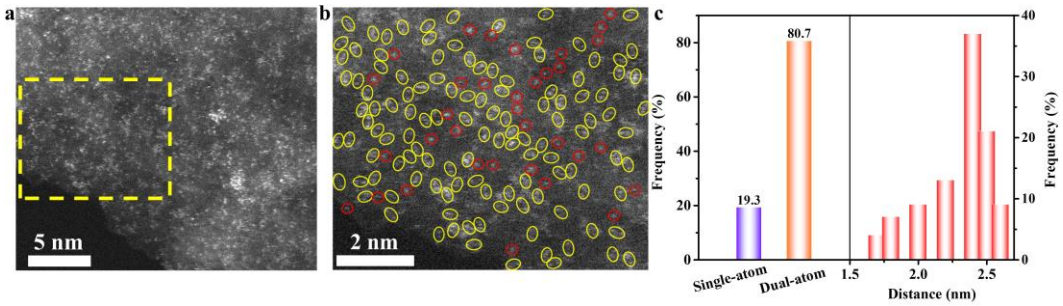

Fig. R20. (a-b) AC-STEM image. The dual Fe sites were signed by the yellow oval. (c) The statistical density of the Fe-Fe dual sites and Fe single sites, as well the Fe-Fe diatomic distance from the AC-STEM images shown in (b).

As shown in **Fig. R21a**, EXAFS spectra for $Fe_1S_1N_3$/NC and Fe_1N_4/NC displayed a prominent peak at approximately 1.50 Å, indicating the dominant Fe-N coordination. In comparison to Fe foil, no significant Fe-Fe signal was detected, suggesting the formation of atomically dispersed Fe single-atom catalysts. For the *A*-$Fe_2S_1N_5$/SNC

sample, a prominent characteristic peak was observed at 1.50 Å, whereas an obvious signal peak and a shoulder peak, corresponding to the presence of Fe-Fe bond and Fe-S, were detected at 2.27 and 1.84 Å, respectively. The quantitative EXAFS fitting results indicated that the Fe atoms were coordinated as FeS_1N_2-FeN_3 atomic interface sites on the SNC matrix. In addition, we provide precise fitting paths attributed to the Fe-N, Fe-S, and Fe-Fe paths, respectively (**Fig. R21b**). The scattering peak located at 2.27 Å is in good agreement with the Fe-Fe bond, which further indicates that there are certain Fe dual atoms sites in *A*-$Fe_2S_1N_5$/SNC. Combining the AC-STEM and FT-EXAFS characterization results, for *A*-$Fe_2S_1N_5$/SNC catalyst, most of the Fe atoms exist in an asymmetric diatomic configuration, and the single atom Fe sites (such as Fe-N_4-C and Fe-N_3S-C) may also exist simultaneous.

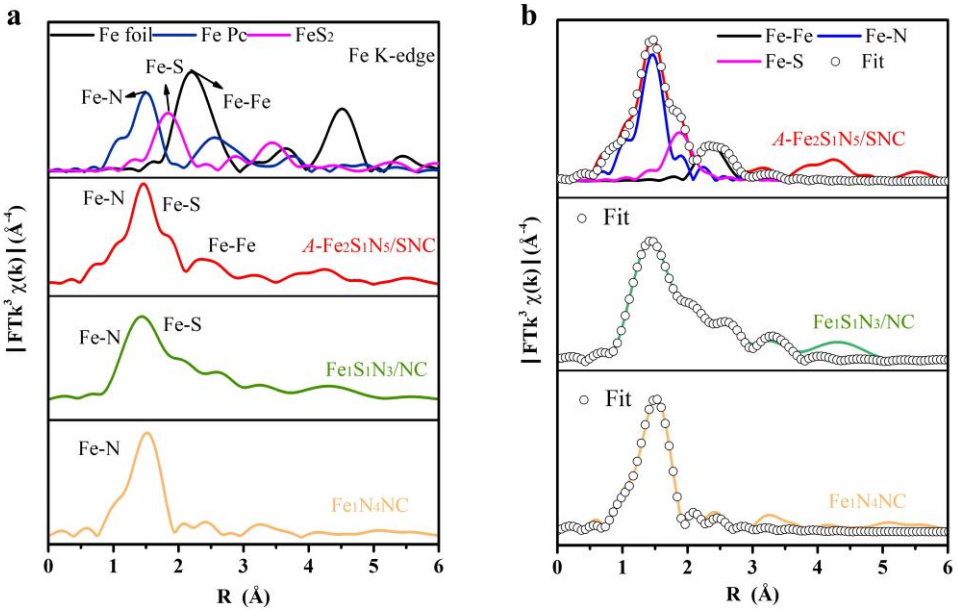

Fig. R21. (a) FT-EXAFS spectrum of *A*-$Fe_2S_1N_5$/SNC, $Fe_1S_1N_3$/NC, Fe_2N_6/NC, and the references. (b) FT-EXAFS fitting curve of *A*-$Fe_2S_1N_5$/SNC, $Fe_1S_1N_3$/NC, and Fe_2N_6/SNC in R space.

References:

[1] Kumar, P. et al. High-density cobalt single-atom catalysts for enhanced oxygen evolution reaction. *J. Am. Chem. Soc*. **145**, 8052-8063 (2023).

[2] Zhao, Q.-P. et al. Photo-induced synthesis of heteronuclear dual-atom catalysts. *Nature Synthesis* **3**, 497-506 (2024).

[3] Zhang, W.-D. et al. Dual-atom catalysts derived from a preorganized covalent organic framework for enhanced electrochemical oxygen reduction. *Angew. Chem. Int. Ed.* **62**, e202304412 (2023).

[4] Su H. et al. Flexibility tuning of dual-metal S-Fe-Co-N_5 catalysts with O-axial ligand structure for electrocatalytic water splitting, *Adv. Energy Mater*. **13**, 2301547 (2023).

[5] Zhu, X. et al. Harnessing the interplay of Fe–Ni atom pairs embedded in nitrogen-doped carbon for bifunctional oxygen electrocatalysis. *Nano Energy* **71**, 104597 (2020).

[6] Zhang, N. et al. High-density planar-like Fe_2N_6 structure catalyzes efficient oxygen reduction, *Matter* **3**, 509-521 (2020).

Our revision: We have revised our manuscript according to the reviewer's suggestion (**Line 145-147** in the revised manuscript, **Supplementary Fig. 10**).

7. *Indeed, the explanation of how Fe sites are arranged in dual atom sites is missing. Since Fe atoms are free to move (no preorganized metal-organic complex was used) they can form dual atom sites, and triple atom sites as well. What factor promotes a precise organization of Fe sites on SNC sites?*

Response: Thank you for your professional comment. The *A*-$Fe_2S_1N_5$/SNC is primarily

synthesized through a high-temperature thermal migration approach. This method has facilitated the successful development of the precise structural characteristics of atomic-dispersed metal catalysts, including coordination number, dispersion tendencies, and binding modes.[1] Notably, defect anchoring and sulfur capture are among the most prevalent techniques employed in the preparation of atomic-dispersed metal catalysts.[2,3] These methods have proven to be effective strategies for the construction of well-exposed paired atoms, allowing for suitable anchoring sites and controlled loadings.

Two-dimensional graphene-like nanosheets were synthesized through confinement encapsulation pyrolysis, resulting in materials characterized by a high specific surface area, significant nitrogen content, abundant defects, and sulfur doping. During the heating process, nitrogen atoms located at the edges along with adjacent sulfur atoms, can effectively anchor individual Fe atoms through defect capture and sulfur tethering effects.[4,5] Following the initial anchoring, the neighboring Fe atoms are capable of migrating and interacting with one another, resulting in the formation of a Fe-Fe bond on the surface of the graphene substrate. This process is facilitated by the effective metal dispersion and regulation of the heating parameters. After a two-hour annealing treatment at 900 °C, a stable asymmetrically coordination structure characterized by FeN_3-FeS_1N_2 was observed for the Fe-Fe pair. Consequently, the asymmetric nitrogen, sulfur-coordinated diatomic iron centers on highly defective nitrogen-doped carbon nanosheets can be formed.

The synthesis of homonuclear diatomic catalysts through a high-temperature thermal migration approach has been extensively employed in the catalysis field. Xie

et al. presented a groundbreaking study that illustrated the synthesis of Fe_2N_6 clusters utilizing single iron atoms (FeN_4) as precursor materials through a thermal migration approach.[6] Specifically, the formation of the desired Fe_2N_6 clusters occurred after treatment at 650 °C for 2 hours in an argon atmosphere. This single-atom thermal migration process offers a viable method for the synthesis of M_2 dual-atom sites, as demonstrated by the observed low-temperature (greater than 500 °C) thermal migration of corresponding metal single atoms on graphene substrates.[7] Chen et al. reported the synthesis of tungsten dimers (W-ACs, W-W dual-atoms) anchored on P-doped carbon materials via a thermal-migration strategy using tungsten single atoms as the parent material.[8] The W-SAs anchored on the P-doped carbon material were obtained by pyrolyzing the W precursors at 700 °C for 2 h under an Ar atmosphere, followed by the alkaline leaching in a 6 M KOH solution for 3 days. The W-ACs were obtained using W-SAs as the parent material via thermal migration strategy at 550 °C, respectively, under a mixture of Ar/H_2 (1 bar) atmosphere. The formation of the intermediate W-ACs (primarily W-W dimers) can be dynamically monitored by probing the evolution of the electronic structures of W atoms from W-SAs to WC NPs using in-situ variable-temperature NAP-XPS measurements. Xia, et al. reported the design and synthesis of an Al-Al bonded dual atomic catalyst stabilized within an amorphous nitrogen-doped porous carbon matrix (Al_2NC) by a hydroxylamine-assisted carbonization method.[9] The NH_2OH can coordinate with two Al^{+3} cations simultaneously using its N and O sites, which keeps the cations nearby while uniformly separated by the glucose backbone. This configuration for the formation of dual atomic Al-Al sites could be

retained during subsequent carbonization at 700 °C in the final step. The decomposition temperature of both NH_2OH and glucose is in the same temperature range (130-150 °C). The generated NH_3 and HNO during the decomposition of NH_2OH react with glucose to form a porous three-dimensional nitrogen-doped carbon matrix (NC). Simultaneously, the formed pseudo bimetallic complex is transformed into neighboring Al-Al atomic pairs embedded within the NC matrix. Thus, uniformly dispersed nitrogen-coordinated dual atomic Al_2-N_x-C_y sites within the NC matrix can be formed. In addition, the concurrent pyrolysis of various metal precursors using a thermal migration approach can also create catalysts with hetero-diatomic sites.[10-12] For example, Pan, et al. precisely fabricated the Fe–Ni dual sites in N, P-co-doped C through a simple in situ adsorption-pyrolysis method.[13]

References:

[1] Leng, K. et al. Interfacial cladding engineering suppresses atomic thermal migration to fabricate well-defined dual-atom electrocatalysts. *Adv. Funct. Mater*. **32**, 2205637 (2022).

[2] Wang, X. et al. Edge-rich Fe-N_4 active sites in defective carbon for oxygen reduction catalysis, *Adv. Mater*. **32**, 2000966 (2020).

[3] Yang, C.-L. et al. Sulfur-anchoring synthesis of platinum intermetallic nanoparticle catalysts for fuel cells. *Science* **374**, 459-464 (2021).

[4] Kim, K. et al. Geometric tuning of single-atom FeN_4 sites via edge-generation enhances multi-enzymatic properties. *Adv. Mater*. **35**, 2207666 (2023).

[5] Hou, Y. et al. Atomically dispersed nickel-nitrogen-sulfur species anchored on

porous carbon nanosheets for efficient water oxidation. *Nat. Commun*. **10**, 1392 (2019).

[6] Zhang, N. et al. High-density planar-like Fe_2N_6 structure catalyzes efficient oxygen reduction, *Matter* **3**, 509-521 (2020).

[7] Ovidiu Cretu. et al. Migration and localization of metal atoms on strained graphene, *PRL* **105**, 196102 (2010).

[8] Chen, Z. et al. Thermal migration towards constructing W-W dual-sites for boosted alkaline hydrogen evolution reaction, *Nat. Commun*. **13**, 763 (2022).

[9] Sudip Biswas et al. Synergistic Al-Al dual-atomic site for efficient artificial nitrogen fixation, *Angew. Chem. Int. Ed*. **63**, e202405493 (2024).

[10] Zeng, Z. et al. Orbital coupling of hetero-diatomic nickel-iron site for bifunctional electrocatalysis of CO_2 reduction and oxygen evolution, *Nat. Commun*. **12**, 4088 (2021).

[11] Chen Y. et al. Coordination shell dependent activity of CuCo diatomic catalysts for oxygen reduction, oxygen evolution, and hydrogen evolution reaction, *Adv. Funct. Mater*. **34**, 2311664 (2024).

[12] Chen C. et al. Adjacent Fe site boosts electrocatalytic oxygen evolution at Co site in single-atom-catalyst through a dual-metal-site design, *Energy Environ. Sci*. **16**, 1685-1696 (2023).

[13] Pan, F. et al. Theory-guided design of atomic Fe-Ni dual sites in N, P-co-doped C for boosting oxygen evolution reaction, *Chem Catalysis* **1**, 734-745 (2021).

Our revision: We have revised our manuscript according to the reviewer's suggestion (**Line 116-124** in the revised manuscript).

8. *In Figure 1a bottom part after annealing S sites are within the graphene network and not available for coordination. While in the final structure, these sites are coordinated to metal centers. Any explanation?*

Response: Thank you for your professional comment. When sulfur is doped in carbon support can induce diverse strong metal-support interaction (SMSI). In particular, the strong interfacial metal-sulfur bonding could greatly enhance the adhesion strength between metal and the sulfur-doped carbon (S-C) support, leading to outstanding sintering resistance at high temperatures up to 1100 °C. The unique SMSI and anti-sintering properties make the S-C support capable of generating diverse highly dispersed catalysts, ranging from monometallic single-atom/cluster catalysts to bimetallic cluster and intermetallic compounds catalysts with application potentials for a variety of industrially relevant reactions.[1] The S-C support exhibits favorable conductivity due to the incorporation of doped sulfur atoms, which are chemically integrated into the carbon lattice structure. In certain instances, these doped sulfur atoms may be removed from the S-C supports, resulting in the cleavage of S-C bonds and subsequent diffusion, thereby creating edge-rich sulfur sites.[2] Notably, during the high-temperature carbonization process conducted in an inert gas atmosphere, volatile sulfur species (with a boiling point of 444 °C) preferentially interact with the carbon framework, leading to the disruption of C-S bonds and the formation of edge-rich sulfur defect.[3,4] Subsequently, the metallic species that experience thermal migration at elevated temperatures will effectively diffuse into edge-rich S and N defects, thereby facilitating the formation of a well-coordinated isolated metal atom.[5] In our work, the

porous S-doped carbon supports (SNC) were prepared by limited domain encapsulation pyrolysis. In this matrix, sulfur was predominantly incorporated in the form of C-S-C. The presence of numerous sulfur-containing sites, coupled with the highly porous structure of the S-C, facilitated the preparation of diatomic iron catalysts with a high loading of 6.72 wt%. During the high-temperature pyrolysis process, the S-C bond adjacent to the N atom undergoes cleavage, resulting in the formation of sulfur sites at the edges that subsequently capture iron atoms and establish Fe-S bonds.

Numerous prior studies have employed analogous sulfur capture methodologies to synthesize atomic-level catalysts characterized by metal-sulfur coordination. For example, Li et al. initially synthesized a hydrogel utilizing carrageenan as a sulfur source, taking advantage of the randomly coiled structure of the carrageenan macromolecular chains.[6] Following a pyrolysis process conducted at temperatures ranging from 800 to 1100 °C, the sulfur sites within the carrageenan macromolecular chains effectively capture iron atoms, resulting in the formation of a Fe_{SA}-NSC catalyst, which is represented by the FeN_3S_1 model. Guo et al. provide an exemplary method for establishing atomic cluster catalysts with engineered S-dominated coordination in the hollowed carbon matrix.[7] The Fe^{3+}/ZIF-8 with a polyhedral structure was first prepared. Subsequently, the PZS layer (rich with triple elements of N, P, and S) was wrapped around the surface of Fe^{3+}/ZIF-8 through aggregation. During pyrolysis, the C-S-C bond in PZS is broken, and the generated S sites preferentially coordinate with the Fe atom diffused from the inner layer to form the Fe_3-S_5N_1 structure. Zhou et al. reported the main-group single atoms (Pb SA/OSC) in situ anchored onto carbon supports

employing a carbon dot-assisted pyrolysis approach.[8] Specifically, the S, O-functionalized carbon dots (SCDs) were first prepared by utilizing varying ratios of S/O-containing precursors. The interfacial metal-sulfur bonding between the Pb cations and SCDs effectively anchored and stabilized the main-group sites, proffering an atomically dispersed metal precursor. Then, the main-group Pb SACs with a distinctive S and O dual coordination were obtained via pyrolysis treatment under a protective flowing Ar atmosphere. Zhao et al. developed an atomic-interfacial-regulation approach to fabricate dual single Fe/Co atoms synchronized with both nitrogen/sulfur atoms on defective/graphitic/porous carbon nanosheets (Fe, Co/DSA-NSC). The N, S co-doped C nanosheet (NSC) was first prepared by in-situ template synthesis. Subsequently, NSC nanosheets were allowed to adsorb metal cations, which were then calcined at high temperatures in an inert atmosphere to form the Fe-S and Co-S bonds [Fe-(N_2S)/Co-(N_2S) moiety].[9] Zhao et al. reported an atomically dispersed N, S co-doped carbon with abundant vacancy defects (NSC-vd) anchored Fe single atoms (SAs). The coal pitch (CP) supramolecule is rich in natural S and N heteroatoms, which act as anchor sites for stabilizing single-atom Fe sites. During the pyrolysis process of CP, a transformation occurs from soft carbon to graphitization, forming an S, N co-doped graphite carbide layer. Then, S and N atoms in graphite carbon capture Fe atoms to form Fe-N_3S_1 coordinated single-atom catalysts.[10] Therefore, using the sulfur capture strategy to synthesize single-atom catalysts under high-temperature conditions is feasible and universal.

References:

[1] Yin, P. et al. Strong metal-support interactions through sulfur-anchoring of metal catalysts on carbon supports, *Angew. Chem. Int. Ed*. **135**, e202302819 (2023).

[2] Wang, L. et al. A sulfur-tethering synthesis strategy toward high-loading atomically dispersed noble metal catalysts, *Sci. Adv.* **5**, eaax6322 (2019).

[3] Zhou, H. et al. Cation-exchange induced precise regulation of single copper site triggers room-temperature oxidation of benzene, *J. Am. Chem. Soc.* **142**, 29, 12643-12650 (2020).

[4] Zhang, E. et al. Engineering the local atomic environments of indium single atom catalysts for efficient electrochemical production of hydrogen peroxide, *Angew. Chem., Int. Ed.* **134**, e202117347 (2022).

[5] Chen, Y. et al. Coordination shell dependent activity of CuCo diatomic catalysts for oxygen reduction, oxygen evolution, and hydrogen evolution reaction, *Adv. Funct. Mater*. **34**, 2311664 (2024).

[6] Li, Y. et al. Local spin-state tuning of iron single-atom electrocatalyst by S-coordinated doping for kinetics-boosted ammonia synthesis, *Adv. Mater*. **34**, 2202240 (2022).

[7] Guo, X. et al. Modulating coordination of iron atom clusters on N, P, S triply doped hollow carbon support towards enhanced electrocatalytic oxygen reduction, *Angew. Chem.* ***135***, e202314124 (2023).

[8] Zhou, X. et al. Constructing sulfur and oxygen supercoordinated main-group electrocatalysts for selective and cumulative H_2O_2 production, *Nat. Commun.* **15**, 193 (2024).

[9] Ghulam Yasin et al. Simultaneously engineering the synergistic-effects and coordination-environment of dual-single-atomic iron/cobalt-sites as a bifunctional oxygen electrocatalyst for rechargeable zinc-air batteries, *ACS Catal*. **13**, 2313-2325 (2023).

[10] Zhao, Y. et al. Vacancy defects inductive effect of asymmetrically coordinated single-atom Fe-N_3S_1 active sites for robust electrocatalytic oxygen reduction with high turnover frequency and mass activity, *Adv. Mater*. **36**, 2308243 (2024).

Our revision: We have revised our manuscript according to the reviewer's suggestion (**Line 116-124** in the revised manuscript).

9. *Figure 2, please enlarge the small area of Figure d to show Fe sites. I can see numerous sites that are randomly distributed. Fe K-edge in EELS spectra should be presented as inset. Do the authors observe any peak splitting? Similarly, XANES should have an inset showing an enlarged view of the high-energy region.*

Response: We sincerely appreciate this critical suggestion from the reviewer. According to your suggestion, the corresponding magnified HAADF-STEM images clearly evidence that a large proportion of the bright spots are adjacent to each other and present a Fe-Fe diatomic structure, as indicated by the red dashed circles in the D region inset of **Fig. R22**. We enlarged the Fe L-edge in EELS spectra and did not observe any peak splitting in **Fig. R23**.

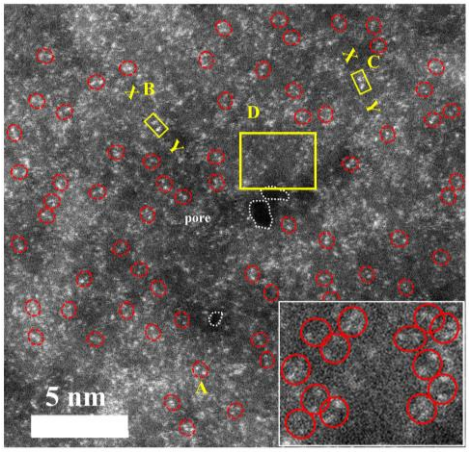

Fig. R22. Aberration-corrected HAADF-STEM of the *A*-$Fe_2S_1N_5$/SNC. The inset shows a locally amplified structure of the D region, with scale bars of 1 nm.

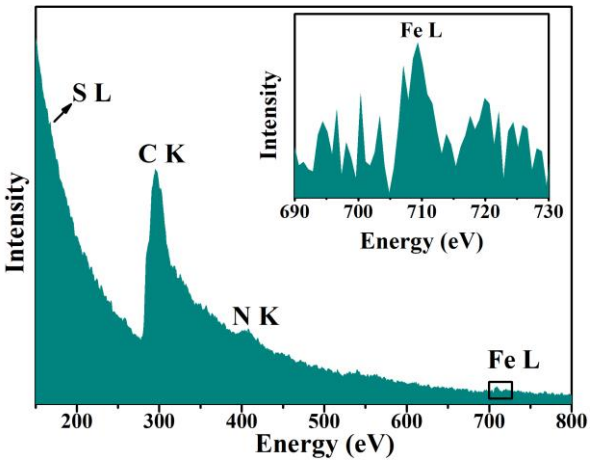

Fig. R23. Electron energy loss spectroscopy (EELS) of *A*-$Fe_2S_1N_5$/SNC. Inset: STEM-EELS point spectrum of Fe site.

The local electronic structure and the coordination environment of the catalysts are correlated with their catalytic performance, which can be detected by synchrotron-radiated XAFS. Synchrotron-radiated XAFS measurement can be divided into both extended X-ray absorption fine structure (EXAFS) and X-ray absorption near edge structure (XANES).[1,2] The EXAFSs are usually used to detect the local structure environment of the probed atom including the coordination type, coordination number, coordination distance, and disorder of the surrounding coordination atoms.[3,4] Different

from EXAFS, the XANES signal is caused by the multiple scattering of the exciting photoelectrons arising from the probed atom, which can give the oxidation states and coordination chemistries of the probed atom.[5,6] For XANES, it can be divided into the regions of pre-edge, edge, and post-edge. The pre-edge reflects the information of system symmetry and orbital hybridization, which originate from the inner electron transition to the empty bound states. The absorption edge of XANES spectra reflects the oxidation state of the probed atom, which defines the ionization threshold.[7] The absorption edge of the probed atom shifts to higher energy with the increase of the oxidation state. The post-edge reflects the spatial structure of the neighbor atom, which originates from the multiple-scattering resonances of the photoelectrons. Therefore, the XANES spectra are usually used to analyze the oxidation state and the characteristic peak of the probed atom.

Furthermore, the Fe K-edge XANES spectra for *A*-$Fe_2S_1N_5$/SNC, along with a corresponding magnified view of the absorption edge and the high-energy region, are presented in **Fig. R24**. As illustrated in **Fig. R24a** and **24b**, the position of the adsorption threshold for *A*-$Fe_2S_1N_5$/SNC is situated between that of FeS_2 and Fe_2O_3, which indicates the average metal valence states of Fe species in *A*-$Fe_2S_1N_5$/SNC were situated between them. In the high-energy region of the XANES spectra, direct information is not readily obtainable. Consequently, we have included an enlarged view of the absorption edge region in the Fe K-edge XANES spectra of *A*-$Fe_2S_1N_5$/SNC in the revised manuscript.

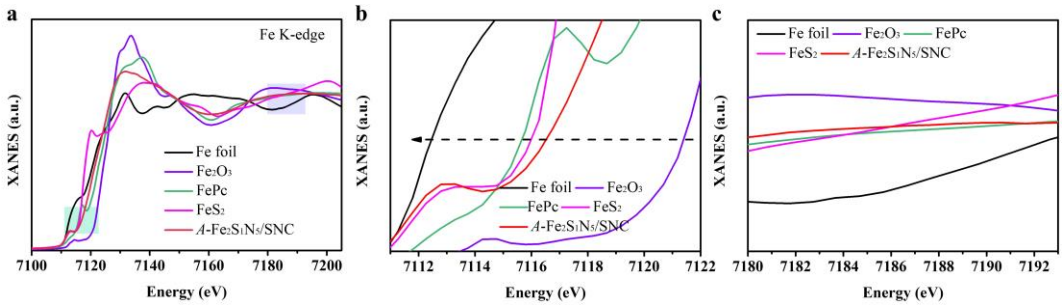

Fig. R24. (a) The Fe K-edge XANES spectra of *A*-$Fe_2S_1N_5$/SNC and the references. (b) The enlarged view of the absorption edge region. (c) The magnified of the high-energy region.

References:

[1] Chen, W. et al. Single tungsten atoms supported on MOF-derived N-doped carbon for robust electrochemical hydrogen evolution. *Adv. Mater.* **30**, 1800396 (2018).

[2] Li, X. et al. In situ/operando techniques for characterization of single-atom catalysts. *ACS Catal.* **9**, 2521-2531 (2019).

[3] Chen, S. et al. Supported metal clusters: synthesis, structure, and catalysis. *Chem. Rev.* **95**, 511-522 (1995).

[4] Abbas Beheshti Askari, et al. High-resolution X-ray emission and X-ray absorption spectroscopy. *Chem. Rev.* **101**, 1779-1808 (2001).

[5] Zhuang, Z. et al. Single-atom catalysis enables long-life, high-energy lithium-sulfur batteries. *Nano Res.* **13**, 1856-1866 (2020).

[6] Xiao, M. et al. Microporous framework induced synthesis of single-atom dispersed Fe-N-C acidic ORR catalyst and its in situ reduced Fe-N_4 active site identification revealed by X-ray absorption spectroscopy. *ACS Catal.* **8**, 2824-2832 (2018).

[7] Yoann Pertot et al. Time-resolved X-ray absorption spectroscopy with a water

window high-harmonic source. *Science* **355**, 264-267 (2017).

Our revision: We have revised our manuscript according to the reviewer's suggestion (**Fig. 2d, Fig. 2f**, and **Fig. 2g** in the revised manuscript).

10. The peak assigned to Fe-S scattering in EXAFS spectra of A-$Fe_2S_1N_5$/SNC might be from the Fe-C scattering path. Such scattering has been observed in high-density Fe-N-C catalysts (Nat. Catal. 2022, 5, 311–323)

Response: Thank you for your careful comment. The EXAFS spectra revealed significant differences in the local coordination of Fe across the various catalysts, as illustrated in **Fig. R25**. The EXAFS curves of the *A*-$Fe_2S_1N_5$/SNC catalyst exhibited a prominent peak at approximately 1.5 Å, which corresponds to the Fe-N scattering. Notably, a shoulder peak at a distance of R ≈ 1.9 Å was found in the EXAFS spectra of *A*-$Fe_2S_1N_5$/SNC. In contrast to the EXAFS spectra of FeS_2, this signal was attributed to Fe-S scattering, indicating the formation of a Fe-S bond.

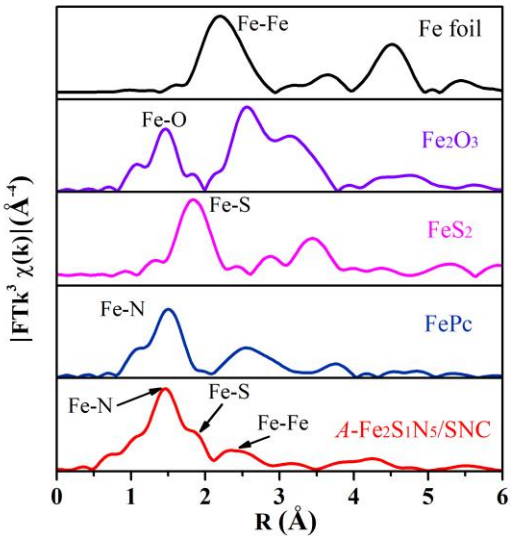

Fig. R25. Fourier transforms of extended X-ray absorption fine structure (EXAFS) spectra of the Fe K-edge.

Table R9. Structural parameters extracted from the Fe K-edge EXAFS fitting. (S_0^2=0.87)

sample	Scattering pair	CN	R(Å)	σ^2 (10^{-3}Å^2)	ΔE_0 (eV)	R factor
A-$Fe_2S_1N_5$/SNC	Fe-N	2.5	1.90	4.1	2.0	0.006
	Fe-S	0.5	2.30	4.6		
	Fe-Fe	1.0	2.56	6.9		

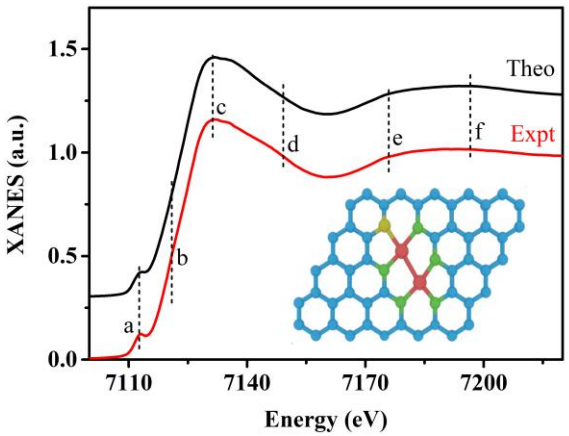

Fig. R26. Comparison between the experimental Fe K-edge XANES spectrum of *A*-$Fe_2S_1N_5$/SNC and the theoretical spectra calculated with the depicted structures.

To obtain quantitative information regarding the coordination configuration, including coordination numbers and bond lengths, the EXAFS fitting analysis of *A*-$Fe_2S_1N_5$/SNC was performed (**Table R9**). In the case of *A*-$Fe_2S_1N_5$/SNC, the average number of coordination for Fe-S bonds was determined to be 0.5. Within *A*-$Fe_2S_1N_5$/SNC, the Fe_2 species are coordinated with five N with a distance of 1.90 Å and the Fe_1 species are coordinated with one S with a distance of 2.30 Å. The *A*-$Fe_2S_1N_5$/SNC model was derived from the simulated Fe K-edge XANES spectra (**Fig.**

R26), which correspond with the experimental spectra. This alignment provides evidence for the absence of Fe-C scattering. Therefore, the coordination number of Fe-S in *A*-$Fe_2S_1N_5$/SNC was determined to be 0.5, with average bond lengths of 2.30 Å, consistent with the results reported in previous literatures.[1-3]

For example, Yasin et al. established the unsymmetrically organized N and S coordinated Fe/Co bridged atomic sites [Fe-(N_2S)/Co-(N_2S) moiety]. In the EXAFS spectra of the Fe,Co/DSA-NSC, the peak located at ~1.71 Å can be allocated to the Fe-S coordination pathway, and the average bond length of Fe-S is 2.21±0.03 Å.[4] Chen et al. developed an unusual ZnCoFe hetero-trimetallic atom site with the nitrogen-coordinated Co and Zn atoms adjacent to the sulfur/nitrogen dual-coordinated Fe atoms ($ZnN_3CoN_3FeN_2S$) anchored in sulfur/nitrogen-doped carbon. The Fe K-edge FT-EXAFS spectra of ZnCoFe-TAC/SNC show that the peak located at 1.8 Å is attributed to the Fe-S coordination in the structures, and the average bond length of Fe-S is 2.35 Å.[5] Liu et al. designed an innovative theoretical model of Fe-N_4SP with Fe-N_4 sites with axial sulfur atoms in the first coordination shell and adjacent phosphorus atoms in the second coordination shell. The Fe-S peak can be detected in Fe-N_4SP/NPS-HC via the quantitative least-squares curve-fitting, with coordination numbers of Fe-S calculated as 1.1, and the average bond length of Fe-S is 2.24±0.01 Å.[6] Zhao et al. reported an atomically dispersed N, S co-doped carbon with abundant vacancy defects (NSC-vd) anchored Fe single atoms (SAs). The EXAFS fitting result showed that the coordination number (CN) of the Fe-S shell in Fe SAs/NSC-vd is 1.0, and the average bond length of Fe-S is 2.25±0.04 Å.[7] In summary, the peak located at a distance of R ≈ 1.9 Å and

the average bond length ≈ 2.30 Å can be allocated to the Fe-S scattering path.

The Fe-C scattering path has been identified in high-density Fe-N-C catalysts, as reported in the literature (*Nat. Catal. 2022, 5, 311–323*). The peak observed at around 2.7 Å can be attributed to the Fe-C coordination path within the EXAFS spectra of the Fe-N_4 single-atom catalysts (SACs). The average bond lengths of Fe-C_1 and Fe-C_2 are 3.10±0.02 and 3.47±0.02 Å, respectively. Furthermore, comparable Fe-C scattering paths have also been reported in other single-atom catalysts. For instance, Noh et al. reported edge-hosted single-atom catalytic sites of M-N (M = Fe, Co, Ni, Cu) on carbon supports.[8] For the prepared Fe-N/S-CNT-GR catalyst, fit parameters obtained from the analysis of the Fe K edge EXAFS spectra show that the average bond length of Fe-C is 3.01±0.01 Å. Meng et al. have developed a NiFe-N-C catalyst that incorporates iron nanoclusters through the pyrolysis of metal phthalocyanine and nitrogen-doped carbon precursors.[9] The EXAFS spectrum of the Fe K-edge in the NiFe-N-C catalyst reveals a peak at approximately 2.45 Å, which is attributed to the Fe-C scattering path. Furthermore, the average bond length for the Fe-C interaction is recorded as 3.00 Å. In a separate study, Li et al. synthesized single-iron-atom catalysts utilizing a solvent-assisted linker exchange method.[10] In the Fe K-edge EXAFS spectrum, the relative peak intensity observed for the synthesized Fe-NC and Fe-NC-S at a distance of 2.64 Å can be ascribed to the Fe-C scattering path. Furthermore, the average bond length for the Fe-C interaction is measured to be 3.00 Å. Zhuang et al. report a surfactant-free strategy to use amorphous metal oxide nanosheets (M-ONS) as sacrificial templates to form the MOF-74 nanosheets (FeCo-MNS-1.0) by confined ligand coordination.[11] Analysis of

the EXAFS spectra in the R-space for Fe K-edge reveals that the relative peak intensity at 2.64 Å is associated with the Fe-C scattering path in the synthesized FeCo-MNS-1.0 catalyst, with average bond lengths of 2.997 Å. Therefore, EXAFS spectroscopy can distinguish between the Fe-S scattering path and the Fe-C scattering path. Consequently, the Fe-S scattering path exists in the *A*-$Fe_2S_1N_5$/SNC catalyst rather than the Fe-C scattering path.

References:

[1] Qiao, Y. et al. Sulfuration of an Fe-N-C catalyst containing Fe_xC/Fe species to enhance the catalysis of oxygen reduction in acidic media and for use in flexible Zn-air batteries, *Adv. Mater*. **30**, 1804504 (2018).

[2] Shang, H. et al. Engineering unsymmetrically coordinated Cu-S_1N_3 single atom sites with enhanced oxygen reduction activity, *Nat. Commun*. **11**, 3049 (2020).

[3] Li, Y. et al. Local Spin-state tuning of iron single-atom electrocatalyst by S-coordinated doping for kinetics-boosted ammonia synthesis, *Adv. Mater.* **34**, 2202240 (2022).

[4] Ghulam Yasin. et al. Simultaneously engineering the synergistic-effects and coordination-environment of dual-single-atomic iron/cobalt-sites as a bifunctional oxygen electrocatalyst for rechargeable zinc-air batteries, *ACS Catal*. **13**, 2313-2325 (2023).

[5] Chen, C. et al. An asymmetrically coordinated ZnCoFe hetero-trimetallic atom catalyst enhances the electrocatalytic oxygen reaction, *Energy Environ. Sci.* **17**, 2298-2308 (2024).

[6] Liu, J. et al. High-coordination Fe-N_4SP single-atom catalysts via the multi-shell synergistic effect for the enhanced oxygen reduction reaction of rechargeable Zn-air battery cathodes, *Energy Environ. Sci.* **17**, 249-259 (2024).

[7] Zhao, Y. et al. Vacancy defects inductive effect of asymmetrically coordinated single-atom Fe-N_3S_1 active sites for robust electrocatalytic oxygen reduction with high turnover frequency and mass activity, *Adv. Mater*. **36**, 2308243 (2024).

[8] Noh, W. Y. et al. Molecularly engineered carbon platform to anchor edge-hosted single-atomic M–N/C (M = Fe, Co, Ni, Cu) electrocatalysts of outstanding durability. *ACS Catalysis* **12**, 7994-8006 (2022).

[9] Meng, H. et al. Optimizing electronic synergy of atomically dispersed dual-metal Ni-N_4 and Fe-N_4 sites with adjacent Fe nanoclusters for high efficiency oxygen electrocatalysis, *Energy Environ. Sci.* **17**, 704-716 (2024).

[10] Li, X. et al. Identification of the electronic and structural dynamics of catalytic centers in single-Fe atom material, *Chem* **6**, 3440-3454 (2020).

[11] Zhuang, L et al. A surfactant-free and scalable general strategy for synthesizing ultrathin two-dimensional metal-organic framework nanosheets for the oxygen evolution reaction, *Angew. Chem. Int. Ed*. **58**, 13565-13572 (2019).

11. Though the OER performance of A-$Fe_2S_1N_5$/SNC was compared with Fe_1N_4/NC and Fe_2N_6/NC catalysts. This does not verify that Fe_1-N_3S-C sites will be less active toward OER. A fair comparison with such catalysts is required both experimentally and in DFT.

Response: We highly appreciate the reviewer for the helpful comment. To the recommendations provided by the reviewer, the $Fe_1S_1N_3$/NC catalyst was synthesized.

A thorough assessment of its efficacy in the OER and ORR was performed, accompanied by DFT calculations. This analysis was undertaken to facilitate a comparative assessment of the $Fe_1S_1N_3$/NC catalysts against the *A*-$Fe_2S_1N_5$/SNC, Fe_1N_4/NC, and Fe_2N_6/NC catalysts. The experimental procedure is delineated as follows: the synthesized NC nanosheet support was subjected to ultrasonic dispersion in 10 mL of ethanol. Subsequently, 40 mg of iron (III) chloride, 0.5 mL of thiophene, 1.0 g of dicyandiamide, and 0.1 g of trimesic acid were incorporated into the suspension, which was then stirred vigorously for 30 minutes. The solvent was subsequently removed through evaporation using a rotary evaporator, yielding a grey powder. This grey powder was then subjected to annealing at a temperature of 900 °C, with a heating rate of 2 °C min^{-1}, and maintained at this temperature for 3 hours in an atmosphere of high-purity nitrogen. Following natural cooling to ambient temperature, the resultant black $Fe_1S_1N_3$/NC was obtained. Thereafter, the electrochemical performance of the $Fe_1S_1N_3$/NC in terms of OER and ORR was evaluated under conditions consistent with those of the control samples.

(1) The TEM images of $Fe_1S_1N_3$/NC, presented in **Fig. R27a** and **R27b**, reveal that the two-dimensional (2D) nanosheets possess an ultrathin thickness of approximately 10 nm, with lateral dimensions extending to several micrometers. Furthermore, high-resolution TEM analysis did not reveal the presence of any metallic particles or clusters. Aberration-corrected HAADF-STEM reveals many bright dots are uniformly distributed across the graphene framework, indicating that the Fe species are atomically dispersed. Elemental mapping further demonstrates that C, N, S, and Fe are

homogeneously distributed throughout the entire support.

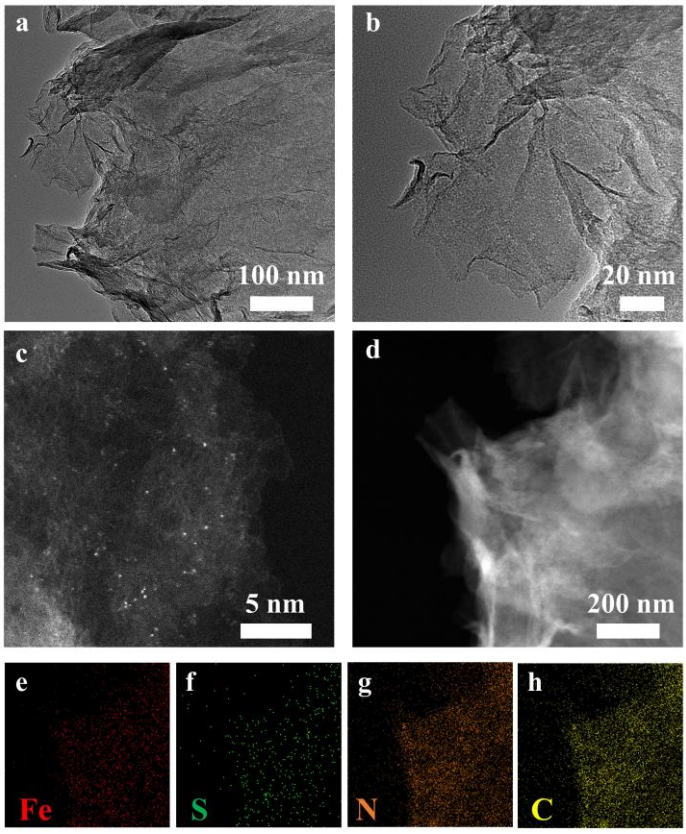

Fig. R27. TEM images of $Fe_1S_1N_3$/NC at (a) 100 nm and (b) 20 nm scale bar showing the two-dimensional wrinkle sheet-like structure. (c) Aberration-corrected HAADF-STEM image. (d) HAADF-STEM image. (e-h) Corresponding EDS mapping images of $Fe_1S_1N_3$/NC showing the Fe, S, N, and C elements are uniformly distributed throughout the entire $Fe_1S_1N_3$/NC.

Additionally, wide-angle X-ray diffraction analysis identifies the distinct peak associated with graphitic carbon at 25° (**Fig. R28**), while no diffraction peaks corresponding to metallic iron or its oxides (or carbides) are observed, thereby corroborating the atomic dispersion of the Fe species. To investigate the detailed elemental composition and valence states of the $Fe_1S_1N_3$/NC catalyst, we performed X-ray photoelectron spectroscopy (XPS) (**Fig. R29**). The analysis uncovered that the

sample primarily consisted of N, C, Fe, and S elements. The high-resolution S 2p of the $Fe_1S_1N_3$/NC sample affirmed the presence of S $2p_{3/2}$, S $2p_{1/2}$, and SO_x species (**Fig. R29b**). Furthermore, the C 1s spectra displayed three distinct peaks corresponding to C–C/C=C, C–N/O, and O=C–C (**Fig. R29c**). A detailed examination of the high-resolution N 1s spectrum allowed for the identification of three unique nitrogen species (**Fig. R29d**), which were identified as graphitic nitrogen, pyrrolic nitrogen, and pyridinic nitrogen.

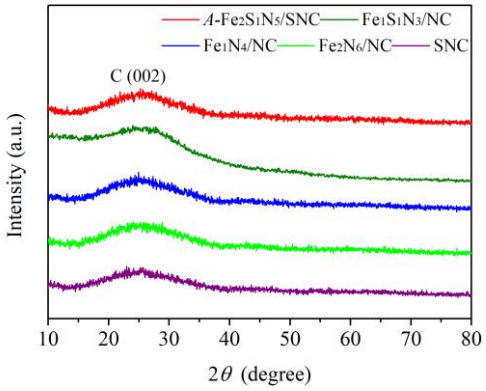

Fig. R28. XRD patterns of *A*-$Fe_2S_1N_5$/SNC, $Fe_1S_1N_3$/NC, Fe_1N_4/NC, Fe_2N_6/NC, and SNC. The broad peaks at 20-30° are assigned to the (002) plane of graphite.

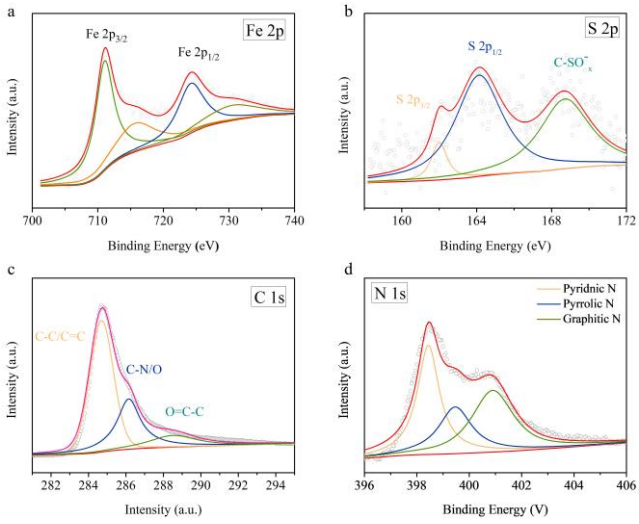

Fig. R29. XPS spectrum of $Fe_1S_1N_3$/NC. (a) Fe 2p, (b) S 2p, (c) C 1s, and (d) N 1s.

The Fe K-edge XANES spectra for the $Fe_1S_1N_3$/NC catalyst are presented in **Fig.**

R30a. The position of the absorption threshold for $Fe_1S_1N_3$/NC was determined to be situated between that of FeS_2 and Fe_2O_3, indicating that the oxidation state of iron is likely between them. Additionally, the EXAFS spectra revealed significant differences in the local coordination of iron across the various catalysts, as shown in **Fig. R30b**. The EXAFS curves for the $Fe_1S_1N_3$/NC catalyst exhibited a prominent peak at approximately 1.5 Å, which corresponds to the scattering path related to the first shell Fe–N interactions. Furthermore, a shoulder peak at around 1.9 Å was observed in the EXAFS spectra of $Fe_1S_1N_3$/NC. In contrast to the EXAFS spectra of FeS_2, this signal was attributed to Fe-S scattering.

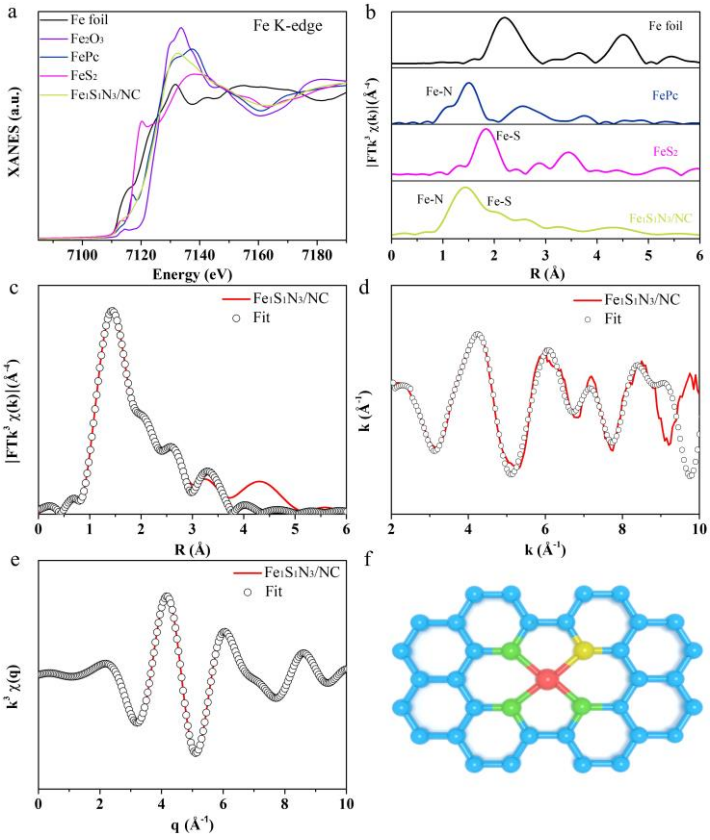

Fig. R30. XANES spectra of the $Fe_1S_1N_3$/NC catalyst. (a) The Fe K-edge. (b) Fourier transforms of extended X-ray absorption fine structure (EXAFS) spectra of the Fe K-edge. EXAFS fitting curves of $Fe_1S_1N_3$/NC. (c) The FT-EXAFS fitting curve of Fe foil

at Fe K-edge, (d) k space fitting curve, and (e) q space fitting curve. (f) Atomic interface structure model of $Fe_1S_1N_3$/NC.

Significantly, there was a lack of substantial evidence indicating the presence of conventional Fe-Fe bonding in $Fe_1S_1N_3$/NC, suggesting that the iron atoms were present in an isolated state. The quantitative EXAFS fitting is studied to authenticate the local coordination configuration of Fe in $Fe_1S_1N_3$/NC catalyst (**Fig. R30c-30e**). The fitting results revealed the coordination configuration in $Fe_1S_1N_3$/NC was $Fe_1S_1N_3$ moiety. The first shell of $Fe_1S_1N_3$/NC was fitted with the Fe-N and Fe-S back-scattering path. **Fig. R30f** shows the atomic interface structure model of $Fe_1S_1N_3$/NC.

(2) To investigate the effect of S heteroatoms on the OER performance, the electrochemical performance of the $Fe_1S_1N_3$/NC catalyst was evaluated via a three-electrode system. The LSV polarization curve presented in **Fig. R31a** demonstrates that *A*-$Fe_2S_1N_5$/SNC exhibits superior catalytic activity, with a value of 193 mV for η_{10}, in comparison to $Fe_1S_1N_3$/NC (263 mV@η_{10}), Fe_2N_6/NC (281 mV@η_{10}), and Fe_1N_4/NC (369 mV@η_{10}). This suggests that the incorporation of diatomic Fe and sulfur doping enhances the local coordination environment of the rigid Fe-N_4 framework. The Tafel slopes for *A*-$Fe_2S_1N_5$/SNC, $Fe_1S_1N_3$/NC, Fe_2N_6/NC, and Fe_1N_4/NC catalysts are 61, 78, 86, and 95 mV dec^{-1}, respectively, revealing that *A*-$Fe_2S_1N_5$/SNC has the fastest catalytic kinetics (**Fig. R31b**). The charge-transfer resistance of the catalyst was assessed using electrochemical impedance spectroscopy (EIS). The *A*-$Fe_2S_1N_5$/SNC catalyst demonstrated the lowest charge-transfer resistance, indicating an enhanced electron transfer rate at the active center due to the establishment of a novel

coordination environment (**Fig. R31c**). To further elucidate its intrinsic activity, the electrochemical active surface area (ECSA) of the catalyst was determined through the measurement of double-layer capacitance (C_{dl}), as illustrated in **Fig. R31d**. The C_{dl} value for *A*-$Fe_2S_1N_5$/SNC (3.2 mF cm^{-2}) surpasses those of $Fe_1S_1N_3$/NC (2.5 mF cm^{-2}), Fe_2N_6/NC (2.1 mF cm^{-2}), and Fe_1N_4/NC (1.2 mF cm^{-2}). This suggests that the newly formed coordination environment in *A*-$Fe_2S_1N_5$/SNC facilitates greater exposure of the active sites.

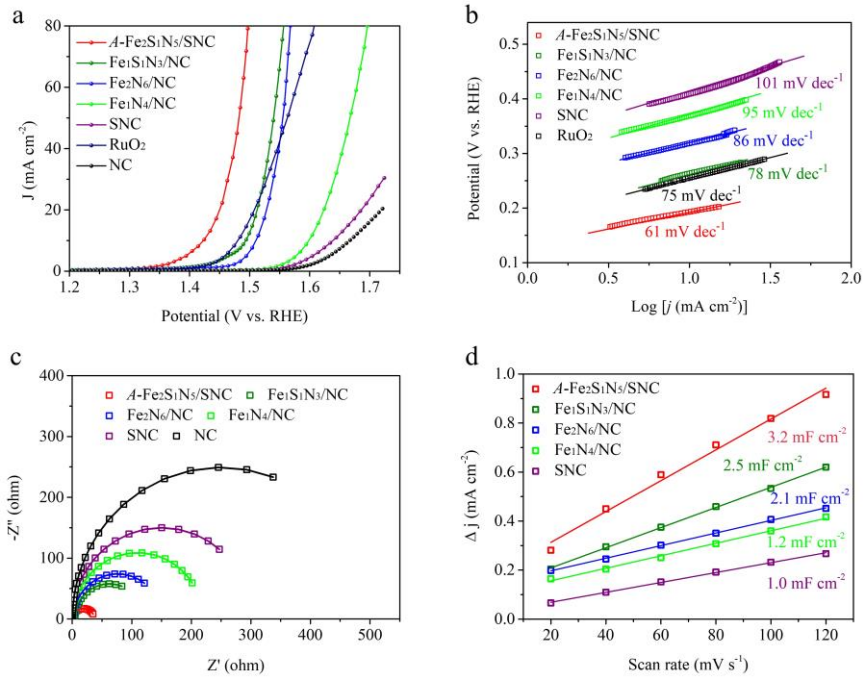

Fig. R31. OER electrochemical activity in 1.0 M KOH. (a) LSV curves, (b) Tafel slopes, (c) EIS curves, and (d) calculated C_{dl} values of *A*-$Fe_2S_1N_5$/SNC, $Fe_1S_1N_3$/NC, Fe_2N_6/NC, Fe_1N_4/NC, and SNC catalysts.

(3) As illustrated in **Fig. R32a**, the *A*-$Fe_2S_1N_5$/SNC catalyst demonstrated enhanced ORR activity, characterized by a high onset potential (E_{onset}) of 1.05 V, which is comparable to that of Pt/C at 0.99 V. In contrast, the catalysts $Fe_1S_1N_3$/NC, Fe_2N_6/NC, Fe_1N_4/NC, and SNC exhibited inferior electrocatalytic performance, with E_{onset} values

of 0.98, 0.97, 0.95, and 0.83 V, respectively. The linear sweep voltammetry (LSV) curves for these catalysts further confirmed that *A*-$Fe_2S_1N_5$/SNC exhibited the most favorable activity, as indicated by its highest half-wave potential ($E_{1/2}$). Specifically, $E_{1/2}$ of *A*-$Fe_2S_1N_5$/SNC, $Fe_1S_1N_3$/NC, Fe_2N_6/NC, Fe_1N_4/NC, SNC, and Pt/C was 0.91, 0.85, 0.82, 0.79, 0.70, and 0.85 V *vs.* RHE, respectively. The lowest Tafel slope of *A*-$Fe_2S_1N_5$/SNC (87 mV dec^{-1}) among those of $Fe_1S_1N_3$/NC (89 mV dec^{-1}), Fe_2N_6/NC (91 mV dec^{-1}), Fe_1N_4/NC (109 mV dec^{-1}), SNC (110 mV dec^{-1}), and Pt/C (101 mV dec^{-1}) also supported the superior ORR kinetics of *A*-$Fe_2S_1N_5$/SNC (**Fig. R32b**). Moreover, *A*-$Fe_2S_1N_5$/SNC exhibited a remarkable kinetic current density (J_k) of 12.6 mA cm^{-2} at 0.85 V *vs.* RHE, about 4 times and 7 times higher than that of Fe_2N_6/NC (3.5 mA cm^{-2}) and Fe_1N_4/NC (1.8 mA cm^{-2}), respectively (**Fig. R32c**). Moreover, the electrochemical double-layer capacitance (C_{dl}) examinations revealed that *A*-$Fe_2S_1N_5$/SNC exhibited the highest C_{dl} (13.6 mF cm^{-2}), confirming the highest exposed electrochemical active surface area for ORR (**Fig. R32d**).

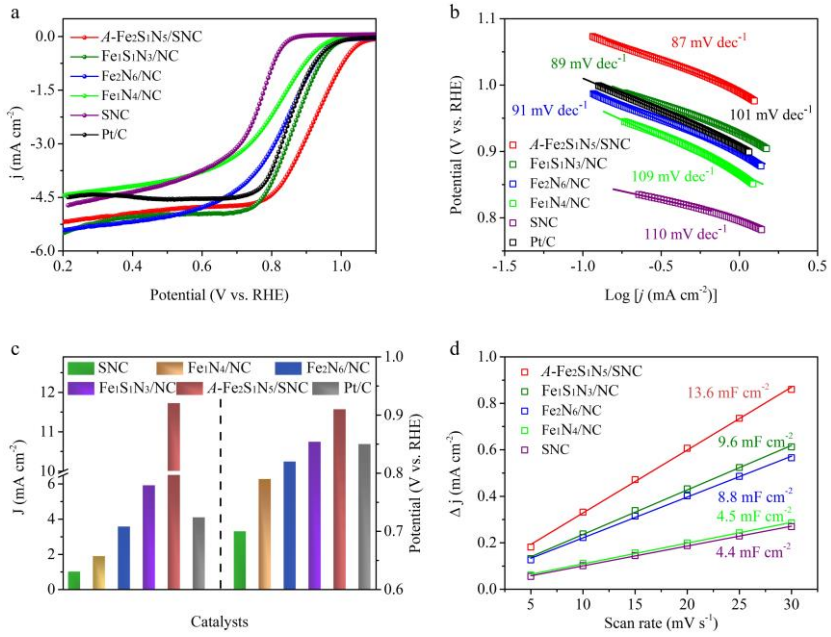

Fig. R32. ORR electrochemical activity in 0.1 M KOH. (a) LSV curves, (b) Tafel slopes, (c) kinetic current density (J_k) at 0.85 V versus reversible hydrogen electrode (versus RHE) and half-wave potentials, and (d) calculated C_{dl} values of *A*-$Fe_2S_1N_5$/SNC, $Fe_1S_1N_3$/NC, Fe_2N_6/NC, Fe_1N_4/NC, and SNC catalysts.

(4) According to the reviewer's comment, we have investigated the OER mechanism on the Fe_1-N_3S-C sites in detail. Initially, the Pourbaix diagram of the $Fe_1S_1N_3$/NC catalyst was calculated in **Fig. R34,** and the corresponding configurations were shown in **Fig. R33**. The optimized configurations of OER intermediates and the free energy change of primary steps for OER on the 2OH-$Fe_1S_1N_3$/NC system are shown in **Fig. R35** and **Fig. R36**, respectively.

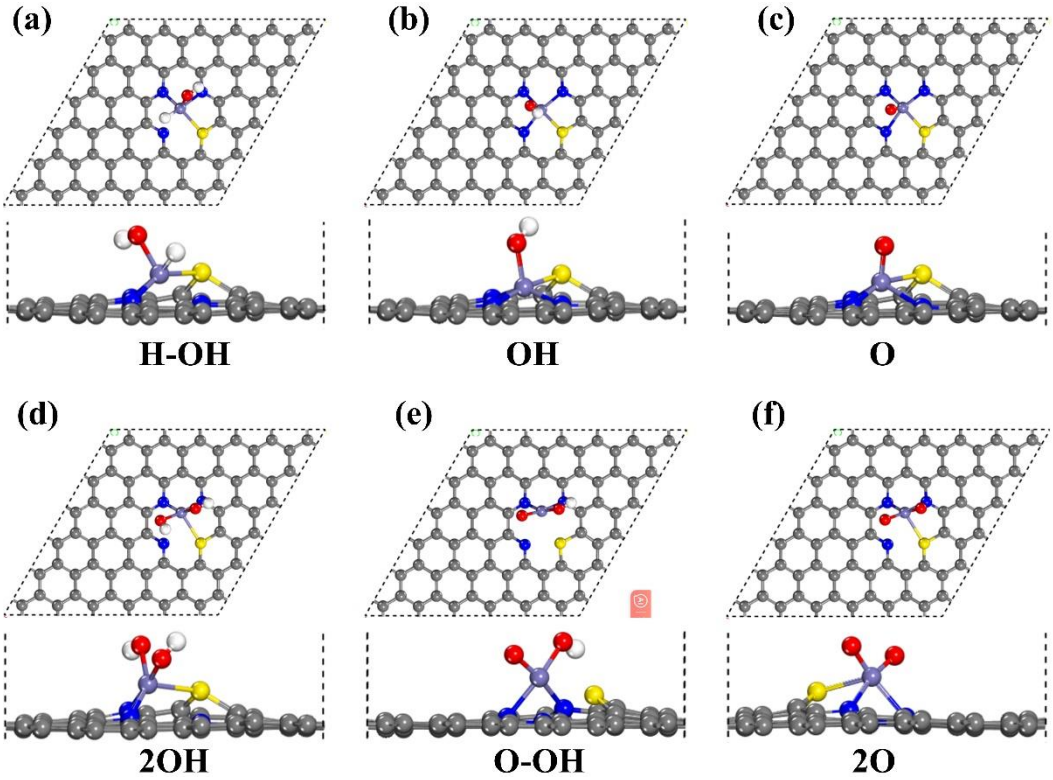

Fig. R33. Optimized configurations of H, O, and OH coverage on the $Fe_1S_1N_3$/NC system. The brown, yellow, red, gray, blue, and white ball marks Fe, S, O, C, N, and H atoms, respectively.

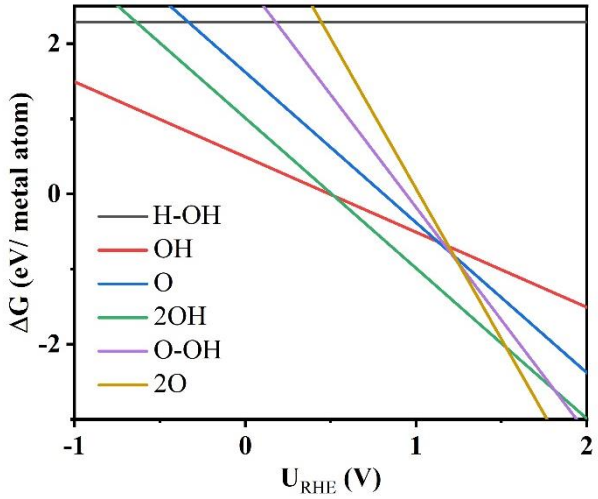

Fig. R34. The free energy change of different intermediate coverage versus reversed hydrogen electrode potential.

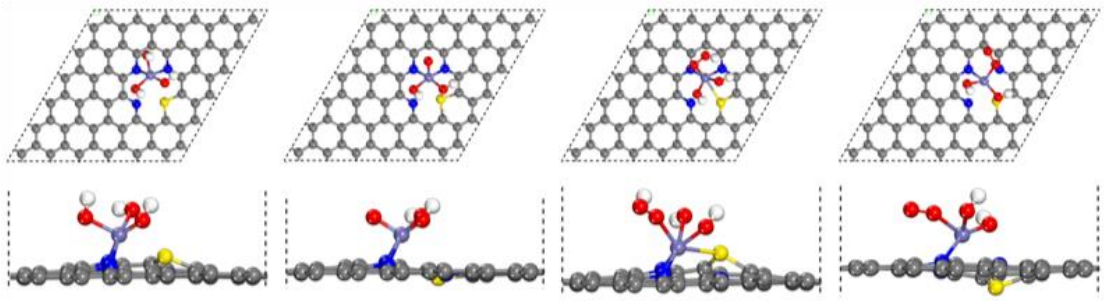

Fig. R35. Optimized configurations of OER intermediates on the 2OH-$Fe_1S_1N_3$/NC system. The brown, yellow, red, gray, blue, and white ball marks Fe, S, O, C, N, and H atoms, respectively.

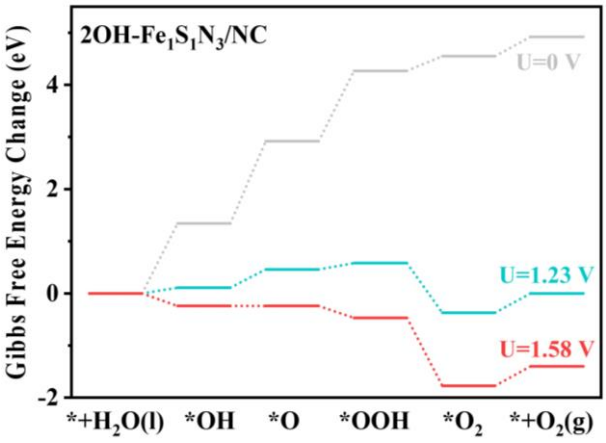

Fig. R36. The free energy change of primary steps for OER on the 2OH-$Fe_1S_1N_3$/NC

sites under the RHE with 0, 1.23, and 1.58 V. wherein the 1.23 V and 1.58 V indicates the equilibrium potential and the onset potential of OER, respectively.

Our revision: We have revised our manuscript according to the reviewer's suggestion (**Line 142, 155, 173, 174, 179, 181, 188-190, 213-216, 374-380,** and **Fig. 4a** in the revised manuscript, **Supplementary Fig. 8, Fig. 12, Figs. 14-15, Fig. 17, Fig. 21, Fig. 26, Figs. 33-37, Fig. 66, Figs. 69-70, Figs. 73-74, and Fig. 77**).

12. What is the role of trimesic acid in the synthesis? It seems a source of carbon. The equation for the calculation of TOF should be added in SI.

Response: Thank you for your careful comment. In the development of the *A*-$Fe_2S_1N_5$/SNC catalyst, the initial step involved the preparation of a carbon support that was co-doped with sulfur and nitrogen. Subsequently, a specific quantity of iron precursor, dicyandiamide, and trimesic acid were meticulously combined and subjected to evaporation until dry. Dicyandiamide serves as an additional carbon source. During the pyrolysis process in an inert atmosphere, dicyandiamide undergoes dissociation, resulting in the formation of ammonia and carbon species at a temperature of 550 ^{o}C.[1] Trimesic acid is recognized as one of the most effective and extensively utilized ligands, attributed to its stability, structural rigidity, and suitable connectivity.[2] In this context, trimesic acid was employed as an organic linker.[3] When subjected to 900-1000 ^{o}C, a minimal quantity of trimesic acid can mitigate the extensive decomposition of dicyandiamide, thereby enhancing the yield of the resultant product.[4-6] Furthermore, during the synthesis process, dicyandiamide can interact with the carboxylic acid

groups present in trimesic acid, leading to the formation of a two-dimensional sheet structure.[7] Subsequently, we performed a supplementary experiment in which only dicyandiamide was introduced in the second step, followed by high-temperature pyrolysis. As depicted in **Fig. R37,** the absence of trimesic acid resulted in a nearly 60% reduction in product quality.

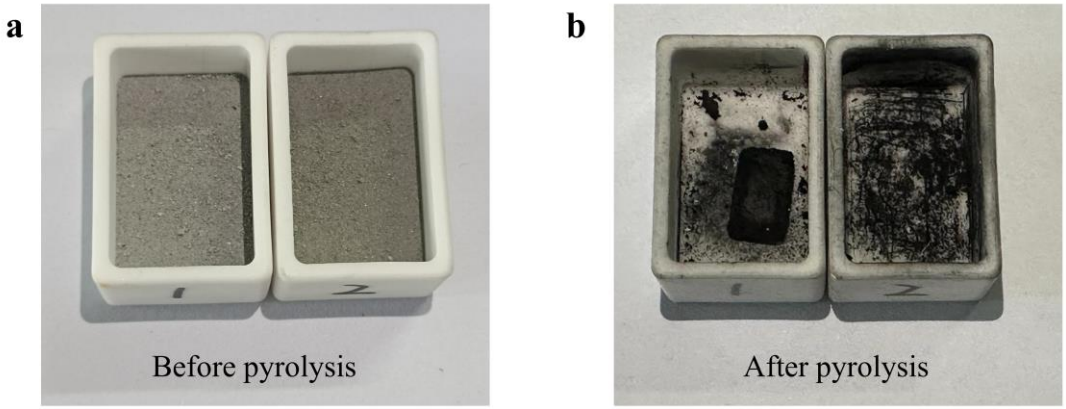

Fig. R37. Photographs (a) before pyrolysis and (b) after pyrolysis. The left image includes the incorporation of trimeric acid, whereas the right image does not contain any trimeric acid.

Furthermore, in alignment with your recommendation, the relevant calculation formulas for Turnover Frequency (TOF) and Mass Activity (MA) are presented as follows:

Supplementary Note 1: Calculation for Turnover Frequency (TOF)

Initially, it was assumed that each iron atom within the catalyst contributed to the formation of a single active center. The quantity of iron (Fe) atoms present in the *A*-$Fe_2S_1N_5$/SNC catalyst was determined based on the molar mass of Fe and the mass loading on the carbon cloth electrode, which was obtained from the results of ICP analysis. The Fe content of the catalyst, as indicated by ICP-OES measurements, was

approximately 6.72 wt%, with a mass loading of around 0.67 mg cm^{-2}. Consequently, the Turnover Frequency (TOF) of the *A*-$Fe_2S_1N_5$/SNC electrocatalyst was calculated using equation (1).

$$\mathrm{TOF} = \frac{\text{number of } O_2 \text{ turnovers}}{\text{number of metal ions}} \quad (1)$$

The number of total O_2 turnovers was calculated using the current density (j) from the OER-LSV polarization:

Number of O_2 turnovers:

$$= \left(\mathrm{j}\frac{\mathrm{mA}}{\mathrm{cm}^2}\right)\left(\frac{1\ \frac{\mathrm{C}}{\mathrm{s}}}{1000\ \mathrm{mA}}\right)\left(\frac{1\ \mathrm{mol\ e^-}}{96485\ \mathrm{C}}\right)\left(\frac{1\ \mathrm{mol\ O_2}}{4\ \mathrm{mol\ e^-}}\right)\left(\frac{6.02\times10^{23}\ \mathrm{mol\ O_2}}{1\ \mathrm{mol\ O_2}}\right)$$

$$= 1.56\ \times\ 10^{15}\ \frac{{O_2}/{s}}{\mathrm{cm}^2}\ \mathrm{per}\ \frac{\mathrm{mA}}{\mathrm{cm}^2} \quad (2)$$

The upper limit of active sites density for *A*-$Fe_2S_1N_5$/SNC:

$$= \frac{0.67\ mg\ cm^{-2}\times10^{-3}\times6.72\%\times6.023\times10^{23}}{55.85\ g\ mol^{-1}}\ per\ cm^2$$

$$= 0.48\times10^{18}\ Fe\ site\ per\ cm^2 \quad (3)$$

The TOF of *A*-$Fe_2S_1N_5$/SNC can be obtained via the current density from the OER LSV polarization curves and according to:

$$\mathrm{TOF} = \frac{1.56\times10^{15}}{0.48\times10^{18}}\ |j| = 0.0033|j| \quad (4)$$

Particularly, at the overpotential of 250 and 300 mV, the current density of OER is 50 and 242 mA cm^{-2}, respectively. Therefore, the TOF values of the *A*-$Fe_2S_1N_5$/SNC electrocatalyst were calculated to be:

$$\mathrm{TOF}_{(250\ mV)} = 0.0033\times50 = 0.165\ O_2\ s^{-1} = 594\ O_2\ h^{-1}. \quad (5)$$

$$TOF_{(300\ mV)} = 0.0033\times242 = 0.799\ O_2\ s^{-1} = 2875\ O_2\ h^{-1}. \quad (6)$$

Supplementary Note 2: Mass activity (MA) calculation

Mass activity (A g_{metal}^{-1}) was derived from the current density (mA cm^{-2}) normalized by the mass loading (0.67 mg cm^{-2}) and per metal at a certainly applied overpotential. The following equation exhibited the mass activity of *A*-$Fe_2S_1N_5$/SNC:

$$\text{Mass activity} = \frac{|j|}{0.67\times6.72\%} = 22.2|j|\text{A } g_{metal}^{-1} \text{ per cm}^2 \quad (7)$$

The current densities for *A*-$Fe_2S_1N_5$/SNC are 50 and 242 mA cm^{-2} at the overpotential of 250 and 300 mV, respectively. Therefore, the mass activities were calculated to be:

$$\text{Mass activity}_{250\ mV} = 22.2\times50 = 1110\ A\ g_{metal}^{-1} = 1.11\ A\ mg_{metal}^{-1} \quad (8)$$

$$\text{Mass activity}_{300\ mV} = 22.2\times242 = 5372\ A\ g_{metal}^{-1} = 5.37\ A\ mg_{metal}^{-1} \quad (9)$$

References:

[1] Zhang, L. et al. Engineering synergistic edge-N dipole in metal-free carbon nanoflakes toward the intensified oxygen reduction electrocatalysis, *Adv. Funct. Mater*. **31**, 2103187 (2021).

[2] Kumaraguru, S. et al. Influence of cobalt, nickel and copper-based metal-organic frameworks on the corrosion protection of mild steel. *Transactions of the IMF* **95**, 131-136 (2017).

[3] Thangavel, P. et al. Graphene-nanoplatelets-supported NiFe-MOF: high-efficiency and ultra-stable oxygen electrodes for sustained alkaline anion exchange membrane water electrolysis. *Energy Environ. Sci.* **13**, 3447-3458 (2020).

[4] Jiang, Z. et al. Atomic interface effect of a single atom copper catalyst for enhanced oxygen reduction reactions, *Energy Environ. Sci*. **12**, 3508-3514 (2019).

[5] Jiang, Z. et al. Discovery of main group single Sb-N_4 active sites for CO_2 electroreduction to formate with high efficiency, *Energy Environ. Sci*. **13**, 2856-2863 (2020).

[6] Sultan, S. et al. Single atoms and clusters based nanomaterials for hydrogen evolution, oxygen evolution reactions, and full water splitting. *Adv. Energy Mater*. **9**, 1900624 (2019).

[7] Li, F. et al. Boosting oxygen reduction catalysis with abundant copper single atom active sites. *Energy Environ. Sci*. **11**, 2263-2269 (2018).

Our revision: We have revised our manuscript according to the reviewer's suggestion (**Supplementary Note 1** and **Note 2**).

13. Bader charge analysis of Fe atom bonded to N and S clearly shows a difference. I understand it is challenging but can the authors provide a charge on each Fe site from XANES or EXAFS?

Response: Thank you for your challenging suggestions. The local electronic structure and the coordination environment of the catalysts are correlated with their catalytic performance, which can be detected by synchrotron-radiated X-ray absorption fine structure (XAFS). Synchrotron-radiated XAFS measurement can be divided into both extended X-ray absorption fine structure (EXAFS) and X-ray absorption near edge structure (XANES).[1-4] The processes of scattering or absorption can be observed during the irradiation process, which provides insights into the atomic structure, elemental composition, and local chemical environment. For the EXAFS region, the core

electrons of the probed atom become photoelectrons due to the excitation of X-ray. Subsequently, a single scattering of the resulting photoelectron between the probed atom and the coordination atom leads to the EXAFS signal.[5,6] Therefore, the EXAFS is usually used to detect the local structure environment of the probed atom including the coordination type, coordination number, coordination distance, and disorder of the surrounding coordination atoms.

In contrast to EXAFS, the XANES signal is generated by the multiple scattering of photoelectrons emitted from the atom under investigation. This phenomenon provides insights into the average oxidation state and coordination chemistry of the examined atom.[7,8] For XANES, it can be divided into the regions of pre-edge, edge, and post-edge. The pre-edge reflects the information of system symmetry and orbital hybridization, which originate from the inner electron transition to the empty bound states. The absorption edge of XANES reflects the average oxidation state of the probed atom, which defines the ionization threshold.[9] The absorption edge of the probed atom shifts to higher energy with the increase of the average oxidation state. The post-edge reflects the spatial structure of the neighbor atom, which originates from the multiple-scattering resonances of the photoelectrons. Therefore, the XANES are usually used to analysis the average oxidation state and the characteristic peak of the probed atom. The Fe dual-atom sites in *A*-$Fe_2S_1N_5$/SNC exhibit distinct charges as a result of their asymmetric coordination configuration. XANES analysis provides insights solely into the average oxidation state, thereby limiting the ability to ascertain the specific charge on each Fe site within *A*-$Fe_2S_1N_5$/SNC through either XANES or EXAFS analysis.

References:

[1] Chen, W. et al. Single tungsten atoms supported on MOF-serived N-doped carbon for robust electrochemical hydrogen evolution. *Adv. Mater*. **30**, 1800396 (2018).

[2] Li, X. et al. In situ/operando techniques for characterization of single-atom catalysts. *ACS Catal*. **9**, 2521-2531 (2019).

[3] Gates, B. C. et al. Supported metal clusters: synthesis, structure, and catalysis. *Chem. Rev*. **95**, 511-522 (1995).

[4] de Groot, F. et al. High resolution X-ray emission and X-ray absorption spectroscopy. *Chem. Rev*. **101**, 1779-1808 (2001).

[5] Rehr, J. et al. Theoretical approaches to x-ray absorption fine structure. *Rev. Mod. Phys*. **72**, 621-654 (2000).

[6] Funke, H. et al. Wavelet analysis of extended x-ray absorption fine structure data. *Phys. Rev. B* **71**, 094110 (2005).

[7] Zhuang, Z. et al. Single-atom catalysis enables long-life, high-energy lithium-sulfur batteries. *Nano Res*. **13**, 1856-1866 (2020).

[8] Xiao, M. L. et al. Microporous framework induced synthesis of single-atom dispersed Fe-N-C acidic ORR catalyst and its in situ reduced Fe-N_4 active site identification revealed by X-ray absorption spectroscopy. *ACS Catal*. **8**, 2824-2832 (2018).

[9] Pertot, Y. et al. Time-resolved x-ray absorption spectroscopy with a water window high-harmonic source. *Science* **355**, 264 (2017).

14. What about the stability of the catalyst in ORR? After recycling the S2p peak was significantly diminished. Please explain.

Response: Thank you for your meaningful comments. The durability of a catalyst is a crucial parameter for evaluating its performance, alongside its activity. In response to your recommendation, we have evaluated the ORR stability of the *A*-$Fe_2S_1N_5$/SNC catalyst. As illustrated in **Fig. R38a**, the *A*-$Fe_2S_1N_5$/SNC catalyst exhibited negligible decay in the half-wave potential after undergoing 5000 continuous cycles. Additionally, the stability of the *A*-$Fe_2S_1N_5$/SNC catalyst was further examined using the chronopotentiometry technique, as shown in **Fig. R38b**. After a sustained testing duration of 40,000 s in 0.1 M KOH solution, the *A*-$Fe_2S_1N_5$/SNC catalyst maintained approximately 90.4% of its initial current. These findings provide compelling evidence that the *A*-$Fe_2S_1N_5$/SNC catalyst demonstrates commendable stability in alkaline solutions during the ORR process.

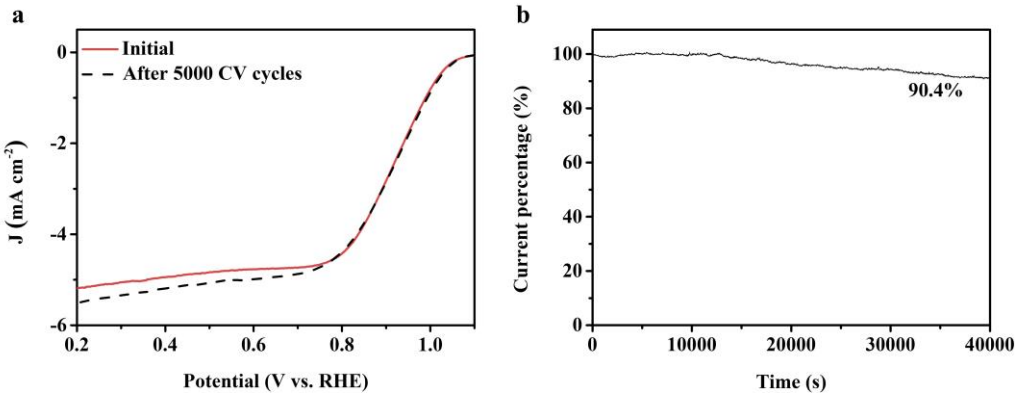

Fig. R38. (a) Before and after the CV test. (b) Durability test of *A*-$Fe_2S_1N_5$/SNC.

To assess the durability of the alkaline OER for the *A*-$Fe_2S_1N_5$/SNC catalyst, we performed TEM, XRD, Raman spectroscopy, and XPS analyses after the durability test. Notably, XPS was utilized to examine alterations in the surface elemental composition

of the *A*-$Fe_2S_1N_5$/SNC catalyst. As illustrated in **Fig. R39**, the XPS survey spectrum indicates that the elemental concentrations of S, C, N, and Fe exhibited negligible changes after the 5000 CV recycling test, thereby demonstrating the exceptional OER durability. It is important to note that the XPS measurements conducted on *A*-$Fe_2S_1N_5$/SNC before and after the recycling test were performed in batches, resulting in variations in intensity between the two sets of data. Consequently, when the S 2p data from before and after the recycling test are presented on the same scale, the intensity difference leads to a marked reduction in the S 2p signal after recycling. To more effectively convey the stability characteristics of the catalyst, the XPS spectra for S 2p before and after 50,000 CV cycles were displayed on separate scales (**Fig. R40**). Additionally, the element content in *A*-$Fe_2S_1N_5$/SNC was also labeled in the quantitative EDS spectrum before and after the stability test (**Fig. R41**). This provides additional evidence that sulfur remains unchanged in the catalyst after the stability test.

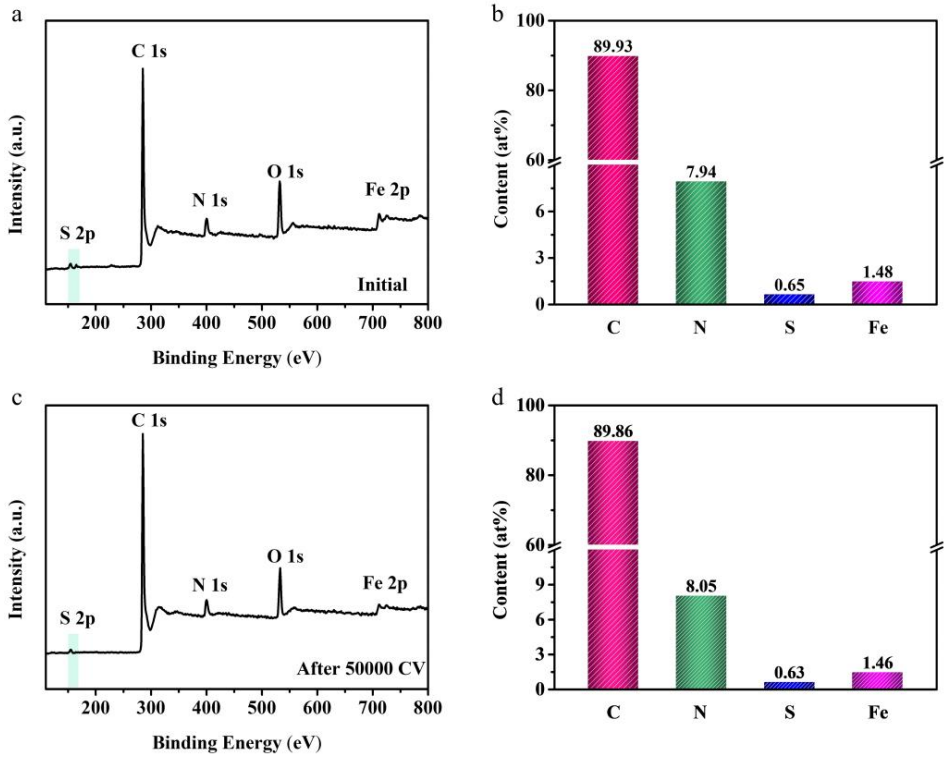

Fig. R39. XPS survey scan spectra of *A*-$Fe_2S_1N_5$/SNC (a) before and (c) after OER cycling. The atomic content percentages of C, N, S, and Fe in *A*-$Fe_2S_1N_5$/SNC were measured by XPS analysis (b) before and (d) after OER cycling.

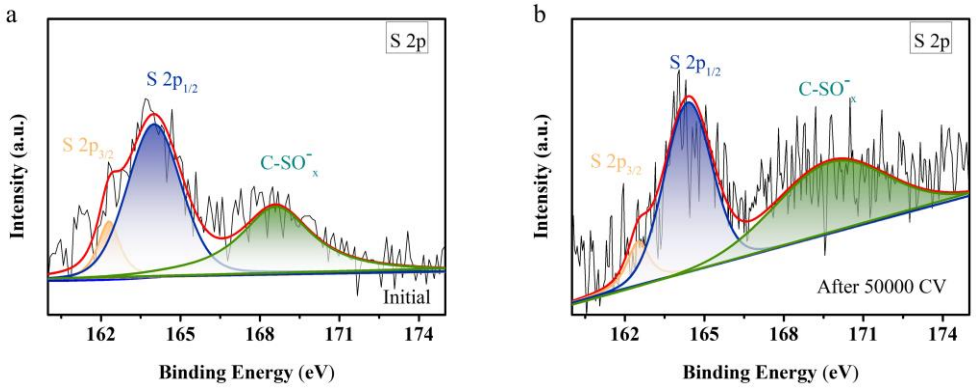

Fig. R40. XPS spectra for S 2p of (a) before 50000 CV and (b) after 50000 CV.

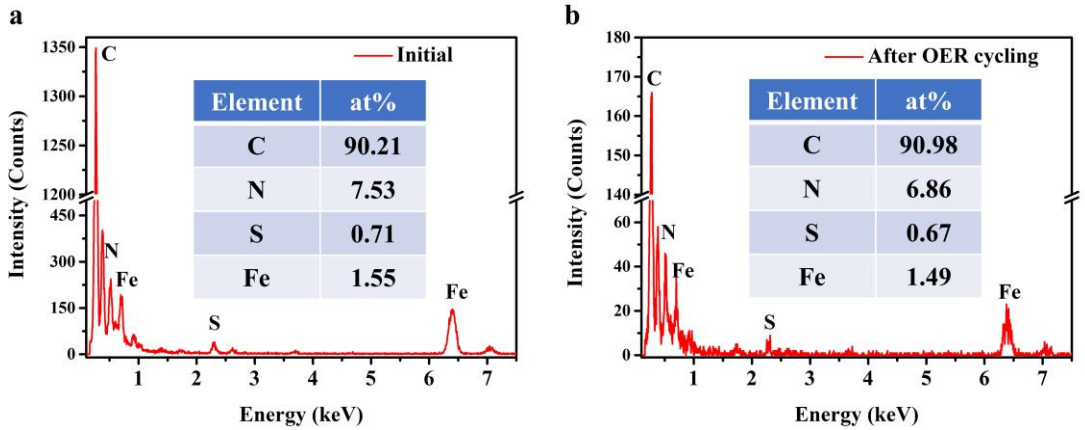

Fig. R41. The Elemental composition in the *A*-$Fe_2S_1N_5$/SNC catalyst (a) before and (b) after the OER cycling.

To further demonstrate the stability of *A*-$Fe_2S_1N_5$/SNC, we conducted the ICP-OES analysis of the catalysts and the electrolyte after the durability test. As shown in **Table R10**, the metal contents of Fe in the *A*-$Fe_2S_1N_5$/SNC catalyst after the durability test are comparable to their fresh values, which indicate only a minor amount of metal dissolved into the electrolyte. Furthermore, the ICP-OES analysis was performed to

confirm the accurate metal content of Fe in the electrolyte after the OER durability test (**Table R11**). The undetectable metal content in the electrolyte suggests that the Fe remains in the *A*-$Fe_2S_1N_5$/SNC catalyst even after the OER durability test.

Table R10. Results of metal leaching experiments (before and after 50000 CV cycles) by ICP.

Sample	Fe content (wt%)		Retention
A-$Fe_2S_1N_5$/SNC	Initial	6.72	97.9%
	50000 CV	6.57	

Table R11. The metal content of Fe in the electrolyte was measured by ICP-OES after the OER durability test.

Sample	Post electrolyte
Fe wt %	0.00

Our revision: We have revised our manuscript according to the reviewer's suggestion (**Line 288-290** in the revised manuscript, **Supplementary Fig. 24**, **Fig. 48, and Table 6**).

15. Please add how XANES data was fitted. In Figure S26.there are two pyridinic N. Please Correct it.

Response: We thank the reviewer for this comment. The Fe K-edge theoretical XANES simulations were carried out with the FDMNES code in the framework of a real-space full multiple scattering (FMS) scheme using Muffin-tin approximation for the potential.

The energy-dependent exchange-correlation potential was calculated in the real Hedin-Lundqvist scheme, and then the spectra convoluted using a Lorentzian function with an energy-dependent width to account for the broadening due both to the core-hole width and to the final state width.[1,2] Furthermore, we modified the N K-edge XANES spectra of the *A*-$Fe_2S_1N_5$/SNC, Fe_2N_6/NC, and Fe_1N_4/NC according to your suggestion, as depicted in **Fig. R42.**

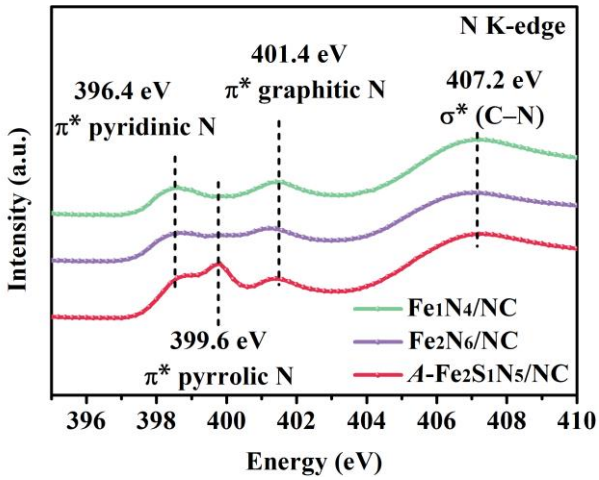

Fig. R42. N K-edge XANES spectra of the *A*-$Fe_2S_1N_5$/SNC, Fe_2N_6/NC, and Fe_1N_4/NC.

References:

[1] Rehr, J. J. et al. Theoretical approaches to x-ray absorption fine structure. *Reviews of Modern Physics* **72**, 621-654 (2000).

[2] Bunău, O. et al. Self-consistent aspects of x-ray absorption calculations. *Journal of Physics: Condensed Matter* **21**, 345501 (2009).

Our revision: We have revised our manuscript according to the reviewer's suggestion (**Supplementary Fig. 29c**).

16. The evolved oxygen should be measured either from GC or water replacement

approach and demonstrate actual Faradain efficiency.

Response: Thank you very much for the constructive suggestion. To determine the Faradaic efficiency (FE) of the OER, a water replacement approach was employed to monitor the generated O_2. The O_2 amount collected experimentally matches well with the theoretical value, illustrating an excellent Faradaic efficiency (99.1%) of *A*-$Fe_2S_1N_5$/SNC for OER (**Fig. R43**), and the corresponding test details are presented in the revised **Supporting Information**.

Supplementary Note 3: Faradaic efficiency (FE) determination

To assess the Faradaic efficiency of oxygen evolution, we need to evaluate the ratio of the amounts of O_2 produced experimentally to those of O_2 produced theoretically at cathodic electrolysis. Therefore, the FE was calculated by the following equations:

$$\mathrm{FE} = \frac{n \times F \times V}{Q \times V_m} \times 100\%$$

Where n is 4 for O_2 production. F is the Faraday constant (96485 A·s mol^{-1}), and V is the oxygen volume measured by the drainage method at a current density of 10 mA cm^{-2} under the standard conditions (room temperature). V_m is the molar volume (22.4 L/mol) and Q is the total theoretical electric charge. Test condition: The Faradaic efficiency was estimated using a simple water drainage method. The evolved O_2 was collected in a 10 mL graduated tube filled with electrolyte. The current was fixed at 10 mA cm^{-2} for about 60 minutes under standard conditions (25 °C, 1 atm). The gas volume of O_2 collected was recorded every 10 minutes. The accumulated charge passing through the working electrode was calculated by the equation (Q = It).

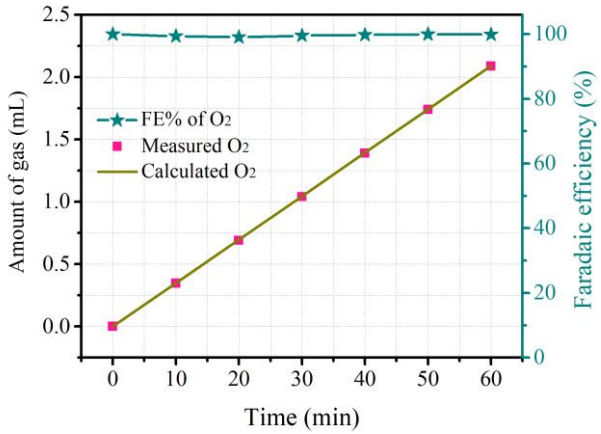

Fig. R43. Experimental and theoretical volumes of generated O_2 and Faraday efficiency of *A*-$Fe_2S_1N_5$/SNC in 1.0 M KOH.

Our revision: We have revised our manuscript according to the reviewer's suggestion (**Line 249-252** in the revised manuscript, **Supplementary Fig. 39** and **Supplementary Note 3**).

17. How authors have chosen a certain metal content for the synthesis. Is it possible to add more metal during synthesis? After the synthesis, did the authors use any acid leaching to remove any nanoparticles?

Response: Thank you for your insightful comments. The effect of metal precursor (anhydrous ferric chloride) content on OER activity has also been studied. To obtain the optimal amount of metal, we used different qualities of metal precursors (30, 40, 50, 60, 70, and 100 mg) to prepare the catalyst using the same process. Subsequently, the OER performance of the resulting catalysts was evaluated. We depicted the relation of metal precursor content as the function of the overpotentials for the electrode. The OER activity of the catalyst was the best when the amount of metal precursor was 40 mg, as shown in the LSV curve of OER in **Fig. R44a**. As expected, a volcano-type relation

was observed between metal precursor content and the overpotentials (**Fig. R44b**). The optimal metal precursor content was determined as 40 mg, where an excessive amount of metal content may result in the low activity and metal aggregation of the catalyst.

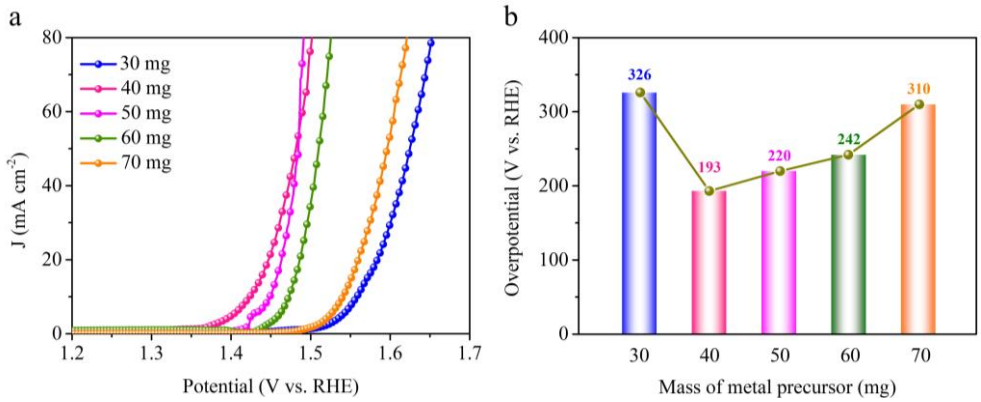

Fig. R44. (a) OER polarization curves of different usage of metal precursor content for different samples. (b) Activity volcano plot based on varied metal precursor content.

Additionally, TEM patterns reveal that the obvious metal particles appear when the concentration of Fe^{3+} is increased to 60 mg (**Fig. R45**). Further increasing the metal content to 100 mg results in a substantial presence of metal particles on the nanosheets (**Fig. R46**). At a precursor concentration of 40 mg, the synthesized *A*-$Fe_2S_1N_5$/SNC exhibits a high metal loading of 6.72 wt% and is characterized as a diatomic catalyst. Notably, the absence of clusters or particles in the catalyst eliminates the necessity for an acid leaching process, which could potentially diminish the metal loading of the catalyst.

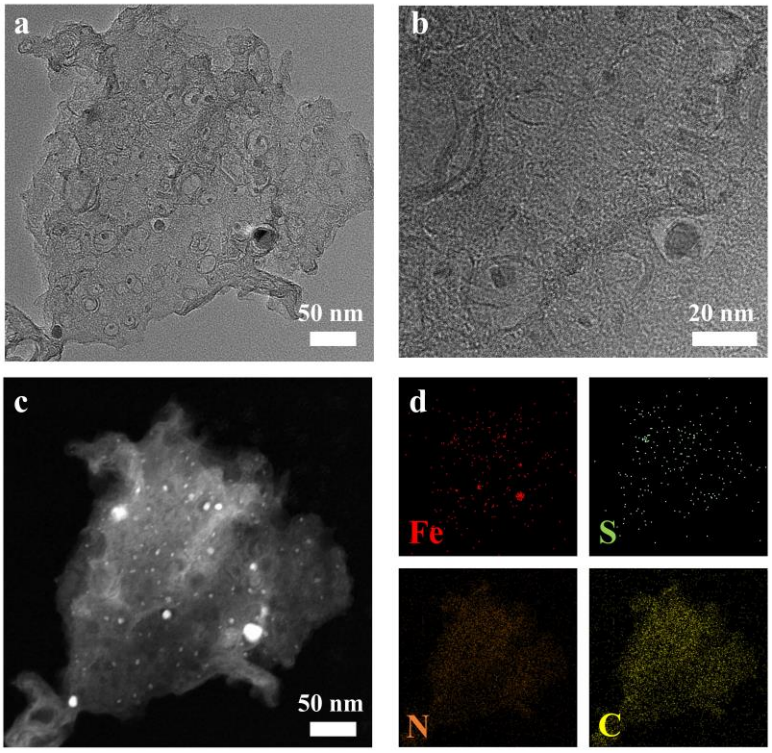

Fig. R45. TEM characterization of the catalyst with mental usage of 60 mg. (a) Low magnification TEM image. (b) High magnification TEM image. (c) HRTEM. (d) EDS mapping of Fe, S, N, and C elements.

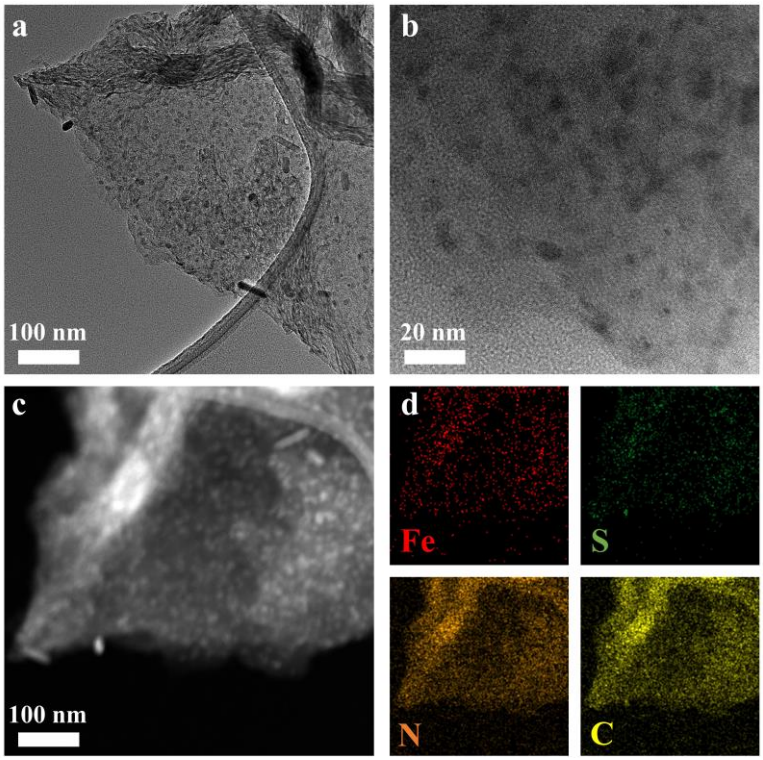

Fig. R46. TEM characterization of the catalyst with mental usage of 100 mg. (a) Low magnification TEM image. (b) High magnification TEM image. (c) HRTEM. (d) EDS mapping of Fe, S, N, and C elements.

Our revision: We have revised our manuscript according to the reviewer's suggestion (**Line 216-218** in the revised manuscript and **Supplementary Fig. 32**).

18. There are many grammatical/sentence errors. Remove hyperbolic phrases such as ultrahigh, unprecedented, etc. Double atom catalysts should be written as dual atom catalysts. Rephrase "which suffered confined pyrolysis…" Please add enough details in the experimental part such as the operating voltage of TEM. How samples were prepared for XPS. Do the authors perform any carbon correction of XPS spectra? What was the voltage for AC-HAADF?

Response: Thank you for your meaningful comments. We have made corrections to the inappropriate expressions in the manuscript. The experimental details and conditions of XPS, TEM, and AC-HAADF have been supplemented in the revised **Supporting Information**.

The added experimental details are as follows: Transmission electron microscopy (TEM) and high-resolution transmission electron microscopy (HRTEM) were performed using a FEI Talos F200S microscope operating at an accelerating voltage of 200 kV. Initially, the fully ground sample was dispersed in an ethanol solution and subjected to ultrasonic homogenization. Subsequently, droplets of the solution were deposited onto a copper mesh coated with a carbon film using a pipette. After drying at

room temperature, TEM samples were prepared for analysis. The TEM investigations were carried out at an operating voltage of 200 kV. Additionally, the Transmission Electron Microscope with Probe Corrector (Themis Z, Thermo Fisher Scientific) was performed at an accelerating voltage of 200 kV.

X-ray photoelectron spectroscopy (XPS) measurements were conducted utilizing an Omicron EA 125 Energy Analyzer equipped with a monochromated Al K-alpha source operating at 1486.7 eV. High-resolution core-level component X-ray photoelectron spectroscopy (XPS) scans were conducted utilizing a pass energy of 20 eV in high magnification mode. The entrance and exit slits were set to 6 mm and 3 mm, respectively, resulting in an overall source and instrumental resolution of 0.6 eV. The methodology for preparing XPS samples involves the following steps: First, a small quantity of the powder sample is positioned on a piece of aluminum foil. Subsequently, a section of double-sided Scotch tape, approximately 5 × 5 mm^2 in area, is cut and held with tweezers to adhere the sample. The tape along with the sample, is then subjected to gentle pressure using a tablet press until the sample surface is rendered flat and free of contaminants. Finally, the prepared sample is placed on the sample stage for analysis. All spectra were calibrated by using the C 1s (binding energy of 284.8 eV) as a reference point.

Our revision: We have revised our manuscript according to the reviewer's suggestion (**Characterizations** section in **Supplementary Information**).

Response to Reviewer 5：

Atomic catalysts with diversified well-defined coordination configurations have attracted increasing attention due to their maximized atomic utilization and high catalytic activity. This manuscript submitted by Chen et al. constructed asymmetric nitrogen, sulfur-coordinated diatomic iron centers on highly defective nitrogen-doped carbon nanosheets, which possessed the atomic configuration of N_2S_1Fe-FeN3 moiety. Benefited from the spontaneous electric polarization occurred on the iron dual-atom sites of the *A*-$Fe_2S_1N_5$/SNC catalyst, it displays ultra-high OER activity and stability in alkaline electrolyte. Moreover, alkaline AEMWE device catalyzed by *A*-$Fe_2S_1N_5$/SNC displays good performance, indicating its broad practical application potential. This work provides a new guidance for simultaneously balancing activity and stability of double-atom catalysts toward electrocatalysis applications. Therefore, I recommend publishing this manuscript after minor revisions. Below is a list of specific comments and questions the authors should address before publication.

Response: We truly thank the reviewer for his/her careful reading and constructive comments. All the insightful comments have been thoroughly considered, and we have performed a series of additional experiments to address all the concerns raised by the reviewer. The corresponding revisions have been made (please see the below).

1. When fitting the average oxidation state of Fe in A-$Fe_2S_1N_5$/SNC from the XANES spectra, the author mentioned that the first maximum of the first derivative is used as refer in Fig S14. So, why not choose the peak near 7120 eV for fitting?

Response: Thank you for your insightful comments. To evaluate the valence states of Fe in *A*-$Fe_2S_1N_5$/SNC, the first-derivative XANES curves of two reference samples (Fe_2O_3 and Fe foil) were derived, and the linear relationship between the photoenergy at the maximum intensity and the valence state was well established.[1] The chemical state of the *A*-$Fe_2S_1N_5$/SNC was studied by XPS. The co-existence of Fe^{2+} (709.1 and 722.4 eV) and Fe^{3+} (711.5 and 724.5 eV) is evident in the high-resolution Fe 2p spectra (**Fig. R47a**). **Fig. R47b** involves the Fe K-edge XANES spectra of *A*-$Fe_2S_1N_5$/SNC. The adsorption threshold position of *A*-$Fe_2S_1N_5$/SNC was both located between FeS_2 and Fe_2O_3, which indicates the average metal valence states of Fe species in *A*-$Fe_2S_1N_5$/SNC was situated between +2 ~ +3. Therefore, combining the results of XPS and XANES, when fitting the average oxidation state of Fe in *A*-$Fe_2S_1N_5$/SNC, choosing the peak at 7125.18 eV was more reasonable. Some previous literature also reported similar results. For example, Zeng et al. reported a precise modulation of Fe-N-C catalysts at the atomic level by a "single-atom to single-atom" grafting of a Pt atom onto the Fe atom at the Fe-N_4 center through a bridging oxygen molecule (Pt_1@Fe-N-C). The first derivative of XANES of Fe K-edge shows a negative shift of Fe K-edge in Pt_1@Fe-N-C compared with the Fe-N-C catalyst, indicating the decreased iron oxidation state after grafting Pt_1 (**Fig. R48a**).[2] Qiao et al. synthesized an atomically dispersed Fe-N-C electrocatalyst, the typical way-through the pyrolysis of microporous carbon fibers coated with a zeolitic imidazolate framework (ZIF). In the comparison of the first derivative of XANES for the different samples, there is a negative shift from 7117.7 eV to 7117.0 eV, which corresponds to Fe-N_4 bonds after sulfuration (**Fig.**

R48b).[3] Hao et al. reported a carbon-rich DAC with Ni dual-atom sites (Ni_2NC) towards CO_2RR to CO and investigated the catalytic behavior of dual-atom sites. The first derivative of XANES in **Fig. R48c** suggested a slight decrease in the oxidation state of Ni during the CO_2RR process due to charge transfer from the active sites to reactants and intermediates. The first-order derivative in an ex-situ state can take the second peak.[4] Chen et al. synthesized atomically dispersed catalysts with novel sulfur-bridged Cu-S-Ni sites (named Cu-S-Ni/SNC), utilizing biomass wool keratin as a precursor. The first derivative XANES curve (**Fig. R48d**) shows that the valence states of Cu and Ni are between the valence states of metal foil and oxide standard samples. The first-order derivative of Ni K-edge of Cu-S-Ni/SNC can also take the second peak.[5] Therefore, for the *A*-$Fe_2S_1N_5$/SNC, choosing the peak near 7125.18 eV for fitting is reasonable.

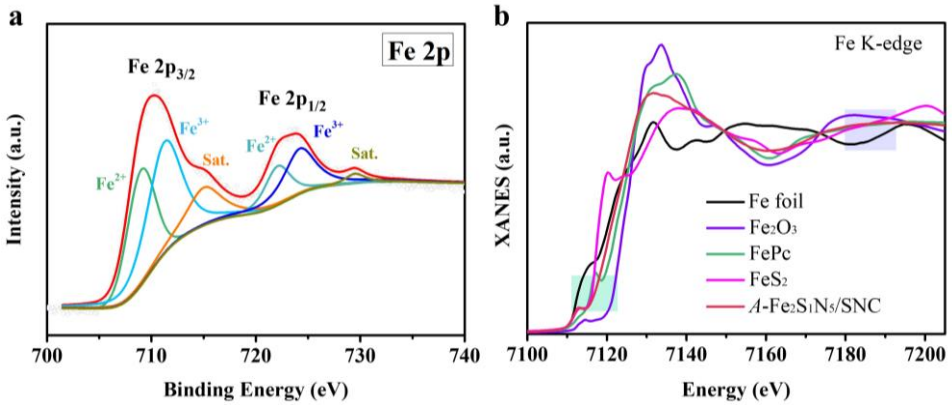

Fig. R47. (a) The Fe 2p XPS spectrum of *A*-$Fe_2S_1N_5$/SNC. (b) Fe K-edge XANES spectra.

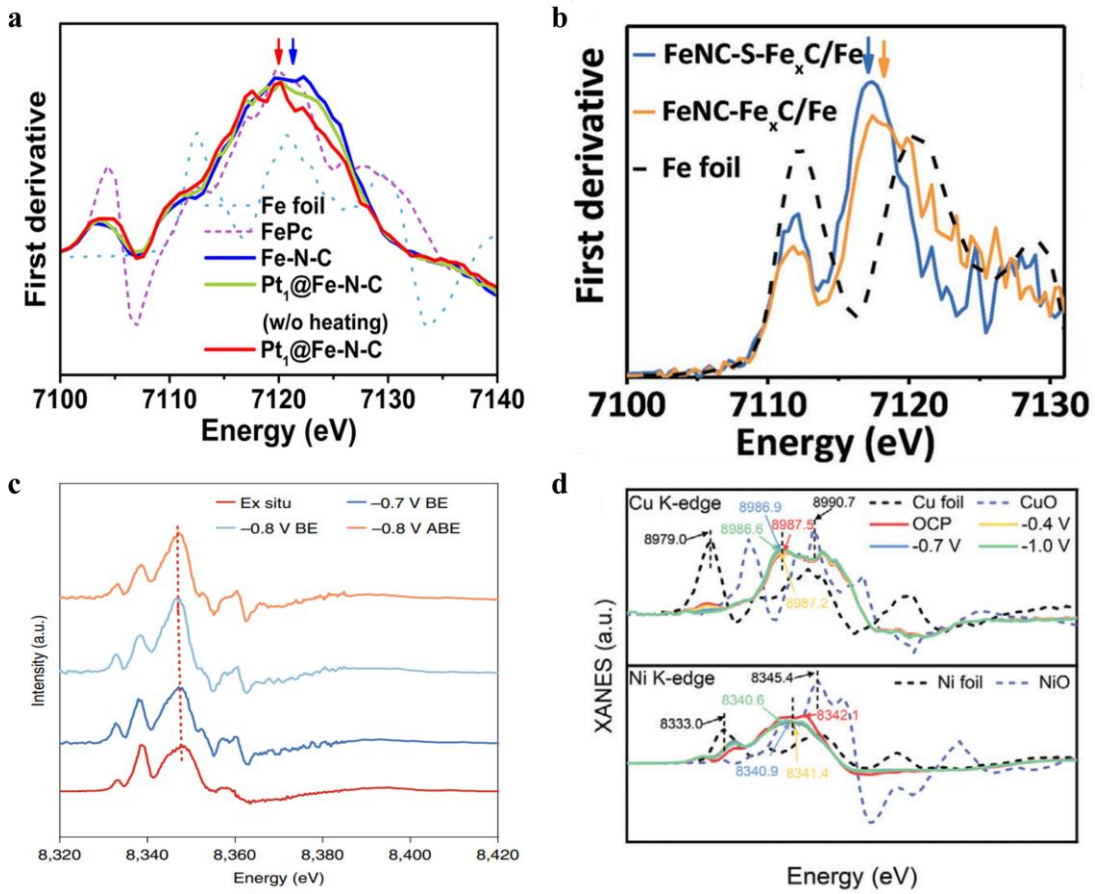

Fig. R48. (a) First derivative of XANES at the Fe *K*-edge for different catalysts.[2] (b) The first-derivative for the FeNC-S-Fe$_x$C/Fe catalyst, the control sample FeNC-Fe$_x$C/Fe, and other standard samples.[3] (c) The first derivative of XANES, the vertical dotted line indicates the tendency of the valence state shift at Ni K edge of Ni$_2$NC at different applied potentials.[4] (d) Corresponding first-derivative XANES curves of Cu-S-Ni/SNC.[5]

References:

[1] Wang, X. et al. Atomically dispersed pentacoordinated-zirconium catalyst with axial oxygen ligand for oxygen reduction reaction. *Angew. Chem. Int. Ed*. **61**, e202209746 (2018).

[2] Zeng, X. et al. Single-atom to single-atom grafting of Pt$_1$ onto Fe-N$_4$ center:

Pt_1@Fe-N-C multifunctional electrocatalyst with significantly enhanced properties, *Adv. Energy Mater*. **8**, 1701345 (2018).

[3] Sulfuration of an Fe-N-C catalyst containing Fe_xC/Fe species to enhance the catalysis of oxygen reduction in acidic media and for use in flexible Zn-air batteries, *Adv. Mater*. **30**, 1804504 (2018).

[4] Hao, Q. et al. Nickel dual-atom sites for electrochemical carbon dioxide reduction. *Nature Synthesis* **1**, 719-728 (2022).

[5] Sun, Z. et al. Sulfur-bridged asymmetric CuNi bimetallic atom sites for CO_2 reduction with high efficiency. *Adv. Mater.* 2404665 (2024).

2. Please check whether the lsv after ECSA normalization is suitable carefully and give the corresponding calculation details. It should be noted that ECSA = C_{dl}/C_s.

Response: Thank you for your helpful comments. To further determine whether the enhanced OER activity is solely contingent on the increased active sites, the ECSA-normalized OER polarization curves are calculated. The *A*-$Fe_2S_1N_5$/SNC still possesses lower overpotential, illustrative of the asymmetric dual Fe atoms not only creating new active sites but also enhancing its intrinsic activity.[1,2] The ECSA was determined by: ECSA = C_{dl}/C_s, where C_{dl} is double-layer capacitance and C_s is the specific capacitance of the sample. In this study, a general specific capacitance of $C_s = 0.035$ mF cm^{-2} was used based on the typical reported value.[3] C_{dl} was determined by the equation $C_{dl} = i_c/\nu$, where i_c is the charging current and ν is the scan rate. A series of CV tests in the non-faradaic potential region under different scan rates (20, 40, 60, 80, 100, and 120 mV s^{-1})

were performed. By plotting measured i_c versus v, C_{dl} was obtained from the slopes of the linear fitting (**Table R12**). The determined C_{dl} and ECSAs of various catalysts. Considering ECSA-normalized OER activity, specific activity still followed the order *A*-$Fe_2S_1N_5$/SNC > $Fe_1S_1N_3$/NC > Fe_2N_6/NC > Fe_1N_4/NC (**Fig. R49**), suggesting intrinsically improved OER activity on the *A*-$Fe_2S_1N_5$/SNC catalyst due to the asymmetric diatomic configuration.

Table R12. The determined C_{dl} and ECSAs of various catalysts.

Catalyst	C_{dl} (mF)	ECSA (cm^2)[a]
A-$Fe_2S_1N_5$/SNC	3.2	91.4
$Fe_1S_1N_3$/NC	2.5	71.4
Fe_2N_6/NC	2.1	60.0
Fe_1N_4/NC	1.2	28.6

[a] ECSAs are determined by the equation of ECSA = $C_{dl}/C_s \times S$ and *S* is the electrode area (1.0 cm^2).

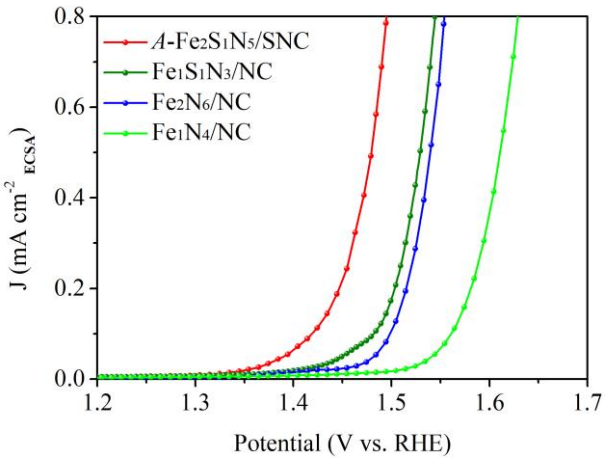

Fig. R49. ECSA-normalized LSVs of *A*-$Fe_2S_1N_5$/SNC, $Fe_1S_1N_3$/NC, Fe_2N_6/NC, and Fe_1N_4/NC.

References:

[1] Sun, K. et al. Interfacial water engineering boosts neutral water reduction. *Nat. Commun,* 6260, (2022).

[2] Wu, Z.-Y. et al. Non-iridium-based electrocatalyst for durable acidic oxygen evolution reaction in proton exchange membrane water electrolysis. *Nat. Mater*. **22**, 100-108 (2023).

[3] Qin, Y. et al. RuO_2 electronic structure and lattice strain dual engineering for enhanced acidic oxygen evolution reaction performance, *Nat. Commun*. **13**, 3784 (2022).

Our revision: We have revised our manuscript according to the reviewer's suggestion (**Line 225-234** in the revised manuscript, **Supplementary Fig. 37a and Supplementary Table 4**).

3. According to the catalyst's XPS data of S after the stability test, the signal of S almost disappeared. Is it accompanied by the metal leaching? Please provide the Fe content change before and after the test via ICP. In addition, how do the authors consider the balance between S corrosion during the OER process and its regulation of the original catalyst structure? Will this regulatory effect persist?

Response: Thank you for your meaningful comments. To assess the durability of the alkaline OER for the *A*-$Fe_2S_1N_5$/SNC catalyst, we performed TEM, XRD, Raman spectroscopy, and XPS analyses after the durability test. Notably, XPS was utilized to examine alterations in the surface elemental composition of the *A*-$Fe_2S_1N_5$/SNC

catalyst. As illustrated in **Fig. R50**, the XPS survey spectrum indicates that the elemental concentrations of S, C, N, and Fe exhibited negligible changes after the 5000 CV recycling test, thereby demonstrating exceptional OER durability.

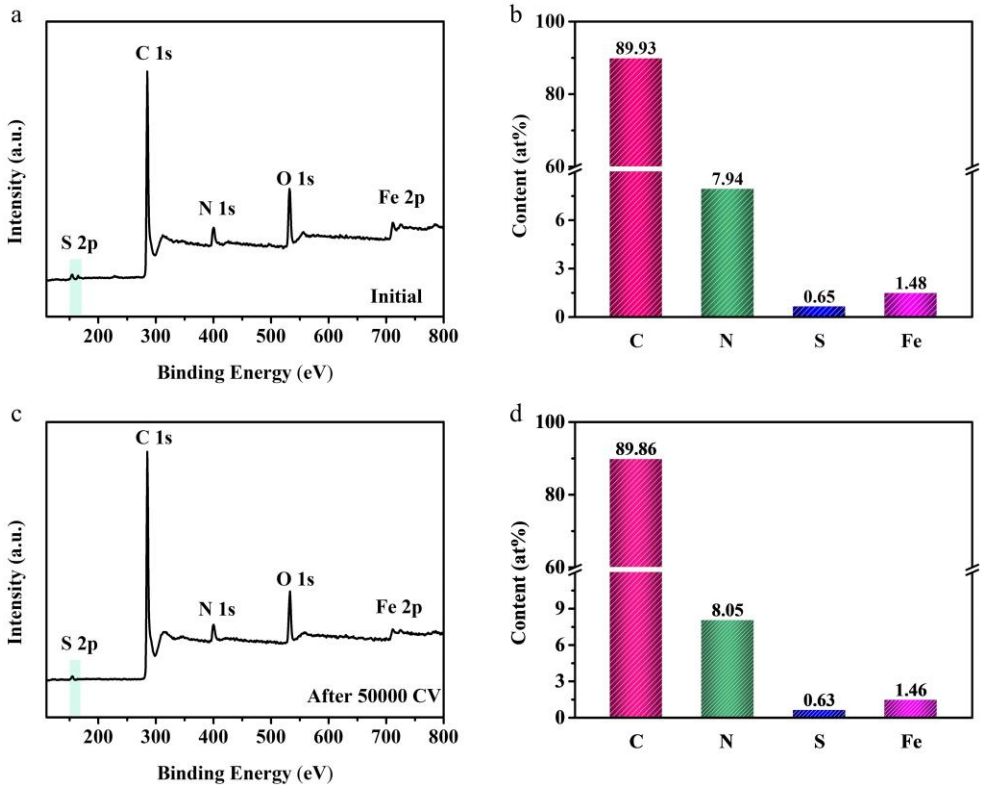

Fig. R50. XPS survey scan spectra of *A*-$Fe_2S_1N_5$/SNC (a) before and (c) after OER cycling. The atomic content percentages of C, N, S, and Fe in *A*-$Fe_2S_1N_5$/SNC were measured by XPS analysis (b) before and (d) after OER cycling.

It is important to note that the XPS measurements conducted on *A*-$Fe_2S_1N_5$/SNC before and after the recycling test were performed in batches, resulting in variations in intensity between the two sets of data. Consequently, when the S 2p data from before and after the recycling test are presented on the same scale, the intensity difference leads to a marked reduction in the S 2p signal after recycling. To more effectively convey the stability characteristics of the catalyst, the XPS spectra for S 2p before and

after 50,000 CV cycles were displayed on separate scales (**Fig. R51**). Additionally, the element content in *A*-$Fe_2S_1N_5$/SNC was also labeled in the quantitative EDS spectrum before and after the stability test (**Fig. R52**). This provides additional evidence that sulfur remains unchanged in the catalyst after the stability test. Consequently, there was no occurrence of S corrosion during the OER process.

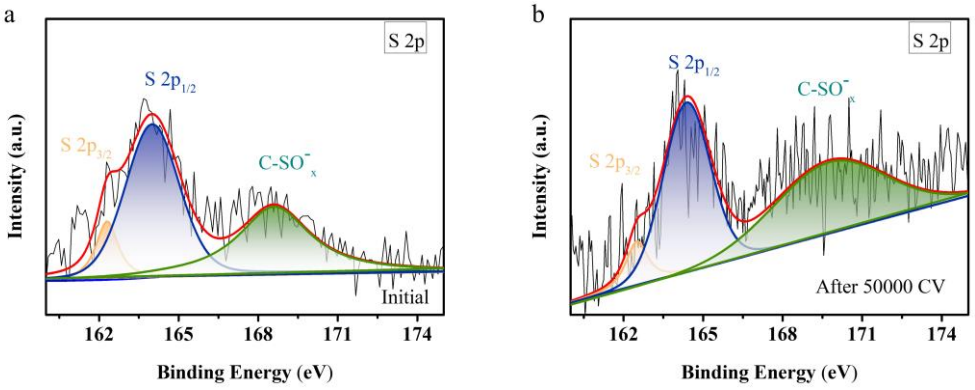

Fig. R51. XPS spectra for S 2p of (a) before 50000 CV and (b) after 50000 CV.

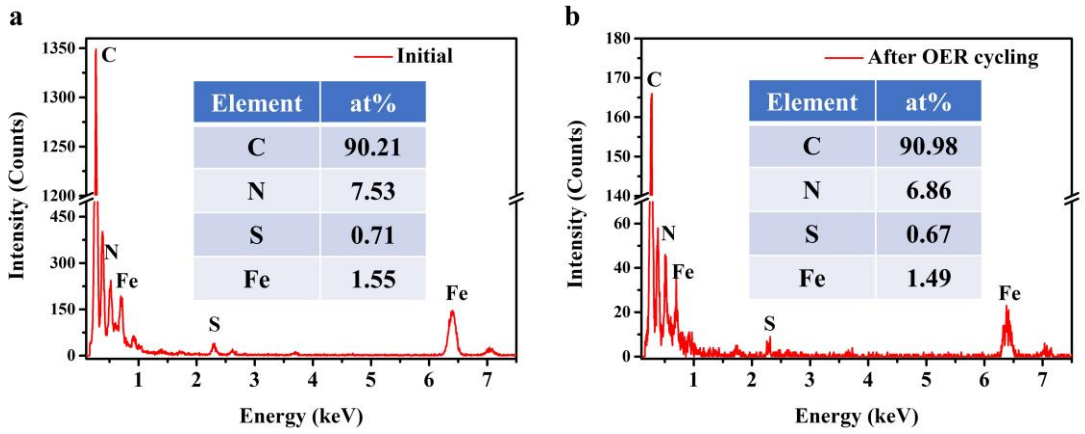

Fig. R52. The Elemental composition in the *A*-$Fe_2S_1N_5$/SNC catalyst (a) before and (b) after the OER cycling.

To further demonstrate the stability of *A*-$Fe_2S_1N_5$/SNC, we conducted the ICP-OES analysis of the catalysts and the electrolyte after the durability test. As shown in **Table R13**, the metal contents of Fe in the *A*-$Fe_2S_1N_5$/SNC catalyst after the durability

test are comparable to their fresh values, which indicate only a minor amount of metal dissolved into the electrolyte. Furthermore, the ICP-OES analysis was performed to confirm the accurate metal content of Fe in the electrolyte after the OER durability test (**Table R14**). The undetectable metal content in the electrolyte suggests that the Fe remains in the *A*-$Fe_2S_1N_5$/SNC catalyst even after the OER durability test.

Table R13. Results of metal leaching experiments (before and after 50000 CV cycles) by ICP.

Sample	Fe content (wt%)		Retention
A-$Fe_2S_1N_5$/SNC	Initial	6.72	97.9%
	50000 CV	6.57	

Table R14. The metal content of Fe in the electrolyte was measured by ICP-OES after the OER durability test.

Sample	Post electrolyte
Fe wt %	0.00

In addition, in the previously reported S-coordinated single-atom catalysts, M-S bonds exhibited good activity and stability in the OER. For instance, Su et al. constructed a dual-metal S-Fe-Co-N_5 catalyst by embedding Fe and S into the structure of Co-N_4 motifs. After stability testing, there are no crystalline metal sulfides in the spent S-Fe-Co-N_5 catalyst, which suggests the good stability of the unique S-Fe-Co-N_5 site.[1] Yasin et al. established the unsymmetrically N and S coordinated Fe/Co dual atom catalysts (Fe,Co/DSA-NSC). The HAADF-STEM and XPS measurements of Fe,Co/DSA-NSC were conducted after the OER durability test. The HAADF-STEM

image endorsed that no typical obvious change is observed in the physical structure after the stability test. Furthermore, the XPS investigation conveyed conclusive evidence that the Fe,Co/DSA-NSC catalyst was chemically stable after the durability test.[2] Chen et al. developed an unusual ZnCoFe hetero-trimetallic atom site anchored in sulfur/nitrogen-doped carbon with the configuration of $ZnN_3CoN_3FeN_2S$. The XPS results show that all the elements remain in ZnCoFe-TAC/SNC after the stability test.[3] It can be concluded that Fe atoms coordinated with S demonstrate good robustness and can maintain structural stability during the OER process. The regulatory effect of sulfur has been observed to persist throughout the OER process.

References:

[1] Su, H. et al. Flexibility tuning of dual-metal S-Fe-Co-N_5 catalysts with O-axial ligand structure for electrocatalytic water splitting, *Adv. Energy Mater*. **13**, 2301547 (2023).

[2] Ghulam Yasin et al. Simultaneously engineering the synergistic-effects and coordination-environment of dual-single-atomic iron/cobalt-sites as a bifunctional oxygen electrocatalyst for rechargeable zinc-air batteries, *ACS Catal*. **13**, 2313-2325 (2023).

[3] Chen, C. et al. An asymmetrically coordinated ZnCoFe hetero-trimetallic atom catalyst enhances the electrocatalytic oxygen reaction, *Energy Environ. Sci.* **17**, 2298–2308 (2024).

Our revision: We have revised our manuscript according to the reviewer's suggestion (**Line 288-290**, **Supplementary Fig. 24** and **Fig. 47**, **Supplementary Table 6**).

4. It is recommended that authors supply the catalytic performance under the industrial electrolytic water system, such as 80 °C, 30% KOH.

Response: Thank you for your helpful comments. Based on the suggestions of the reviewers, we investigated the prospective utilization of the *A*-$Fe_2S_1N_5$/SNC catalyst under industrial conditions (60-80 °C, 20-30% KOH, 400 mA cm^{-2}). Subsequently, the OER activity of the *A*-$Fe_2S_1N_5$/SNC catalyst was assessed through linear sweep voltammetry at a scan rate of 5 mV s^{-1} in a 30% KOH solution at a temperature of 80 °C. As illustrated in **Fig. R53a**, the *A*-$Fe_2S_1N_5$/SNC catalyst shines with impressive OER performance even in industrial settings. Meanwhile, **Fig. R53b** highlights the overpotential comparisons across various current densities. Notably, it boasts a remarkably low overpotential of just 340 mV at 400 mA cm^{-2}.

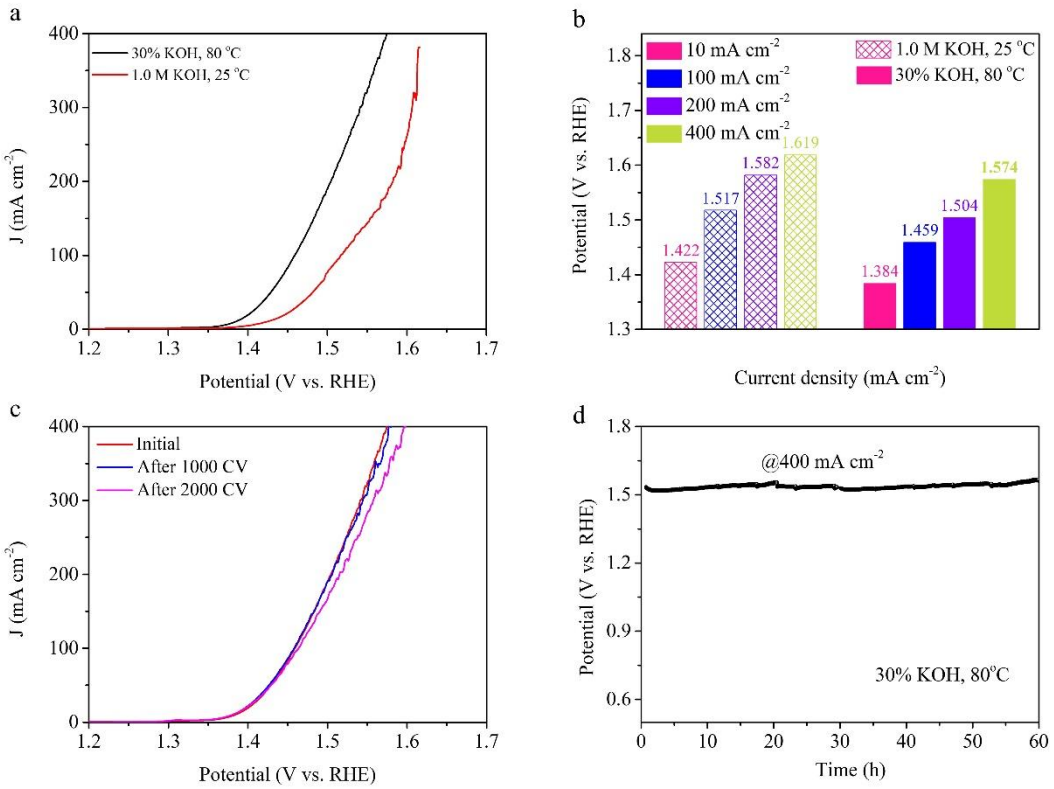

Fig. R53. The catalytic performance of *A*-$Fe_2S_1N_5$/SNC under the industrial electrolytic water system. (a) LSV curves of the *A*-$Fe_2S_1N_5$/SNC electrode for water electrolysis in 30% KOH at 80 ºC and 1.0 M KOH at 25 ºC. (b) Potentials for OER on the *A*-

$Fe_2S_1N_5$/SNC electrode at current densities of 10, 100, 200, and 400 mA cm^{-2} in 30% KOH at 80 ºC and 1.0 M KOH at 25 ºC, respectively. The results were carried out with 90% iR-compensation. (c) LSV curves for initial, 1000, and 2000 CV tests on the *A*-$Fe_2S_1N_5$/SNC catalyst in 30% KOH electrolyte at 80 ºC. (d) Chronpotentiometric curve at 400 mA cm^{-2} for the *A*-$Fe_2S_1N_5$/SNC electrode towards OER in 30% KOH at 80 ºC.

In the context of practical electrocatalysts, it is essential to ensure robust stability during prolonged operation. To evaluate the stability of *A*-$Fe_2S_1N_5$/SNC under industrial conditions, we conducted the durability test. The resulting electrolyzer consistently delivered a current density of 400 mA cm^{-2} at approximately 1.57 V for 60 h, demonstrating the high stability of the *A*-$Fe_2S_1N_5$/SNC catalyst under substantial current conditions (**Fig. R53d**). Additionally, we performed water oxidation experiments utilizing cyclic voltammetry at a scan rate of 50 mV s^{-1}, which revealed a little appreciable decrease in current densities over 2,000 cycles (**Fig. R53c**).

Our revision: We have revised our manuscript according to the reviewer's suggestion (**Line 252-254** in the revised manuscript, **Supplementary Fig. 40**).

5. There are some vague description and typo errors in this article. Thus, for a better readability, please check throughout the whole article text and correct all the errors.

Response: I express my gratitude for your insightful recommendations. Following your advice, we have revised the ambiguous descriptions and corrected typographical errors throughout the manuscript, thereby enhancing its overall readability.

REVIEWER COMMENTS

Reviewer #1 (Remarks to the Author):

The authors have well addressed my concerns.

Reviewer #2 (Remarks to the Author):

The authors have done a considerable work to improve their manuscript and tried to address the numerous comments raised by the referees. The paper can now be accepted for publication.

Reviewer #3 (Remarks to the Author):

I carefully reviewed the revised version of the manuscript and the author's response to my comments. The authors have addressed most concerns by adding new data/explanations and implementing suggested changes. The manuscript has been significantly improved and can be considered for publication after addressing these issues.

1. As per CHNS analysis, the S content is ~1.7 wt% which is equivalent to ~10.51 at% while Fe content was 6.72 wt% (22.84 at%). Therefore, each S-coordinated cavity in graphenic network occupies two Fe atoms. These results indirectly evidence the presence of Fe in dual sites. The authors should add these in the main text.
2. Additionally, ssNMR is not very noisy and peaks are broad, therefore, the authors should not draw any conclusion related to the presence of SOx based on NMR. The authors should use other ancillary techniques such as NH3-TPD to titrate acidic SO4 sites.
3. The author's explanation that S atoms were oxidized via an X-ray beam in an XPS chamber is not correct. Under an ultrahigh vacuum, there is a minimum chance of in-situ oxidation. Therefore any such assumption should be removed, if already added to the manuscript.

Reviewer #4 (Remarks to the Author):

We have carefully read the authors' responses and agree with the revisions they have made in response to previous comments. Therefore, I recommend publishing this manuscript.

Reviewer #5 (Remarks to the Author):

I co-reviewed this manuscript with one of the reviewers who provided the listed reports. This is part of the Nature Communications initiative to facilitate training in peer review and to provide appropriate recognition for Early Career Researchers who co-review manuscripts.

Responses to the Referees' Comments

We thank the referees for their valuable comments on our manuscript. We have carefully considered the referees' comments and revised the manuscript accordingly. The reviewers' comments are laid out below in *Italic font* and specific concerns have been numbered. Our responses and corresponding revisions are given in normal font with red color.

Response to Reviewer 1：

The authors have well addressed my concerns.

Response: We thank the reviewer for the positive comments on the revised manuscript.

Response to Reviewer 2：

The authors have done a considerable work to improve their manuscript and tried to address the numerous comments raised by the referees. The paper can now be accepted for publication.

Response: We thank the reviewer for the positive comments.

Response to Reviewer 3：

I carefully reviewed the revised version of the manuscript and the author's response to my comments. The authors have addressed most concerns by adding new data/explanations and implementing suggested changes. The manuscript has been significantly improved and can be considered for publication after addressing these issues.

Response: We thank the reviewer for the time and efforts devoted to evaluating our manuscript. We revised carefully the manuscript according to the suggestions.

Comment 1: *As per CHNS analysis, the S content is ~1.7 wt% which is equivalent to ~10.51 at% while Fe content was 6.72 wt% (22.84 at%). Therefore, each S-coordinated cavity in graphenic network occupies two Fe atoms. These results indirectly evidence the presence of Fe in dual sites. The authors should add these in the main text.*

Response: We sincerely appreciate the reviewer for the insightful comment and constructive suggestion. According to the reviewer's suggestion, we have added the corresponding description to the main text.

Our revision: We have revised our manuscript according to the reviewer's suggestion (**Line 160-161** in the revised manuscript).

Comment 2: *Additionally, ssNMR is not very noisy and peaks are broad, therefore, the authors should not draw any conclusion related to the presence of SO_x based on NMR. The authors should use other ancillary techniques such as NH_3-TPD to titrate acidic SO_4 sites.*

Response: We thank the reviewer for this comment. According to the reviewer's

suggestion, the NH_3-TPD technique was performed to titrate acidic SO_4 sites. As shown in **Fig. R1,** the *A*-$Fe_2S_1N_5$/SNC catalyst displayed negligible acidic sites across the *A*-$Fe_2S_1N_5$/SNC catalyst.

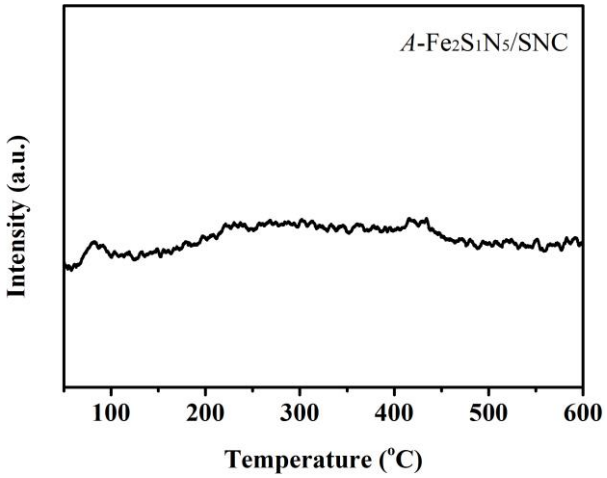

Fig. R1. NH_3-TPD profile of *A*-$Fe_2S_1N_5$/SNC catalyst.

Our revision: We have revised our manuscript according to the reviewer's suggestion (**Line 210-212** in the revised manuscript and **Supplementary Fig. 31**).

Comment 3: *The author's explanation that S atoms were oxidized via an X-ray beam in an XPS chamber is not correct. Under an ultrahigh vacuum, there is a minimum chance of in-situ oxidation. Therefore, any such assumption should be removed, if already added to the manuscript.*

Response: Thank you very much for the constructive suggestion. According to the reviewer's suggestion, the relevant description has been deleted in the manuscript.

Response to Reviewer 4：

We have carefully read the authors' responses and agree with the revisions they have made in response to previous comments. Therefore, I recommend publishing this manuscript.

Response: Thank you for your valuable comments and feedbacks in the previous round.

Response to Reviewer 5：

I co-reviewed this manuscript with one of the reviewers who provided the listed reports. This is part of the Nature Communications initiative to facilitate training in peer review and to provide appropriate recognition for Early Career Researchers who co-review manuscripts.

Response: Thank you for your kind recommendation and careful review.